

Development and Application of Disposable Microfluidic Devices for Bioassays

Yiwen Ouyang
Wuhan, Hubei, China

Bachelor of Science, Wuhan University, 2009

A Dissertation presented to the Graduate Faculty
of the University of Virginia in Candidacy for the Degree of
Doctor of Philosophy

Department of Chemistry

University of Virginia
May, 2014

Abstract

The research presented in this dissertation is focused on the development of polyester-toner (PeT) based microchip as a potential affordable, disposable microfluidic platform for medical diagnostics. Besides a brief review of current fabrication techniques for microfluidic devices, the fundamental concepts of flow control methods on microfluidic platform and the latest detection methods are introduced in Chapter 1. Chapter 2 describes a rapid, cost-effective fabrication method to realize the valving functionality on PeT microfluidic device, where laser printer lithography was employed to conveniently create hydrophobic toner valves providing tunable burst pressures in microchannel. Chapter 3 continues to focus on the development of the flow control on PeT microchip. A CD-sized five-layer PeT microfluidic device operated on an inexpensive and portable battery-powered centrifugal system was developed, providing all the basic fluidic control functionalities which are essential for conducting comprehensive biology assays. By simply controlling the rotation speed of the PeT microchip, sample and buffer can be aliquoted from 200 nL to 2 μ L and serially-diluted by buffer in parallel. Additionally, in order to enhance the mixing process on the chip, a reciprocating mixing domain for improving the mixing of viscous biology sample was designed and characterized in Chapter 3. With the advantage of the flow control functionalities developed for PeT microchip, Chapter 4 describes an adaption of DNA-induced magnetic bead aggregation detection reaction to a CD-sized PeT microchip as a simple and high-throughput solution to enumerate the white cells in human blood. Furthermore, development of PeT microchip for PCR application using an in-house infra-red thermal control system was detailed in

Chapter 5. PeT microchips with different samples throughput were designed and evaluated in terms of the temperature ramp rate, effectiveness of IR-PCR system for thermal cycle temperature control and PCR efficiency. The dynamic surface passivation for chip surface was devised so that PCR performance on PeT microchip is comparable to conventional glass microchips. Finally, feasible future research direction towards using PeT microchip as an integrated, commercialized platform for diagnostics is outlined in Chapter 6.

Table of Content

Chapter 1: Introduction	1
1.1 Overview	1
1.2 Fabrication Technology for Microfluidic Device.....	2
1.2.1 Fabrication of glass microfluidic devices.....	2
1.2.2 Fabrication of polymeric microfluidic devices	2
1.2.3 Fabrication of polyester-toner microfluidic devices	5
1.3 Flow Control in Microfluidic Devices	7
1.3.1 Control of fluid propulsion.....	7
1.3.2 Valving technology	11
1.3.3 Mixing technology	15
1.4 Visual Detection for Microfluidic System	18
1.5 Molecular Diagnostic Techniques	23
1.6 Concluding Remarks	26
1.7 Reference	27
Chapter 2: Rapid and Direct Patterning of ‘Tunable’ Hydrophobic Valves on Disposable Microchips by Laser Printer Lithography.....	33
2.1 Introduction	33
2.2 Theory.....	35

2.2.1 Burst pressures associated with printed features	35
2.2.2 Burst frequency on a centrifugal system associate with printed features ..	39
2.3 Material and Methods	40
2.3.1 Reagents	40
2.3.2 Fabrication of the hydrophobic patches	41
2.3.3 Contact angle measurement	41
2.3.4 Image analysis to quantitate the fractional area of toner printed at different gray-scale level	42
2.3.5 Fabrication of toner-based valves on PeT microdevices.....	42
2.3.6 Determine the contact angle on the sidewall.....	43
2.3.7 Characterization of burst pressure	44
2.3.8 Determining the burst frequency of the valve on a centrifugal system....	45
2.4 Results and Discussion	45
2.4.1 Selection of printer toners	45
2.4.2 Characterization of the toner-coated surface on Pe film	47
2.4.3 Characterization of the laser-ablated sidewall on PeT microdevice	49
2.4.4 Influence of the channel geometry on burst pressure	52
2.4.5 Influence of gray-scale level on burst pressure	53
2.4.6 Toner-valve performance in a centrifugal microfluidic device	54
2.4.7 Multivalve operation in a centrifugally-driven microfluidic system.....	55
2.5 Conclusions	58
2.6 Reference	59

Chapter 3: Multilevel Fluidic Flow Control for Rapid Protein Quantitation in a Rotationally-driven Polyester-Toner Microdevice	63
3.1 Introduction	63
3.2 The Working Principle	66
3.2.1 Volume Splitting	66
3.2.2 Multi-level aliquoting on 3D PeT microdevice for sample diluting	68
3.2.3 Surface-tension pump to assist reciprocating passive mixing	70
3.3 Material and Methods	73
3.3.1 Reagent.....	73
3.3.2 Fabrication of the PeT microchip.....	74
3.3.3 Spinner setup	75
3.3.4 Image analysis to quantitate the metered volume	76
3.4 Result and Discussion.....	76
3.4.1 Influence of multiple layer alignment on aliquoting performance	76
3.4.2 Influence of microfluidic network design on aliquoting process	77
3.4.3 Measurement of aliquotted volumes	80
3.4.4 Characterization of reciprocating mixing.....	83
3.4.5. Evaluating sample dilution performance.....	85
3.4.6 Colorimetric protein assay on the PeT microchip	87
3.5 Conclusion.....	91
3.6 Reference	93

Chapter 4: A Laminated Microdevice for Multiplexing Cell Counting by Magnetic Bead Aggregation on a Rotating Platform	95
4.1 Introduction	95
4.2 Material and Methods.....	98
4.2.1 Reagent.....	98
4.2.2 Device design	99
4.2.3 Device fabrication	101
4.2.4 Operational procedure of the PeT disc platform	102
4.2.5 Bi-directional rotating magnetic field	104
4.2.6 Image detection	105
4.2.7 Multiplexed pinwheel assays on PeT disc for cell counting	106
4.3 Result and Discussion.....	107
4.3.1 Validation of metering performance	107
4.3.2 Movement of beads under bi-directional magnetic field.....	110
4.3.3 Influence of rotation frequency of bi-RMF on beads assay	113
4.3.4 White blood cell counting for crude blood samples	115
4.4 Conclusion.....	118
4.5 Reference	119
Chapter 5: A Disposable Polyester-Toner Microchip for PCR via Infra-Red Mediated Thermal Control.....	122
5.1 Introduction	122

5.2 Material and Method	125
5.2.1 Reagents	125
5.2.2 Microdevice fabrication	125
5.2.3 IR- mediated temperature control system	126
5.2.4 Investigation on surface passivation	128
5.2.5 Amplification of λ -phage DNA in PeT microchip for single PCR	128
5.2.6 Amplification of Azospirillun brasilienses DNA in PeT microchip for single PCR	130
5.2.7 Characterizing the temperature behavior of multichamber PeT microchips on IR-control system.....	130
5.2.8 Multichambered PCR amplification on PeT microchip	131
5.3 Result and Discussion.....	132
5.3.1 Thermocycling on PeT microchip for single PCR amplification	132
5.3.2 Dynamic surface passivation to enhance the PCR efficiency	133
5.3.3 Amplification of λ -phage DNA and Azospirillun Brasilienses DNA...	135
5.3.4 Multi-chamber thermal control for PCR on a PeT microchip.....	138
5.3.5 Optimization of the ramp rate for multi-chambered PCR thermal cycling	141
5.3.6 Amplification of DNA fragment on multichamber PeT microchip	143
5.4 Conclusion.....	146
5.5 Reference	146
Chapter 6: Future Direction	150

6.1 Overview	150
6.2 Flow Control.....	150
6.3 Reagent Storage on PeT Microchip.....	151
6.4 Portable PeT Microdevices Platform for Integrated Assays	152
6.5 Reference	154

Acknowledgement

I would like to express my sincere gratitude to my PhD advisor, Dr. James P. Landers for the research opportunities in his laboratory over the past five years. He has enlightened and inspired me in the full aspect of my research life, including designing and conducting the experiments, grant proposing, scientific writing and conference presentation. In addition, with his support and encouragement for creativity and technical innovation, I was able to explore my research interest to the fullest extent. For these things, I feel blessed and will always be grateful. I also want to thank the following mentors in my graduate study. Dr. Matthew Begley has showed great wisdom and kindness to insightfully guide my study. Dr. Dede Haverstick has offered great perspectives and support to my research. I am thankful to the entire Landers group, for the company and the friendship. Particularly, I would like to thank Dr. Jingyi Li who I have directly worked and learned from, along with Dr. Jenny Lounsbury and Brian Poe for their guidance in the early stages of introducing me to the various instruments and techniques. At the same time, I would also like to thank my collaborators outside UVA who make direct contribution to my work, Christopher Phaneuf and Dr. Gabriela R. M. Duarte. Additionally, I greatly appreciate the dedication of my undergraduate research assistant, Paul S. Riehl. I would like to acknowledge my family in China for their constant support, particularly my mother, without whom I would not have accomplished what I have today. And finally, I would like to express my immeasurable appreciation to Shibo Wang for his love, support and encouragement. I dedicate this dissertation to them.

Chapter 1: Introduction

1.1 Overview

Lab-on-a-Chip (LOC) generally refers to a chip-format system that manipulates a small amount of fluid (nL to μ L), allowing to scale down and integrate single or multiple lab processes. Compared to most of bench-top methods in traditional labs, LOC technology allows for low-volume consumption of reagents, miniaturization, improved portability and potential for automation. As a result, LOC technology provides an attractive solution for point-of-care (POC) diagnostics, which could be used in the resource-limited circumstances for health monitoring or diseases diagnosis. As microfluidic devices focusing on specific applications become more prevalent, there is an increasing interest in designing a portable system that integrates flow control and detection at affordable fabrication cost with industrial manufacturability. This chapter is aimed to provide an introduction to the latest developments of microfluidic technologies in fabrication, flow control and detection. In addition, fundamental concepts and basic techniques that are relevant to the work in dissertation are also explained in detail.

1.2 Fabrication Technology for Microfluidic Device

1.2.1 Fabrication of glass microfluidic devices

In the early development of microfluidic systems, photolithography and wet etching were utilized for fabricating glass and silicon microdevices. Figure 1-1 shows typical fabrication steps for glass microdevices¹, which can control microfeatures down to the submicron scale. The process generally requires the use of clean room and hazardous chemicals. In addition, the fabrication time of a device is quite time consuming and labor intensive.

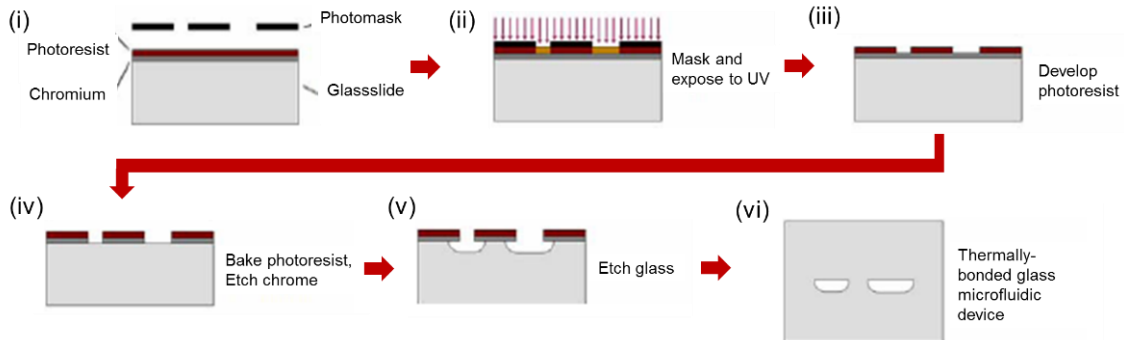


Figure 1-1: Standard photolithographic method for fabrication of glass microfluidic devices¹. (i) A layer of photoresist and a layer of chromium are laid down onto the surface of glass. (ii) Soluble regions of photoresist are created by the UV exposure, (iii) which is then developed. (iv) after the photoresist is baked for 30 min, the chromium layer is etched away. (v) The exposed glass, now in the pattern of the photomask, is isotropically etched with HF to the desired depth. (vi) After removal of excess photoresist and chromium and drilling of access holes, a second glass slide is thermally bonded to the etched slide at 640 °C for 8 h.

1.2.2 Fabrication of polymeric microfluidic devices

As microfluidic research and development have matured, there has been a shift

from traditional glass microdevices to those constructed with polymeric materials, primarily because of easy fabrication and a decrease in the overall cost.^{2, 3} With the introduction of soft-lithography by Duffy et al., poly(dimethylsiloxane) (PDMS) has become one of the most popular polymeric substrates in academia, owing to the large number of devices that can be rapidly replicated from a master template without the need of expensive clean room facilities.⁴ Nevertheless, applications of PDMS microdevices to routine biological and chemical purposes have been restricted by its mechanical deformability, instability of the surface treatment, gas permeability and absorption of small hydrophobic molecules.⁵

Thermoplastics, such as poly(methyl methacrylate), polycarbonate, cyclo-olefins and polystyrene are economic alternatives to PDMS. The material cost of thermoplastics is generally much lower than the glass or silicon (Table 1-1)⁶. Fabrication of these substrates can benefit from a knowledge base of existing industrial fabrication processes, including multilayer lamination, embossing and injection molding.

Table 1-1: Comparison of microchips made from different substrates.⁶

	Glass microchip	PDMS microchip	PMMA microchip	PeT microchip
Cost per device	~ \$40	~ \$2-5	~ \$5-10	~ \$0.15
Fabrication time	~ 24-48 h	~ 3-4 h	~ 3-5 h	< 10 min
Durability	reusable	reusable	reusable	single use

In addition to the replication-based fabrication, direct machining techniques, such as laser ablation and mechanical micromilling, are also applicable for thermoplastics. More recently, hot roll-to-roll embossing into polymer foil was reported, providing further

reductions in fabrication cost for mass production⁷. A detailed review of various fabrication methods can be found in the recent review articles^{2,8}.

Although the direct machining techniques such as laser ablation and mechanical micromilling are probably not as economic as replication-based fabrication methods for mass production, they provide a way for rapid prototyping (a few hours for a prototype cycle). CO₂ laser ablation is chosen as an exemplary direct machining technique to describe here, as it was utilized for the works in the following chapters.

The ablation mechanism of CO₂ laser is focusing a laser beam at a wavelength of 10.6 μm on the desired section of the thermoplastic surface, causing a rapid rise of temperature at the irradiated spot. The schematic diagram of the laser machining process can be seen in Figure 1-2⁹. Due to the larger thermal input, the material will first melt and then decompose, leaving a void in the workpiece¹⁰. With the assistance of a computer design program, the laser beam can continuously move according to a graphic design with different settings of laser power and speed. In this manner, the moving laser beams can produce a microchannel either by cutting through the pieces or etching a groove on the surface. The accuracy and smoothness of the structure ablated by laser depend not only on the laser optical setting but also on material properties of the chosen material. Common materials used for CO₂ laser ablation

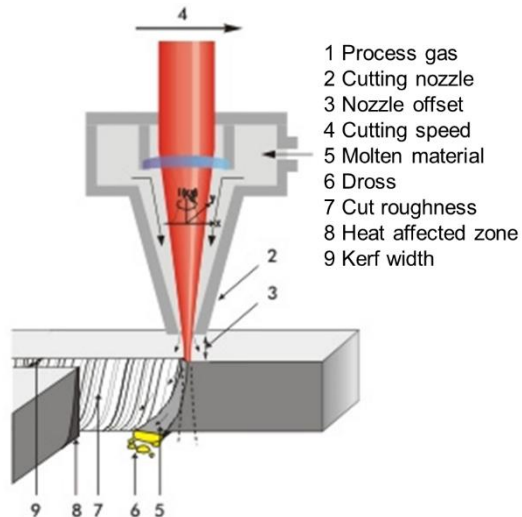


Figure 1-2: Schematic illustration of CO₂ laser ablation⁹. The laser head contains not only a lens to focus the beam onto the workpiece but also a nozzle to direct high pressure gas at the focus.

are poly (methacrylate), polycarbonate and polyester. Various bonding techniques are compatible with the laser ablation process, such as solvent-based bonding, hot lamination and adhesive bonding. The fabrication time for a laser-ablated microdevice mainly depends on the bonding time since the ablation process only takes a few minutes.

1.2.3 Fabrication of polyester-toner microfluidic devices

For the clinical application, single-use microfluidic systems with a cost of a few cents are especially desired to avoid sample contamination between sample runs. One of the simplest and least expensive thermoplastic fabrication approaches involves the use of polyester and, in particular, that found in overhead transparency sheets: poly(ethylene terephthalate). Throughout the work presented in this dissertation, a variety of polyester-based microfluidic devices were designed, fabricated, and utilized. Thus, it is instructive to describe the fabrication concept in this section.

Do Lago et al. were the first to show that black printer toner directly patterned onto the surface of polyester film enables Poly(ethylene terephthalate)-Toner (PeT) microdevices.¹¹ The toner is bifunctional, serving as the adhesive to bond the two layers together and,

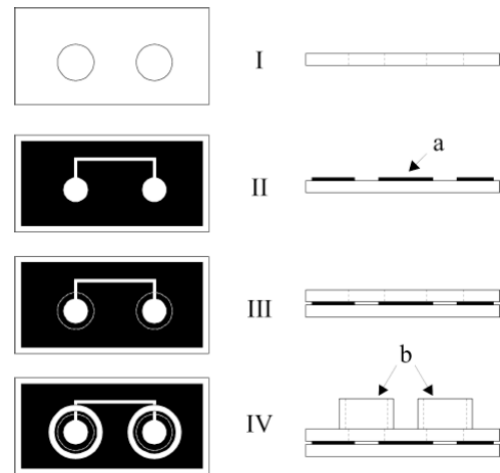


Figure 1-3: Schematic showing two-layer PeT microchip fabrication¹¹: (I) Pe layer; (II) printer toner is laid down to the surface; (III) another Pe layer is laminated with the toner-patterned Pe layer; (IV) the final device with reservoir gluing to the outlet and inlet of the microchannel .

where absent, serving to define the fluidic architecture (Figure 1-3). Fabrication of a PeT microdevice was completed by laminating the printed sheet to either a blank transparency film or a sheet with the mirror image of the device design. Under these conditions, the depth of the microchannel was defined by the thickness of the printer toner, which was $7 \pm 1 \mu\text{m}$ for a single layer of toner ($12 \pm 2 \mu\text{m}$ for two layers). In that work, the PeT microdevice was used for electrophoretic separation of ions with end-channel amperometric detection.

This fabrication method was further improved by Duarte et al. to provide deeper channels so that silica-coated magnetic beads could be integrated into the system for DNA extraction (Figure 1-4)⁶. In that work, one (or more) internal layers of polyester film were laser-ablated and laminated to the toner-patterned layers; again, the toner served as the adhesive but the depth of channel was primarily defined by the number of laser-ablated layers ($\sim 100 \mu\text{m}$ for each internal layer). As a result, they were able to define channels

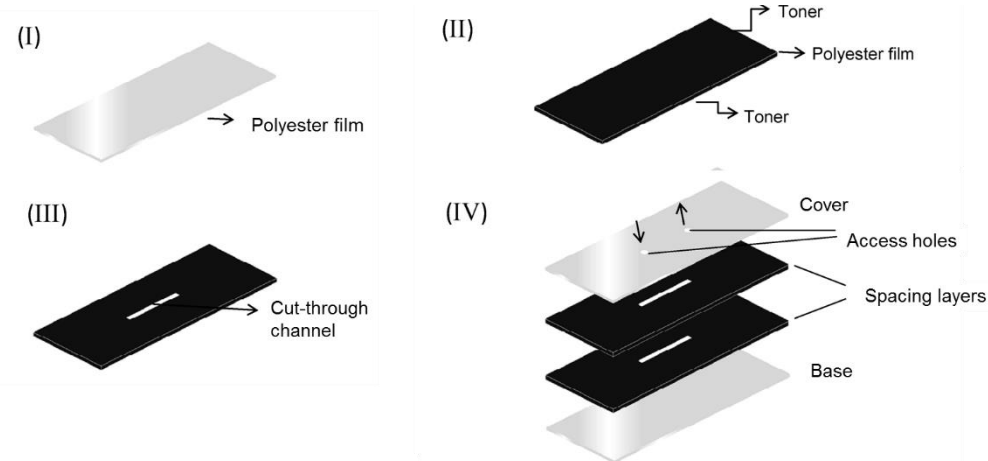


Figure 1-4: Fabrication process for a four-layer PeT microchip⁶. (I) polyester film, (II) polyester film with toner coating on both sides, (III) microfluidic channel cut by laser cutter, (IV) alignment and lamination of four layers (bottom and top enclosing two middle layers with channel); arrows indicate inlet and outlet access.

with adequate depth (~272 μm) for the extraction and amplification of DNA.

1.3 Flow Control in Microfluidic Devices

Since the inception of microfluidics in the 1980's, lab-on-a-chip (LOC) technologies have been increasingly applied to a broad variety of applications including immunoassays^{12, 13, 14}, enzyme assays^{15, 16, 17}, polymerase chain reaction (PCR)^{18, 19}, DNA analysis^{20, 21}, protein separation^{22, 23} and cell analysis^{24, 25}. In 1990's, microfluidic technology significantly decreased sample analysis time by an order of magnitude (e.g., electrophoretic separation), and the volume of reagents for analysis. However, it became clear that expediting the "analytical step" provided only incremental improvement to the overall analysis time when sequential sample preparation steps were involved. Therefore, integration of multiple sample processing steps was critical, and the ability to do so requires that very different chemistries to be physically isolated in the microfluidic architecture of the device, but ultimately connectable when needed.^{26, 27} As a result, this brought to the forefront need for a flow control solution in the microfluidic regime.

1.3.1 Control of fluid propulsion

For an integrated microfluidic system, liquids or samples must be introduced into the reservoir and transported to a series of domains for purification, mixing, and detection. A number of external pumping devices have been developed for microfluidic system, which include syringe, peristaltic pump, acoustic-wave pump, magneto pump, thermal pneumatic pump, electrochemical bubble generation, DC/AC electrokinetics pump,

Table 1-2: Comparison of microfluidics propulsion techniques²⁹.

Fluid propulsion mechanism				
Comparison	Centrifuge	Pressure	Acoustic	Electrokinetic
Valving solved?	Yes for liquids, no for vapor	Yes for liquids and vapor	No solution shown yet for liquid or vapor	Yes for liquids, no for vapor
Maturity	Products available	Products available	Research	Products available
Propulsion force influenced by	Density and viscosity	Generic	Generic	pH, ionic strength
Power source	Rotary motor	Pump, mechanical roller	5 to 40 V	10 kV
Materials	Plastics	Plastics	Piezoelectrics	Glass, plastics
Scaling	L^3	L^3	L^2	L^2
Flow rate	From less than 1 nl s ⁻¹ to greater than 100 μ l s ⁻¹	Very wide range (less than nl s ⁻¹ to liter s ⁻¹)	20 μ l s ⁻¹	0.001–1 μ l sec ⁻¹
General remarks	Inexpensive CD drive, mixing is easy, most samples possible (including cells). Better for diagnostics	Standard technique. Difficult to miniaturize and multiplex	Least mature of the four techniques. Might be too expensive. Better for smallest samples	Mixing difficult. High voltage source is dangerous and many parameters influence propulsion, better for smallest samples (HTS)

centrifuge pump, etc²⁸. Table 1-2²⁹ shows the comparison of the four fluid propulsion means.

Syringe or peristaltic pump has been a traditional pumping method for many integrated microfluidic systems^{27,30} because the technology is well-developed and is commercially available. While they offer a wide range of flow rate with good accuracy, they require seamless connection between the microcomponent (i.e. reservoir on microfluidic devices) and macro-environment (i.e. syringe). This usually requires manual gluing which can consume a large amount of microdevice area if multiple pumping inlets are needed. In addition, considering the footprint and power requirement of the syringe or peristaltic pump, portability of the microfluidic system is questionable.

Electrokinetic pumps are based on the interaction between the working fluid and an electric field. The electrohydrodynamic micropumps are based on the interaction of

electrostatic force with ions in dielectric fluids. Operation of these micropumps requires the existence of space charge in a dielectric fluids, which can be produced because of inhomogeneity in the fluid or though the dissociation or direct charge injection²⁸. The electroosmotic pumping leverages the surface charge that spontaneously develops when a liquid comes in contact with a solid. For both types of pumping methods, only electrodes need to be inserted into the reservoir, hence, connecting microdevice to the pumping system is easy. However, they require voltage supplies ranging from 40 V to 30kV, which can be a potential issue for portability. In addition, the pumping performance is very sensitive to the ionic strengths, pH of the solutions as well as the charges on the surface of the channel wall.

Acoustic streaming pumping is a steady fluid flow formed by viscous attenuation of an acoustic wave. The acoustic wave in the channel is generated by a piezo transducer that is in contact with the microfluidic device. Compared to electrokinetic pumps, the acoustic steaming pumping is insensitive to the chemical nature of the fluids, and therefore can be applied to a wider range of fluids. Nonetheless, the acoustic method is considerably more complex to be implemented and the pumping performance is subjective to the stiffness of device substrate.

In centrifugal pumping, as the microdevices spin, centrifugal force applied on sample fluid drives liquid radially outwards from the spinning center to the perimeter. This centrifugal flow in the microdevice has been well characterized by Madou et al.²⁹ and Duffy et al.²⁶. The average velocity (\bar{v}) of the liquid in a rotating microdevice is given as:

$$\bar{v} = D_b^2 \rho \omega^2 \bar{r} \Delta r / 32 \mu L \quad (1-1)$$

where D_b is the hydraulic diameter of the channel (defined as four times of cross-sectional area to the perimeter of the area), ρ is the density of the liquid, ω is the angular velocity of the rotating microdevice, \bar{r} is the mean radial position of the liquid, Δr is the length of the liquid, μ is the viscosity of the liquid and L is the length of the liquid in the capillary channel (Figure 1-5)²⁹.

The equivalent (external) pressure head (Δp), which corresponds to the pressure difference required to pump a pressure-driven flow at a mean velocity through the same channel, can be calculated by the following equation²⁶:

$$\Delta p = \rho \bar{r} \Delta r \omega^2 \quad (1-2)$$

As it suggested by the Eq (1-2), the flow rate is only dependent on the rotational frequency, physic property of the fluids, the geometry and location of the channel/chamber. Therefore, the centrifugal flow is relatively insensitive to the physicochemical properties such as ionic strength, pH and conductivity.

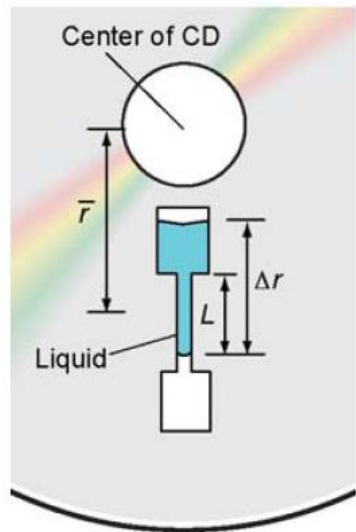


Figure 1-5: Schematic illustrations for the description of flow driven by centrifugal force²⁹.

Due to rotational symmetry of the centrifugal flow, the generic format for a centrifugal microfluidic device is usually a disc-like microchip. Replication of identical microfluidic flow can be easily implemented on a single microfluidic device, thus facilitating the multiplexing of assays while lowering the cost per run. In addition, the control of the centrifugal flow rate on a disc-like microfluidic requires relatively low rotational speed, which can be easily provided by a micromotor in a DVD player. Chapter 3 and Chapter 4 have demonstrated the realization of fluidic control on a disc-like disk using a portable, low-spin micromoter for clinical samples processing.

1.3.2 Valving technology

It has become common to see microfluidic systems described in the literature with a variety of microvalving approaches that serve as a core component for a comprehensive flow control.^{29, 31–33} Disposable microdevices with valving are particularly practical when used for handling biohazardous materials as it provides a ‘closed’ system. Since the first microvalves reported by Terry³⁴ in 1973, there have been more than 200 archival research literature on microvalve solutions³¹. Most of them generally fall into one of the two major categories: mechanical valves and non-mechanical valves.

1.3.2.1 Mechanical valve

The fundamental idea of the mechanical valves is to use mechanical moving parts (usually elastomeric polymeric membrane) to “open” and “close” the channel. Pressure to actuate the moving part can be controlled by magnetic, electric, piezoelectric, thermal, reciprocal moving pump,etc³¹. Figure 1-6³¹ illustrates the actuation principles widely employed in the mechanical microvalve structure. Due to the limited range of suitable materials for the moving parts, the majority of microvalves require costly clean-room dust-free fabrication. In addition, the bulky external devices required to trigger the moving parts increases the complexity of the assay operation. Therefore, the portability and disposability of the integrated microfluidic system using such valves remains a challenge.

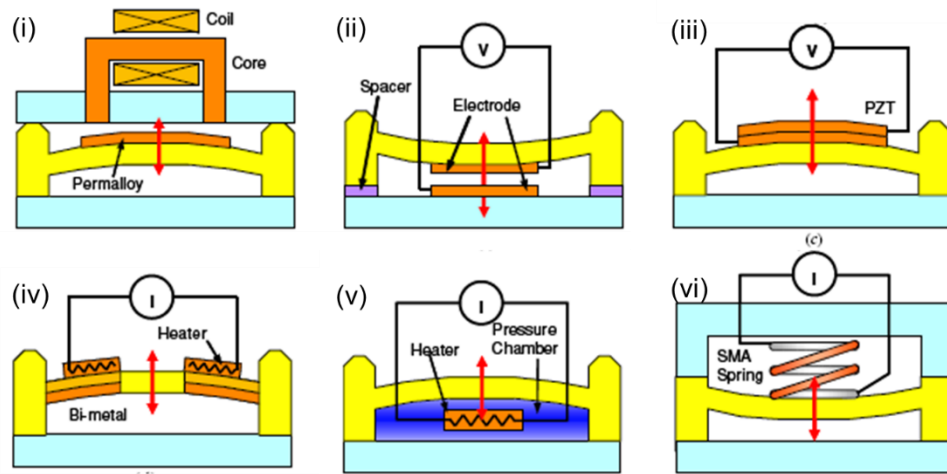


Figure 1-6: Illustrations of several basic actuation principles of active microvalves with mechanical moving parts: (i) electromagnetic; (ii) electrostatic; (iii) piezoelectric; (iv) bimetallic; (v) thermopneumatic and (vi) shape memory alloy actuation ³¹.

1.3.2.2 Non-mechanical valve

Compared to the mechanical valves, the non-mechanical valves appear as a more economical choice since many of them can be used on polymeric microdevices. The two most popular valves , among all, are sacrificial valves and capillary valves. The sacrificial valve can be operated by small or intelligent material such as hydrogel³¹, sol-gel³⁵, wax-based (paraffin, ferrowax)³⁶, and dissolvable film³⁷. In response to the changes in pH, temperature or contacting material, the solid material which acts as a physical gating element is changed or removed. Despite successful miniaturizations of external hardware to actuate sacrificial valves, potential damages from pH and heating to the integrity of biomolecular functionality are always of primary concern when used in biological applications. Furthermore, the fabrication of sacrificial valve are not trivial, as they require a barrier material to be embedded. In addition, the footprints of valving structure and single electronic actuator can limit the space utilization on microchip.

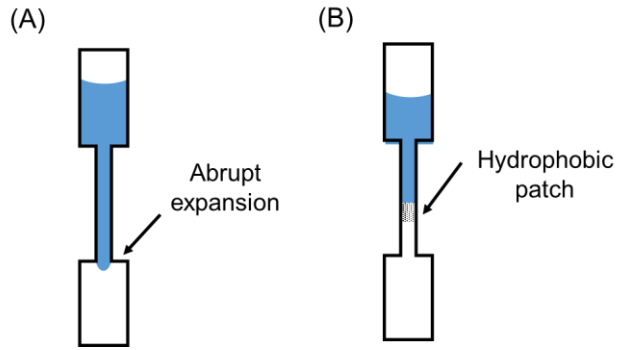


Figure 1-7: Two types of capillary valves: (A) capillary valve stops the liquid by abrupt expansion of the channel dimension, (B) capillary valve stops the liquid by changing the surface wettability.

The capillary valves stop the flow of liquid by giving a simple geometric or surface-chemical variation of the channel (Figure 1-7). In the geometrical capillary valve, the liquid stops to flow due to an abrupt expansion of the channel. In contrast, the surface-

chemical capillary valves (e.g. hydrophobic valves) stop the flow by a sudden change of the wetting properties. To open either capillary valve, it simply requires a driving force to overcome the surface tension of the liquid at the interface. Therefore, only simple supporting instrumentation is needed (e.g. micromoter and syringe pump). One limitation of the geometrical capillary valves is that their high-aspect ratio in structure increases the fabrication cost. Similarly, mass production of surface-chemical capillary valves can also be challenging as they require local surface modification for a very high spatial resolution.

Although each microvalve, as discussed above, has its own advantages, the incorporation of these microvalves more or less complicates the microfabrication and increases the material cost. Therefore, developing a truly cost-effective valve with industrial manufacturability is a significant hurdle for commercialization of integrated microdevices. In Chapter 2, a new methodology was established for massive integration of passive valves with tuneable burst pressure on disposable PeT microfluidic device with minimum addition to the fabrication cost and time.

1.3.3 Mixing technology

Mixing is another important functionality needed in microfluidic devices. Due to the small dimension of microfluidic channel, the flow in microfluidic devices is usually laminar flow (Figure 1-8) featured with a low Reynold number³⁸. Therefore, rapid mixing is difficult to obtain in a straight microchannel even at high flow rates. The micromixers that have been applied to the microdevices can be categorized as passive micromixers and active micromixers³⁹.

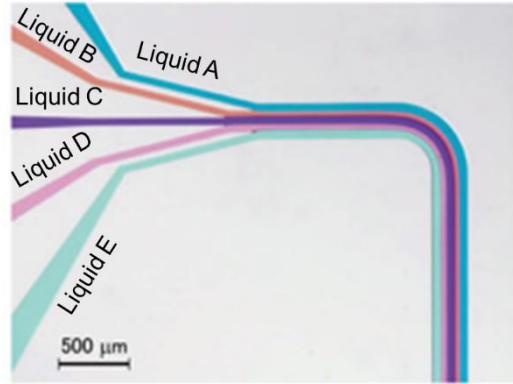


Figure 1-8: Five-layer laminar flow was observed in a microchannel with five inlets for different dye solutions (liquid A-E) injections. The clear boundaries between dyes can still be observed after flowing for several seconds³⁸.

1.3.3.1 Passive mixing

In passive mixing, a micromixer domain is integrated in the flow path to enhance passive mixing either by optimizing the diffusion process or by creating chaotic advection. Based on the structural characteristic of the mixing domain, passive mixers can be further categorized as parallel lamination, serial lamination, injection, chaotic advection and droplet³⁹. Figure 1-9 shows the exemplary structures of parallel lamination and serial lamination. The effectiveness of the above structures all rely on increasing the contact surface between the different fluids and decreasing the diffusion path.

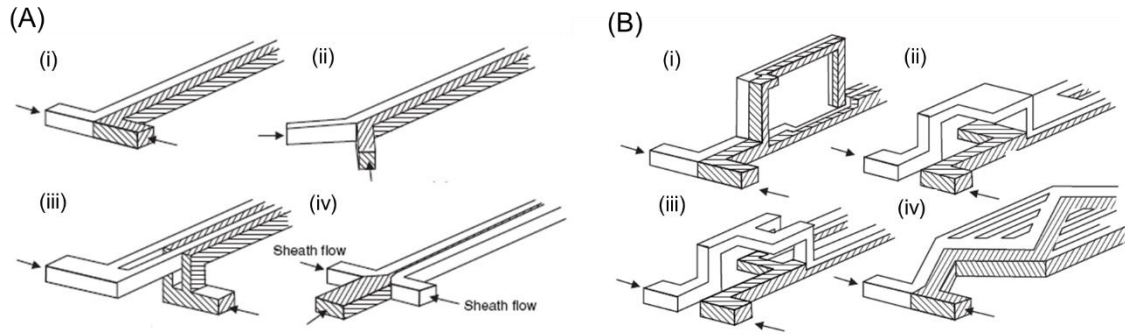


Figure 1-9: Examples of parallel and serial lamination micromixers. (A) Parallel lamination micromixer: (i) the basic T-mixer and (ii) Y-mixer, (iii) the concept of parallel lamination and (iv) the concept of hydraulic focusing; (B) Serial lamination mixer: (i) join–split–join, (ii) split–join, (iii) split–split–join and (iv) multiple intersecting microchannels³⁹.

Besides the diffusion-based passive mixer, the passive mixers based on chaotic-advection can also significantly improve mixing. The chaotic advection mixer relies on special geometries in the mixing channel. For example, placement of physical obstacles in the mixing channel or creating rips and grooves on the channel wall (Figure 1-10) induces advective current in the transversal plane of the fluidic flow³⁹. It is noteworthy that different structural designs are optimized for the flows with different Reynolds numbers.

The advantages of using passive mixing include that (1) no external actuator are required; (2) operation is robust and stable and (3) it can be easily integrated in a more complex system. The obvious downside of using passive mixing is that relatively complicated structures are required, thus, complicating the fabrication.

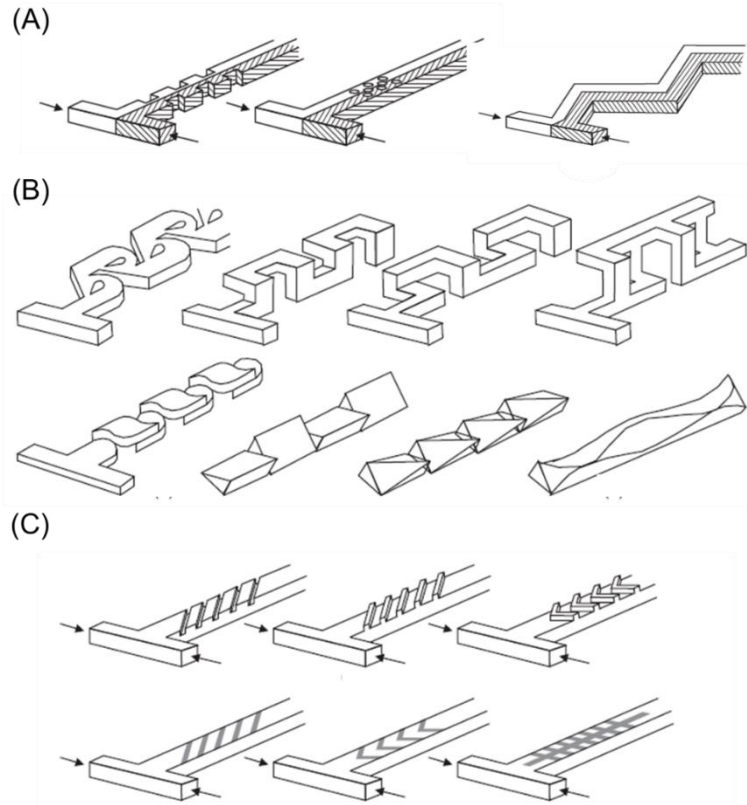


Figure 1-10: Typical structures of chaotic micromixers ³⁹. (A) Planar designs for mixing with chaotic advection at high Reynolds numbers, (B) 3D designs for mixing with chaotic advection at intermediate Reynolds numbers,(C) Modification of mixing channel for chaotic advection at low Reynolds numbers.

1.3.3.2 Active mixing

Active mixing employs the use of an external field to generate disturbance in the flow at certain frequency. Based on the types of external field, the active mixer can be categorized as pressure, temperature, electrohydrodynamics, dielectrophoretic, electrokinetics, magnetohydrodynamics and acoustic³⁹, which are also the common means used in active pumping or mechanical valving. Although the active mixing can be controlled externally, and provide the flexibility of use on different microfluidic devices, the advantage is offset by the complicated microfabrication and external machinary.

Therefore, integrating the active mixer in a microfluidic system can be more expensive than that of passive mixer. Therefore, the availability of simple-control and easy-fabricated micromixer is still in demand by many types of portable microfluidic systems. In chapter 3, a novel micromixer was designed and characterized, which takes advantage of both active and passive mixing mechanisms.

1.4 Visual Detection for Microfluidic System

Visual detection for colormetric assays and turbidimetric assays on microfluidic system has been recently gained attentions⁴⁰⁻⁴⁴ due to the ease of detection. By comparing the changes in color /turbidity of processed samples to a reference chart generated by a set of standard solutions, qualitative (yes/no) or semi-quantitative analyzed results can be interpreted by naked eyes without the need of an external instrumentation. This detection method, therefore, ensures the cost-effectiveness and portability of the microfluidic system. Given that there are numerous popular commercialized paper-based microfluidic devices such as lateral flow strips for infection detections⁴⁵, paper-strip for urine test⁴⁶, etc (Figure 1-11), this visual detection concept has brought great commercial success to microfluidic technology.

With the development and wide popularization of sophisticated yet inexpensive consumer electronics technologies, which are user-friendly with good portability, quantitative analysis for visual detection on microfluidic platform is also feasible. For example, cell phones have been employed to read the results of several colormetric assays on paper-fluidic devices^{17,47,48}. By using the driver's error detection process in a compact

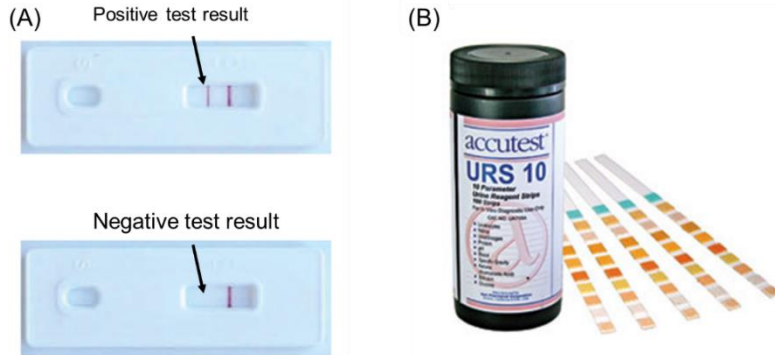


Figure 1-11: Commercialized paper-based microfluidic devices. (A) Rapid immunochromatographic strip tests for sexually transmitted infection. Positive diagnostic results are indicated by the appearance of a red line on the left of the reference line ⁴⁵. (B) Colorimetric assay on strip for urine test ⁴⁶.

disc drive, particles and cells were counted on a disc-like microdevice ⁴⁹. In addition, quantitative detection via a desktop scanner and camera has also been utilized in several reported works ^{49, 56, 51}. Considering that both visual detections, described in Chapter 3 and Chapter 4, were obtained from a desktop scanner (also known as flatbed scanner), this section will be focused on explaining the mechanism of using flatbed scanner for quantitation analysis compatible with microfluidic systems.

A typical optical system in the scanning head of a flatbed scanner is shown in Figure 1-12⁵². A lamp is used to illuminate the object of interest. The images of the object are first reflected by an angled mirror onto another mirror. The surfaces of both mirrors are curved so that after several reflections, a smaller image is focused on a lens. After passing the lens, the image is filtered into red (580-700 nm), green (500-580 nm), and blue (400-500 nm) channels recorded by the charged-coupled-device (CCD) array. The scanner integrates the data from the three parts of the CCD array into a single full-color image. As

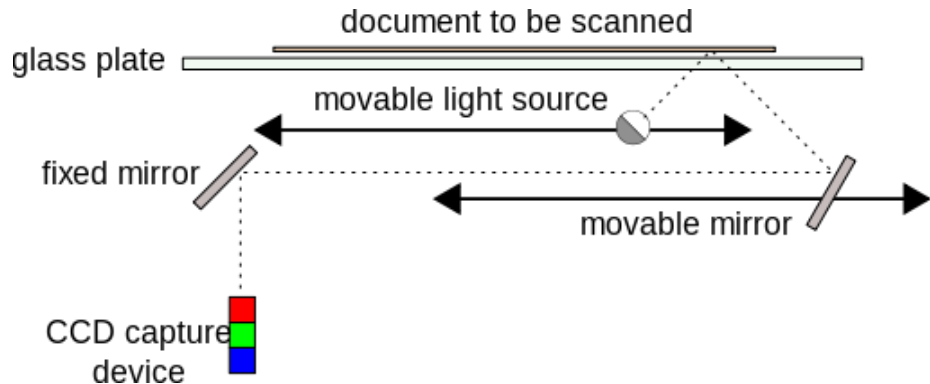


Figure 1-12: Schematic configuration of the moving optical head of flatbed scanner⁵².

a result, RGB (red-green-blue) is the most common color model used by scanner to record image information.

As described above, the functionality of a flatbed scanner has some resemblance to a UV-Vis spectrometer because both of them detect the absorption or transmission of light. However, since the filters from the flatbed scanner have a much lower resolution compared to UV-Vis spectrometer, image analysis can be challenging especially when small color changes are present. Using only one RGB intensity value is not sufficient for quantification. In addition, the RGB model is not intuitive to correlate the RGB values with human perception or visual-light spectrum. For these reasons, alternative image models were introduced with the developed image algorithms for better perception and to compensate the degeneration of the spectrum resolution.

A Hue Saturation Brightness (HSB) model, also known as the HSV model, is one of the most common cylindrical-coordinate-representations of points in an RGB color model (Figure 1-13A)⁵³. The RGB model can be easily converted to the HSB model with

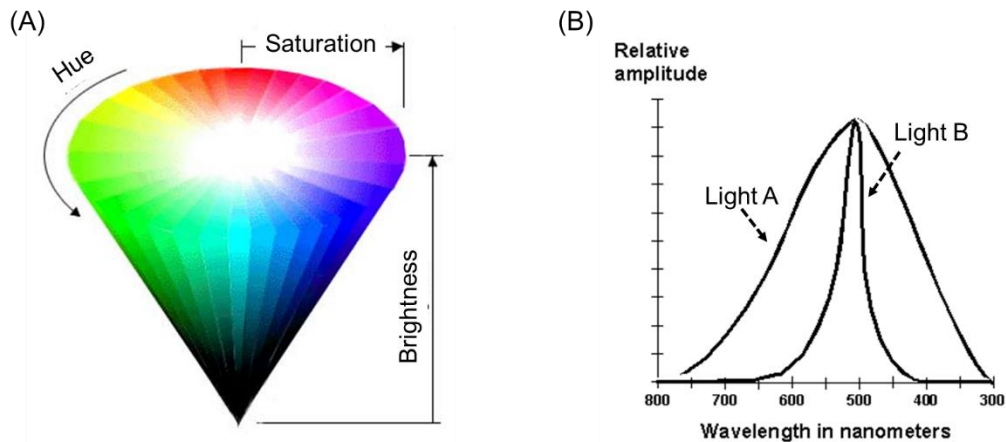


Figure 1-13: Schematic illustration of the HSB model concept. (A) A 3-D graph to illustrate the definition of HSB model⁵³. (B) Correlation between the HSB model to the emission spectrum.

a simple calculation which is introduced in detail elsewhere⁵⁴. The terms in the HSB model can be understood by looking at the visible-light spectrum (Figure 1-13B), where Hue is the wavelength at which the intensity of the light is the greatest. Saturation is defined in terms of the relative bandwidth of the light, as indicated by the steepness of the slopes of the curves in Figure 1-13B. Brightness is a relative expression of intensity of the energy output of a visible light and can be indicated by the amplitude at the wavelength where the intensity is the greatest. As shown in Figure 1-13B, the maximum intensity of both curves is at ~520 nm with same amplitude, therefore the Hue values and Brightness of the two are the same while the Saturation value decreases from light A to light B.

Because the Hue value is an indicator of the wavelength of light, it is typically used in colorimetric assays to quantify the change in color. Henry et.al's work (Figure 1-14) has demonstrated the effectiveness of using the Hue value of the developed color to quantify the level of glucose, lactate, and uric acid in serum and urine samples by using the colormetric assays on paperfluidic microdevice⁴⁴. The advantage of using Hue values is

that, unlike saturation or brightness value, it is not influenced by the change of ambient light when the image is taken, hence the reliable and accurate detection is obtained.

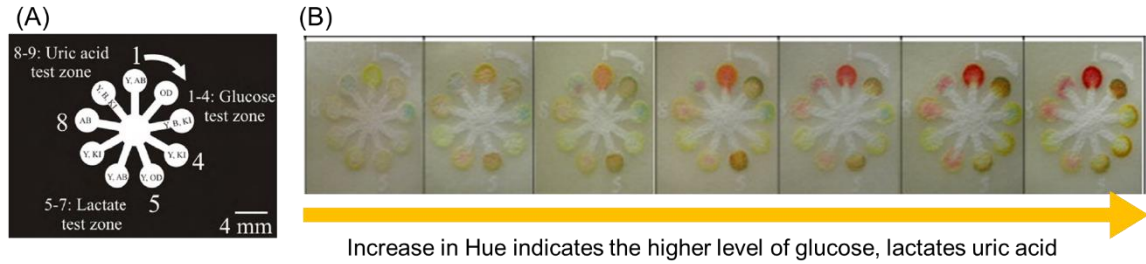


Figure 1-14: Colorimetric assay on paper-based microfluidic devices to perform urine tests⁴⁴.

(A) The device contained different test zones which have been spotted indicators for uric acid, glucose and lactate. (B) Assay colors respond to increasing analyte concentrations.

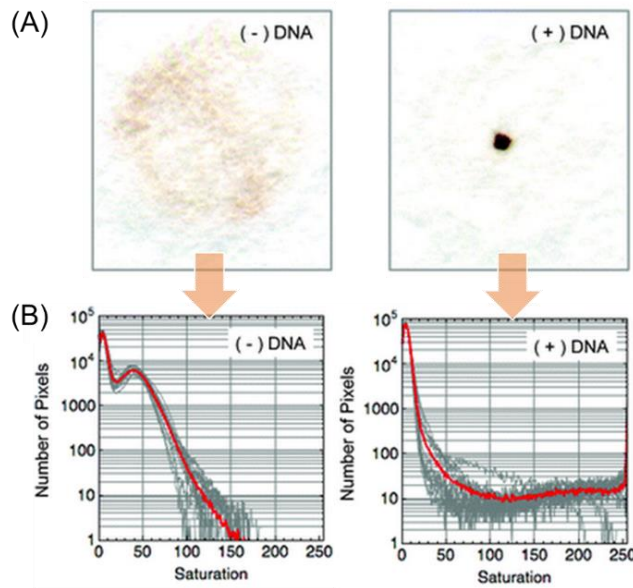


Figure 1-15: A turbidometric assay for DNA quantitation⁵⁵. (A) Without DNA, the silica-coated magnetic beads are dispersed on the paper substrate. In the presence of the DNA, the silica-coated magnetic beads aggregate, maintaining as a cluster on the paper. (B) Image results with DNA or without DNA can be differentiated by looking at Saturation value.

For turbidmetric assays which measure the intensity change of transmitted light due to the suspended/aggregated particles for quantification, the use of Brightness value or Saturation value can be effective to discriminate the particles of interest from the background. Recent work published by Landers group demonstrates successful use of this technique, where an in-house written image algorithm based on Saturation value was developed for the quantitative analysis of a DNA-induced beads aggregation assay on filter paper (Figure 1-15)⁵⁵. It is conceivable that the creative utilization of affordable consumer electronics and image algorithm provide an alternative to conventional spectrometer, will expedite the popularization and commercialization of the diagnostics on microfluidic devices.

1.5 Molecular Diagnostic Techniques

In the past decade, tremendous progress has been made in public health through developing the health care systems (especially in the developed countries) and through popularization of vaccines. Nevertheless, global health burden has been lightly relieved with the reemerging of infectious disease (e.g., malaria, tuberculosis) in developing countries, along with emergence of new diseases (e.g., HIV/AIDS) and other chronic diseases. The percentage of death resulted from various diseases per year is shown in Figure 1-16⁵⁶. It is obvious that accurate identification of patient at the early stage is of great benefit for immediate treatment and infectious disease control. Moreover, suitable means for monitoring chronic diseases are necessary for treatment adjustments or preventive action to minimize medicinal side-effects.

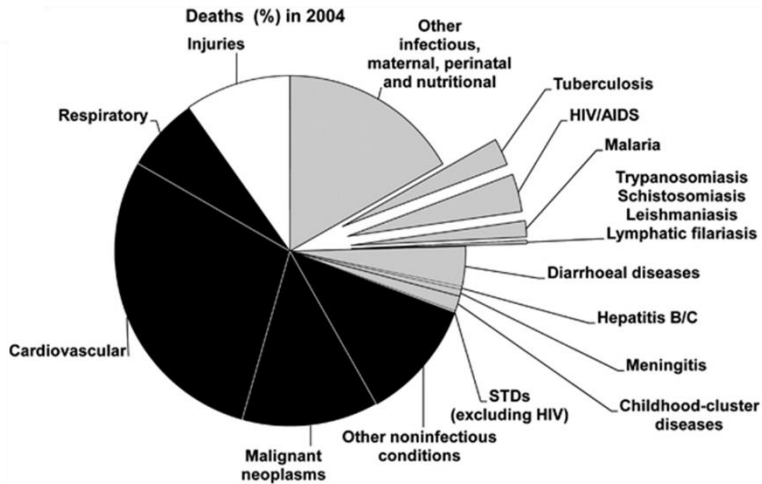


Figure 1-16: A pie chart showing the percentage of death owing to communicable diseases (grey), non-communicable diseases (black) and injury (white) in WHO regions in 2004⁵⁶.

Recent revolutionary progress in human genomics and proteomic has reshaped medical approaches for therapy and diagnosis. The genomic diagnostic tests detect specific sequences in DNA or RNA that are not only associated with inherited genetic disease but might also be involved in the neoplastic and infectious processes. Detection of nucleic-acid-based target sequence, prior to its protein expression provides opportunities to identify the diseases at very early stage when no symptoms are observed. In addition, with the introduction of polymerase-chain-reaction (PCR) technology, genomic diagnostic tests can be ultra-sensitive. For example, an RNA assays has been reported to detect 12 HIV viral copies per milliliter⁵⁷.

The PCR technology employs thermally-stable polymerase enzymes to catalyze the amplification of DNA sequence of interest *in vitro*. The reaction process is controlled by varying temperature in each step (Figure 1-17¹). A conventional PCR reaction is carried out in a thin-walled polypropylene tube with a reaction volume ranging from 15-100 μL . The tube is inserted into a metal plate in the thermal cycler which provides contact heating and cooling. The PCR usually consists of 20-40 cycles of 2-3 temperature steps between 50-95 °C. In the first step, also known as the denaturation step (typically temperature is set to 90-95 °C), double-strand DNA is separated into two single strands. Next, the solution is cooled to the annealing temperature (between 55-68 °C) so that primers can bind to the complementary region of the single strand mother DNA template. The solution is then heated to the optimal extension temperature of *Taq* polymerase (72 °C) to synthesize a new DNA strand complementary to the DNA template strand by adding deoxynucleotide triphosphates (dNTPs) that are complementary to the template. Therefore, if we assume the 100% efficiency of the reaction, the number of DNA templates double after the first cycle of the above mentioned steps. In theory, if the process is repeated for 30 times, 1.1 billion copies of the DNA fragment of interest from the only one starting copy of template will be created with a typical reaction time between 60-120 minutes in conventional

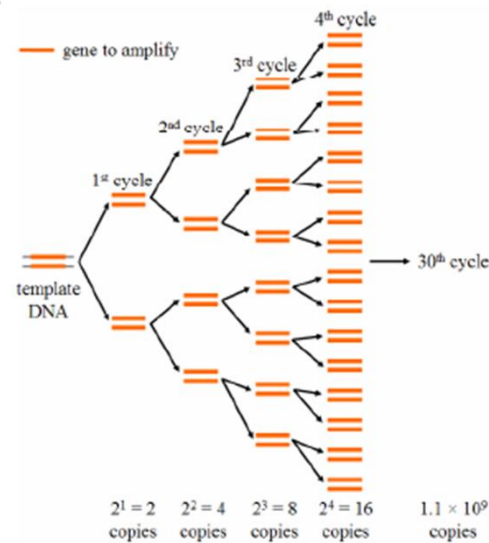


Figure 1-17: Schematically showing the exponential amplification nature of PCR¹.

thermal cycler. The actual efficiency of the PCR is subject to a number of factors such as accurate temperature control, primer design, bioactivity of *Taq*, chemical inhibitors, etc. Miniaturization of PCR on the microfluidic device will be discussed in Chapter 5.

Although genetic diagnosis is very sensitive, it is usually very expensive, limiting its availability in the low-income countries. Moreover, because it requires well-trained personnel, daily use for self-health monitoring remains difficult. In contrast, diagnostic assays based on detecting protein markers have shown great potential to be used as an affordable, easily operative and rapid assay with acceptable sensitivity and specificity. For example, the Whiteside's group developed a paperfluidic device for liver function monitoring with a cost of a couple of cents by measuring the markers of liver diseases in a drop of blood through colorimetric assays¹⁷. By using antibodies to capture the target markers and color changes as a capture-event signal, the enzyme-linked immunosorbent assays (ELISA) have been successfully utilized for pregnancy test and diagnosis for infectious disease such as HIV/AIDS, malaria, *salmonella Typhi* LPS and etc^{32,45}.

1.6 Concluding Remarks

With the fundamental concepts and background outlined in this chapter, the following chapters will address the challenges in fabrication, integration of flow controls and detection, which are the key steps to the commercialization of the microfluidic devices. In Chapter 2, a cost-effective and rapid fabrication method for integrating passive valves is depicted, based on interfacial phenomena and printing lithography technique. Together with the novel micromixer developed in Chapter 3, an automated system for

comprehensive liquid handling on a rotation-driven PeT microdevice was developed for protein quantitation. In Chapter 4, the fluidic control platform was adopted for multiplexing a beads-based cell quantitation assay. A flatbed scanner was proven to be an effective detection means. Chapter 5 presents a new type of microfluidic device for infrared mediated control PCR amplification which broadens the vision of disposable microdevice substrate for genetic analysis. Finally, concluding remarks for the works presented in this dissertation and future prospective are discussed in Chapter 6.

1.7 Reference

1. C. J. Easley, Univeristy of Virginia, 2006.
2. F. Reymond and P. E. Michel, *Polymer (Guildf.)*, 2002, 858–867.
3. C.-W. Tsao and D. L. DeVoe, *Microfluid. Nanofuidics*, 2008, **6**, 1–16.
4. D. C. Duffy, J. C. McDonald, O. J. Schueller, and G. M. Whitesides, *Anal. Chem.*, 1998, **70**, 4974–84.
5. W. K. T. Coltro, S. M. Lunte, and E. Carrilho, *Electrophoresis*, 2008, **29**, 4928–37.
6. G. R. M. Duarte, C. W. Price, B. H. Augustine, E. Carrilho, and J. P. Landers, *Anal. Chem.*, 2011, 5182–5189.
7. S. Miserere, G. Mottet, V. Taniga, S. Descroix, J.-L. Viovy, and L. Malaquin, *Lab Chip*, 2012, **12**, 1849–56.

8. C.-W. Tsao and D. L. DeVoe, *Microfluid. Nanofluidics*, 2008, **6**, 1–16.
9. <http://www.rofin.co.uk/applications/laser-cutting>
10. H. Klank, J. P. Kutter, and O. Geschke, *Lab Chip*, 2002, **2**, 242–6.
11. C. L. do Lago, H. D. T. da Silva, C. A. Neves, J. G. A. Brito-Neto, and J. A. F. da Silva, *Anal. Chem.*, 2003, **75**, 3853–8.
12. J. Park, V. Sunkara, T.-H. Kim, H. Hwang, and Y.-K. Cho, *Anal. Chem.*, 2012, **84**, 2133–40.
13. B. S. Lee, Y. U. Lee, H.-S. Kim, T.-H. Kim, J. Park, J.-G. Lee, J. Kim, H. Kim, W. G. Lee, and Y.-K. Cho, *Lab Chip*, 2011, **11**, 70–8.
14. S. Lai, S. Wang, J. Luo, L. J. Lee, S.-T. Yang, and M. J. Madou, *Anal. Chem.*, 2004, **76**, 1832–7.
15. D. C. Duffy, H. L. Gillis, J. Lin, N. F. Sheppard, G. J. Kellogg, G. Bioscience, and B. Avenue, *Anal. Chem.*, 1999, **71**, 4669–4678.
16. M. Grumann, J. Steigert, L. Rieger, I. Moser, B. Enderle, K. Riebeseel, G. Urban, R. Zengerle, and J. Ducr ée, *Biomed. Microdevices*, 2006, **8**, 209–14.
17. S. J. Vella, P. Beattie, R. Cademartiri, A. Laromaine, A. W. Martinez, S. T. Phillips, K. A. Mirica, and G. M. Whitesides, *Anal. Chem.*, 2012, **84**, 2883–91.
18. Y. Zhang and P. Ozdemir, *Anal. Chim. Acta*, 2009, **638**, 115–25.

19. M. Focke, F. Stumpf, B. Faltin, P. Reith, D. Bamarni, S. Wadle, C. Müller, H. Reinecke, J. Schrenzel, P. Francois, D. Mark, G. Roth, R. Zengerle, and F. von Stetten, *Lab Chip*, 2010, **10**, 2519–26.
20. E. T. Lagally, C. A. Emrich, and R. A. Mathies, *Lab Chip*, 2001, **1**, 102–7.
21. M. J. Heller, *Annu. Rev. Biomed. Eng.*, 2002, **4**, 129–53.
22. H. Yu, Y. Lu, Y. Zhou, F. Wang, F. He, and X. Xia, *Lab Chip*, 2008, **8**, 1496–501.
23. Z. Zhu, J. J. Lu, and S. Liu, *Anal. Chim. Acta*, 2012, **709**, 21–31.
24. J. Gao, X.-F. Yin, and Z.-L. Fang, *Lab Chip*, 2004, **4**, 47–52.
25. S. Lindström and H. Andersson-Svahn, *Lab Chip*, 2010, **10**, 3363–72.
26. J. Ducr  , S. Haeberle, S. Lutz, S. Pausch, F. Von Stetten, and R. Zengerle, *J. Micromechanics Microengineering*, 2007, **17**, S103–S115.
27. C. J. Easley, J. M. Karlinsey, J. M. Bienvenue, L. A. Legendre, M. G. Roper, S. H. Feldman, M. A. Hughes, E. L. Hewlett, T. J. Merkel, J. P. Ferrance, and J. P. Landers, *Proc. Natl. Acad. Sci. U. S. A.*, 2006, **103**, 19272–7.
28. D. J. Laser and J. G. Santiago, *J. Micromechanics Microengineering*, 2004, **14**, R35–R64.
29. M. Madou, J. Zoval, G. Jia, H. Kido, J. Kim, and N. Kim, *Annu. Rev. Biomed. Eng.*, 2006, **8**, 601–28.

30. J. a Lounsbury, A. Karlsson, D. C. Miranian, S. M. Cronk, D. a Nelson, J. Li, D. M. Haverstick, P. Kinnon, D. J. Saul, and J. P. Landers, *Lab Chip*, 2013, **13**, 1384–93.
31. K. W. Oh and C. H. Ahn, *J. Micromechanics Microengineering*, 2006, **16**, R13–R39.
32. C. D. Chin, V. Linder, and S. K. Sia, *Lab Chip*, 2007, **7**, 41–57.
33. R. Gorkin, J. Park, J. Siegrist, M. Amasia, B. S. Lee, J.-M. Park, J. Kim, H. Kim, M. Madou, and Y.-K. Cho, *Lab Chip*, 2010, 1758–1773.
34. Y. Goldstein, N. B. Grover, C. Chang, A. Jelli, J. Andre, P. Mark, and A. Goodwin, 1979, 1880–1886.
35. B. H. Park, J. H. Jung, H. Zhang, N. Y. Lee, and T. S. Seo, *Lab Chip*, 2012, **12**, 3875–81.
36. K. Abi-Samra, R. Hanson, M. Madou, and R. a Gorkin, *Lab Chip*, 2011, **11**, 723–6.
37. R. Gorkin, C. E. Nwankire, J. Gaughran, X. Zhang, G. G. Donohoe, M. Rook, R. O’Kennedy, and J. Ducr  , *Lab Chip*, 2012, **12**, 2894–902.
38. C. D. Chin, V. Linder, and S. K. Sia, *Lab Chip*, 2007, **7**, 41–57
39. N.-T. Nguyen and Z. Wu, *J. Micromechanics Microengineering*, 2005, **15**, R1–R16.
40. C. V Sapan, R. L. Lundblad, and N. C. Price, *Biotechnol. Appl. Biochem.*, 1999, **29** (Pt 2), 99–108.

41. W. G. Cao, Q. C. Jiao, Y. Fu, L. Chen, and Q. Liu, *Spectrosc. Lett.*, 2003, **36**, 197–209.
42. V. Vichai and K. Kirtikara, *Nat. Protoc.*, 2006, **1**, 1112–6.
43. W. Wang, W.-Y. Wu, and J.-J. Zhu, *J. Chromatogr. A*, 2010, **1217**, 3896–9.
44. W. Dungchai, O. Chailapakul, and C. S. Henry, *Anal. Chim. Acta*, 2010, **674**, 227–33.
45. P. Yager, T. Edwards, E. Fu, K. Helton, K. Nelson, M. R. Tam, and B. H. Weigl, *Nature*, 2006, **442**, 412–8.
46. <http://www.microfluidics.iis.u-tokyo.ac.jp/r08002.html>
47. A. F. Coskun, R. Nagi, K. Sadeghi, S. Phillips, and A. Ozcan, *Lab Chip*, 2013.
48. L. Shen, J. a Hagen, and I. Papautsky, *Lab Chip*, 2012, **12**, 4240–3.
49. S. M. Imaad, N. Lord, G. Kulsharova, and G. L. Liu, *Lab Chip*, 2011, **11**, 1448–56.
50. R. S. J. Alkasir, M. Ornatska, and S. Andreeescu, *Anal. Chem.*, 2012, **84**, 9729–37.
51. D. C. Leslie, J. Li, B. C. Strachan, M. R. Begley, D. Finkler, L. a L. Bazydlo, N. S. Barker, D. M. Haverstick, M. Utz, and J. P. Landers, *J. Am. Chem. Soc.*, 2012, **134**, 5689–96.
52. http://en.wikipedia.org/wiki/File:CPT_Hardware-Input-scanner-flatbed.svg
53. <http://rudocs.exdat.com/docs/index-315478.html>

54. http://whatis.techtarget.com/definition/hue-saturation-and-brightness
55. J. Li, Q. Liu, H. Alsamarri, J. a Lounsbury, D. M. Haversitick, and J. P. Landers, *Lab Chip*, 2013, **13**, 955–61.
56. K. T. Andrews, A. Haque, and M. K. Jones, *Immunol. Cell Biol.*, 2012, **90**, 66–77.
57. J. M. Barletta, D. C. Edelman, and N. T. Constantine, *Am. J. Clin. Pathol.*, 2004, **122**, 20–27.

Chapter 2: Rapid and Direct Patterning of ‘Tunable’ Hydrophobic Valves on Disposable Microchips by Laser Printer Lithography

2.1 Introduction

Valving is a key component for the flow control in the integrated microfluidic system. However, manufacturing disposable microdevice with reliable microvalves at an economically-viable cost has been one of the bottlenecks for commercializing the LOC technologies. Desirable features of a disposable microdevice with integrated microvalves include those: (1) fabricated with substrate that is cost-effective, (2) compatible with current industrial microdevice manufacturing techniques, (3) easily integrated in the manufacturing process, and (4) not reliant on external hardware but preferably, use of passive valving mechanisms.

PeT microdevices is a promising candidates as disposable devices, since it fulfils the first three requirements mention above as discussed in Chapter one. With its nonbiofouling for biological samples and desirable optical property used for visual detection, PeT microchip has been successfully utilised for many biological applications including inducing passive mixing¹, studying the kinetics of enzymatic reactions², rapid protein concentration and purification³, DNA extraction and electrophoretic seperation. However, it is noteworthy that all of the previous work utilising PeT microchip were applied to one-step chemistries (e.g., single reagent delivery). The use of PeT microchip as integrated microfluidic device has been hindered by the lack of flow control.

The reasons that valving has not been demonstrated on PeT microdevices are the fabrication challenges and the possibility of trading off its inexpensive nature. For example, it is challenging to incorporate into a PeT microdevice the type of mechanically-driven active valves that have been a cornerstone for PDMS microdevices, primarily because the required feature size that would prevent microchip debonding is excessively large (i.e., the fluidic resistance of the valve has to be kept small, because the bonding is relatively weak). Non-mechanical active valves, such as phase-change valves (i.e., hydrogel-based⁴, paraffin-based⁵, dissolvable film coupled with centrifugal-pneumatic valves⁶) are a possibility but can malfunction due to thermal- and pressure-induced failure modes during the final lamination step. Moreover, the incorporation of either type of valve necessitates the embedding of a different barrier material, thus, complicating the fabrication. In addition, with the exception of dissolvable film/centrifugal-pneumatic valves³⁴, the actuation of such valves generally requires external energy input, again increasing the complexity of operation and potential portability.

Geometrical capillary valves can be easily fabricated and only requires sufficient driving force to overcome the surface tension of the liquid where the channel dimensions expand. Its operational ‘burst pressure’ is determined by the aspect ratio of the channel structures, which, in this case, is limited by the resolution for laser ablation (~100 µm) and bonding process (lamination). This creates potential hurdles for accurate fabrication of geometric capillary-type valves for fluid flow control. As a result, PeT as substrate has not been as widely-utilized for microchip fabrication as other thermoplastics (e.g., PMMA or PC) materials that ultimately are substantially more costly.

The work in this chapter provide the first valving solution for integrating fluidic

control functionality into PeT microdevices, while keeping the fabrication process, that is ‘print, cut and laminate’, as simple as it was defined by do Lago et al.⁷ More specifically, hydrophobic valves have been patterned onto the polyester film by laser printing lithography, and these function as passive valves. In addition to showing how these devices can be fabricated, this chapter also discusses the fundamental principles behind using a conventional laser printer to control the degree of hydrophobicity/hydrophilicity of the surface, and the effect of valve surface character on burst pressure. Both the theoretical model and experimental results suggest that the burst pressure of the valve is defined by the density of the toner particles on the film, which is simply controlled by the gray-scale in the printing setting. Finally, advanced control of sequential fluidic manipulation processes driven by centrifugal force was demonstrated by the toner-based hydrophobic valves to provide. Since this fabrication method is compatible with the current fabrication approaches for creating PeT microdevices, it presents an interesting potential for developing PeT microchips as low-cost microfluidic-based diagnostic devices in resource-limited areas.

2.2 Theory

2.2.1 Burst pressures associated with printed features

The *Material Safety Data Sheet* (MSDS) for the polyester transparency film used in this work (CG5000, 3M) indicates that the surface coating contains silica, and this is likely responsible for rendering the surface hydrophilic (Figure 2-1A). Conversely, the printer toner particles are primarily wax-based⁷ and, if patterned on the surface, should increase the hydrophobic character (Figure 2-1B).

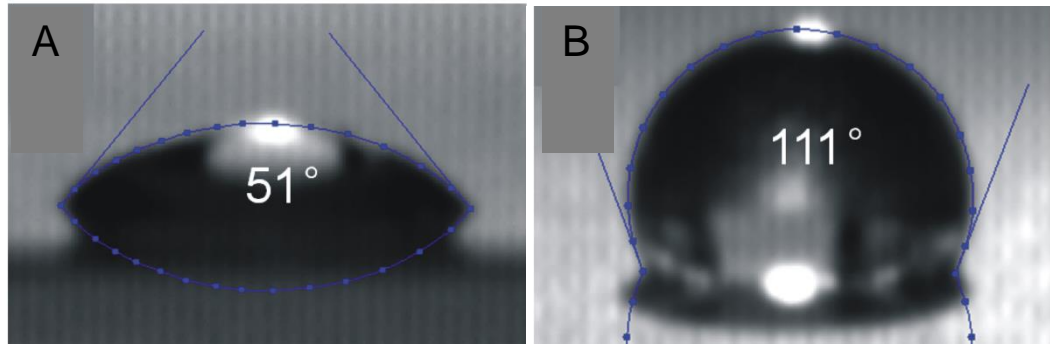


Figure 2-1: Controlling the hydrophobicity of the poly(ethylene terephthalate) film. Photographic images of deionized water ($3 \mu\text{L}$) on (A) the surface of unpatterned transparency film and (B) transparency film with a single layer of toner, respectively.

As expected, the degree of hydrophobicity imparted to the transparency film surface by micropatterning with toner is revealed by a change in the contact angle as the composition of the heterogeneous solid surface is altered. In many instances, the effective wetting angle of a patterned surface can be described by a simple rule of mixtures (i.e. Cassie's equation), as in:

$$\cos \theta_p = f \cos \theta_t + (1 - f) \cos \theta_f \quad (2-1)$$

where $\cos \theta_t$ is the contact angle of the toner, $\cos \theta_f$ is the contact angle of the native transparency film, and f is the area fraction of toner coverage. This suggests that the hydrophobicity of a patterned surface (θ_p) can be directly controlled by using toners with different wetting properties and/or by modulating the area fraction of coverage using the printer's gray scale.

In the following, a hydrophobic valve by printing toner patches were constructed at various gray scales on the top and bottom of a channel formed by the lamination process, as shown in Figure 2-2. Fluid easily flows to the leading edge of the patterned feature due

to the hydrophilic nature of the PeT surface (Fig.2-3). Additional pressure is needed to drive the fluid front past the leading edge of the patterned section. The pressure change across the meniscus (when located on the toner patch) associated with equilibrium (i.e. force balance) is given by:

$$\Delta P = 2\gamma \left(\frac{\cos \theta_w}{w} + \frac{\cos \theta_p}{h} \right) \quad (2-2)$$

where γ is the surface tension of the liquid, h is the height of the channel, w is the channel width, $\cos \theta_w$ is the contact angle of the fluid on the side walls, and again, $\cos \theta_p$ is the contact angle associated with the patterned surface on top and bottom of the channel [given by Eq (2-1)]. From a theoretical perspective, the apparent dynamic contact angle that exists

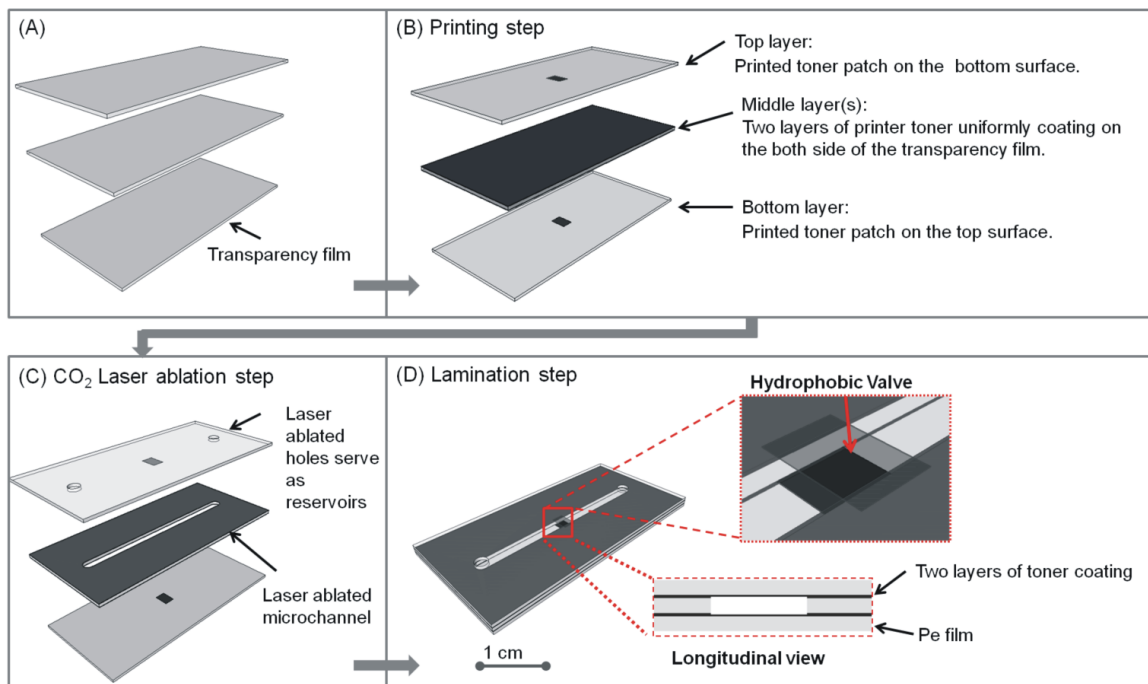


Figure 2-2: Steps involved in the fabrication of a PeT microdevice with hydrophobic toner-based valves. (A) three layers of transparency film, (B) patterning toner onto the both sides of the middle layer and hydrophobic patches on the top and bottom layers, (C) microfeatures cut by laser cutter in to middle layers and, (D) alignment of all layers for lamination.

as the meniscus is advanced by pressure (which is close to the ‘critical advancing contact angle’) should be used Eq (2-2).⁸ The ‘critical advancing contact angle’ is the contact angle at which the contact line of liquid/solid begins to move, which is usually greater than the static contact angle (also known as Young-equilibrium contact angle).⁹

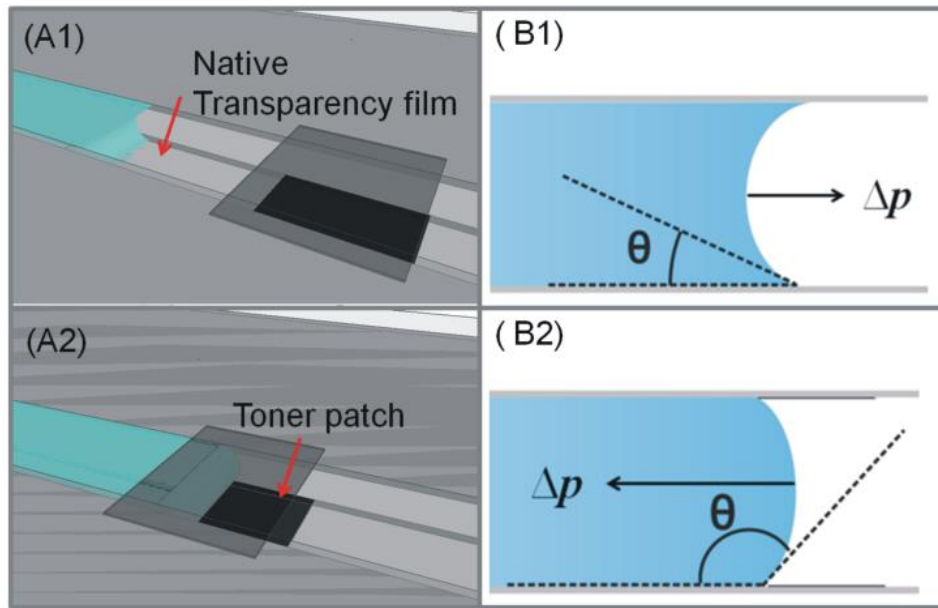


Figure 2-3: Configuration and valving mechanism with a toner-based valve. (A) A 3D rendering showing liquid priming the channel with either a hydrophilic ceiling surface (A1) and hydrophobic ceiling surface (A2). (B) A schematic showing wetting interactions with the polyethylene surface without (B1) and with (B2) toner patterning.

Since the sidewall was composed of alternating layers of laser-ablated poly(ethylene terephthalate) and toner strips (Fig.2-2 D), in principle, the contact angle of the fluid on the side walls could be calculated from the application of rule of mixtures, as done for the patterned surface. However, the laser cutting process significantly alters the surface on the

cut edge of the transparency film (which forms the side wall), such that details of the final side-wall geometry following lamination are difficult to quantify. As such, direct measurements of the pressure needed to stop fluid advancing in the channel without a toner patch were employed to determine the effective contact angle of the side walls using Eq (2-2), with $\cos\theta_f$ replacing $\cos\theta_p$ (since there is no patch in these experiments).

It is clear that the burst pressure for the toner-based valves can be tuned by three parameters (1) the physical dimensions of the valve (2) the hydrophobicity of the coating material, and (3) the fractional area of the coating material. Compared with common geometrical capillary valves^{10, 20, 21}, of which the control of the burst pressure relies on no more than two parameters (i.e., the geometry or one invariable hydrophobic property), the use of laser printer lithography technology significantly reduces the dependence on fabrication precision while expanding the operational burst pressure bandwidth. The latter is particularly valuable for application to centrifugal systems and is further discussed below.

2.2.2 Burst frequency on a centrifugal system associate with printed features

Considering the radial pressure distribution on the centrifugal system, Eq (2-3) was used to estimate the pumping pressure generated by centrifugal force¹³ :

$$\Delta P = \rho\omega^2(R_2 - R_1) \cdot \left(\frac{R_2 + R_1}{2}\right) = \rho\omega^2 \cdot \Delta R \cdot \bar{R} \quad (2-3)$$

where ρ is the density of the liquid, ω is the angular velocity of the disc, R_1 and R_2 are the two distances of liquid from the disc center, and ΔR is equal to $R_2 - R_1$ while \bar{R} is equal to $(R_2 + R_1)/2$. Even though it has been successfully applied to predict the burst frequency of

other surface tension-based valves^{14, 15}, it is noteworthy that the pressure calculated from Eq (2-3) is the equivalent pressure head needed to pump solution in pressure-driven flow at the same flow velocity. Due to the nonuniform centrifugal force density along the radius, the pressure calculated by Eq (2-3) can deviate slightly from the actual pressure that liquid meniscus experienced at the toner patch.¹³

For the geometry of the channel discussed in this paper, having uniform width and depth, the minimum theoretical pressure to force the liquid of a finite length flowing through this normally ‘closed’ valve can be calculated by:

$$\Delta P = P_1 - P_2 \quad (2-4)$$

where P_1 is the pressure generated on liquid meniscus at the end of the advancing liquid plug on native transparency film and P_2 is the pressure generated on the front meniscus of advancing liquid plug on hydrophobic toner patterned surface, both of which can be calculated by using Eq (2-2).

By combining Eq (2-2), Eq (2-3) and Eq (2-4), the required burst frequency in revolution per minute (RPM) can be calculated by Eq (2-5).

$$f(\text{Hz}) = \frac{30}{\pi} \sqrt{\frac{2\gamma f(\cos \theta_f - \cos \theta_p)}{\rho h \Delta R \bar{R}}} \quad (2-5)$$

2.3 Material and Methods

2.3.1 Reagents

2% (wt/wt) bovine serum albumin (Sigma) was prepared by dissolving in PBS

buffer (pH=7.4, 10 mM). 10×PCR buffer (Fisher Scientific) was diluted by 10 fold with distilled water. All other reagents are analytical grade and used without further purification. pH of the solution was measured by a Mettler Toledo MP 220 pH meter.

2.3.2 Fabrication of the hydrophobic patches

Commercially available poly(ethylene terephthalate transparency sheets were used for the base substrate (CG5000, 3M). The thickness of the Pe film was determined to be $110 \pm 2 \mu\text{m}$ thick by a micrometer (IP54, Craftsman) ($n=5$). The patterns for hydrophobic valves were printed on the transparencies using a laser printer with graphic software control. To compare toners from different brands, the setting for the HP laser printer (HP Laserjet 4000) was chosen as ‘600 dpi’ using black toner cartridge (HP C-4127X) and the setting for the Brother printer (Brother HL4070-CDW) was chosen as ‘output of RGB for bitmap’ and ‘600 dpi’ for four different toner colors (BR-TN-110 Yellow, TN-135 Black, TN-135 Magenta and TN-110 Cyan cartridges). In the evaluation of the efficiency by using gray-scale level control to tuning the hydrophobic surface, only HP laser printer was used to print transparencies with different gray-scale level settings (from 10% to 100 % in increments of 10 %). After printing, the surface was cleaned by filtered air and did not undergo any further treatment. The thickness of the 100% gray-scale toner patch was measured to be $7 \pm 1 \mu\text{m}$.

2.3.3 Contact angle measurement

To examine the surface wettability (hydrophobicity), the ternary-phase contact

angles of sessile liquid samples (3 μL) on the prepared surfaces were measured under room temperature and pressure on a custom-built, vibration-free test bed. Images of the droplets were captured using an AVT Guppy NIR CCD color camera with a 9.8-77 mm video zoom lens (Edmund Optics) and a light diffuser. The captured images were processed by ImageJ with the Dropsnake and LB-ADSA plugins, in which contact angles on the left and right side of each droplet were measured and averaged. Three replicate droplets of each sample were measured.

2.3.4 Image analysis to quantitate the fractional area of toner printed at different gray-scale level

Image of the prepared transparency films were magnified by 20 fold under a microscope (Axio Scope A1, ZEISS) and captured by a camera with CMOS sensor (PL-B681CU, PixeLINK). TIF image files were processed into binary with the gray level threshold set by an isodata algorithm written in Mathematica software. The fractional area of toner was obtained by dividing the number of dark pixels over the total number of pixels.

2.3.5 Fabrication of toner-based valves on PeT microdevices

For the fabrication of PeT microdevices described in the literature to-date^{16, 3, 7, 1, 2}, a dense layer of toner is patterned by a laser printer selectively on the transparency sheets to serve as an adhesive to bond the two layers together. This very same fabrication process is obviously compatible with the step needed to incorporate toner-based valves by precisely patterning toner (at predetermined densities) in select locations in the microchannel. The method described by Duarte *et al.* for PeT chip fabrication¹⁶ was modified, as it yielded

microchannel depths functional and comparable to those applications utilized in many microfluidic devices (e.g., glass, PDMS, PMMA) reported for biological assays.^{17, 18, 19} The main fabrication steps are shown schematically in Figure 2-2. First, only the underside of the top (L1) and topside of bottom (L3) transparency layers were selectively patterned with toner [3 mm (w) \times 2 mm (l) patches] to define the hydrophobic valve, while both sides of middle transparency layer (L2) were uniformly coated by two layers of printer toners (the final thickness of the middle layer after printing was measured to be $132 \pm 3 \mu\text{m}$). The L1 and L2 layers were then ablated by a CO₂ laser system according to the design: access holes are cut through L1 as reservoirs and the microchannel out of L2 to define the fluidic network. Following laser ablation, three or four layered devices were created by sandwiching the uniformly toner-coated layer(s) between L1 and L3 layers, visually aligned and inserted into a heated roll laminator with a temperature setting at 130 °C and a speed setting of 2.5 mm/second (Model 305, Mega Dry film laminator).

It is during this lamination step that the toner coating on L2 bonds the neighbouring polyester layers. The patterned toner patches on L1 and L3 constitute a section the ceiling and floor of the valve region, and since these are air-filled and separated by the thickness of the middle spacing layer(s) (L2), their hydrophobic character is preserved enough to serve as a hydrophobic valve. It is noteworthy that the integration of toner valves on the PeT microdevices adds negligible extra cost (~ \$ 0.007 for 100 valves), additional fabrication time (~1 min).

2.3.6 Determine the contact angle on the sidewall

Three and four-layer PeT microdevices with no toner-based hydrophobic valves

were fabricated which has a 60 mm long channel. The actual width of the channel after lamination was experimentally measured under microscope. The microdevice was inserted into the DI water vertically with one end of the channel immersed under the water surface. The water wicked into the channel by capillary force until it was balanced by the gravity. Therefore, one can obtain the relationship between the surface property and observed height difference (H_1) between the water column in the channel and water level around the microdevice. The pressure generated by gravity is ρgH_1 . $\cos \theta_w$ could be solved by plugging the calculated value of ρgH_1 to Eq (2-2). The effective contact angles on the side walls of the laser-ablated microchannel were measured for five replicates devices fabricated using ablated a series combination of laser powers and speeds. The number of laser pulses per inch (PPI) was set to 1000 for all the experiments and “vector” mode was used to cut the rectangular channels.

2.3.7 Characterization of burst pressure

In the study of burst pressure, three and four layers of PeT microdevices were fabricated which have a 20 mm long channel with a toner valve 2 mm away from the outlet. Experimental burst pressures of the hydrophobic toner valves were obtained by a microflow method described elsewhere.¹² Briefly, the inlet of the channel was connected to a straight pipette. The initial addition of deionized water wetted through the channel until it came to the hydrophobic zone. Deionized water was gradually added into the pipette until the water height (H_2) reached a critical value driving the liquid past the hydrophobic zone. The pressure generated by the water column is ρgH_2 , which can be used with Eq (2-2).

2.3.8 Determining the burst frequency of the valve on a centrifugal system

PeT microdevices with toner valves were placed on a spinning setup comprised of a computer-controlled motor (5:1 Micro Metal Gearmotor HP) to precisely modulate rotational frequencies via voltage input (0-6 V). Distilled water was loaded through the inlet which automatically priming the channel until the water was stopped by the toner valve. The critical burst frequency was obtained by gradually increasing the rotational speed at intervals of ~30 rpm until water was observed in the receiving chamber.

2.4 Results and Discussion

2.4.1 Selection of printer toners

The compositions of commercially-available toners differ significantly from brand to brand. For example, according to the MSDS, the black toner in an HP printer is composed of iron oxide (45-55% wt/wt) and a styrene/acrylate copolymer (a ratio of 1:4.6, 45-55% wt/wt.⁷ In contrast, the black toner in a Brother printer, as recorded in MSDS, generally have a higher weight percentage of styrene-acrylate copolymer (85-87 % wt/wt) mixed with fatty acid ester (4-6 % wt/wt), pigment (4-6 % wt/wt), PMMA (1-3 % wt/wt) and silicon dioxide (1-3 % wt/wt). The hydrophobicity of both brands of printer toner patterned on polyester at maximum density was tested by measuring the contact angle of deionized water.

Table 2-1: Contact angles for deionized water on the different surfaces. The standard deviation of all measurements is $\pm 3^\circ$ (n=3).

Material	Transparency	Black (HP) film	Black (Brother)	Magenta (Brother)	Cyan (Brother)	Yellow (Brother)
Contact angle		51 °	111 °	96 °	99 °	91 °

As summarized in Table 2-1, all of the toners increase the contact angle effectively in comparison with untreated transparency film, with the largest increase in contact angle provided by the HP toner. As indicated by Eq (2-2), a relatively large contact angle from the toner provides a wider range for manipulation of surface hydrophobicity via gray-scale level graphic control. As a result, the HP black toner was selected for all the work that follows.

Table 2-2: Contact angle of different biological relevant reagents on the HP toner coating. The standard deviation of all measurements is $\pm 3^\circ$ (n=3).

Reagent	Distilled Water	TE Buffer	PCR Buffer	6M GuHCl (pH=7.4)	1% BSA in PBS (pH=7.4)	HCl (pH=1)	NaOH (pH=13)
Contact Angle	111 °	106 °	114 °	106 °	106 °	110 °	109 °

With HP toner patterned at 100% gray-scale level, the contact angle associated with a number of different reagents commonly used in biochemistry protocols of interest to author's lab were measured and displayed in Table 2-2. While the HP toner proved to be a reliable and relatively inert hydrophobic coating for most aqueous solutions, its stability in the presence of organic solvents or surfactants was poor (data not shown), consistent with many other reported hydrophobic valves.

Printer toner has been previously shown to be inert to variety of chemicals.⁷ Successful DNA extraction, PCR amplification¹⁶, protein concentration and purification³ have been demonstrated on PeT microdevices and suggest that there is a small, if any, effect of these on performance. In addition, considering the contact surface area (<1.6 mm²) and exposure time to reagents are small, chance that adverse interactions (e.g., absorption) occur is minimized. Furthermore, if there is concern over potential redox effect from contact between encapsulated iron oxide and samples/reagents in certain applications, purely polymeric-based toners (e.g., Brother toner) can be used as an alternative. Admittedly, contamination of the samples by direct contact with the toner surface is always a potential issue but the author's experience, thus far, has been that this is not problematic with this valving process.

2.4.2 Characterization of the toner-coated surface on Pe film

The first step is to validate that the use of gray-scale level control of printing could

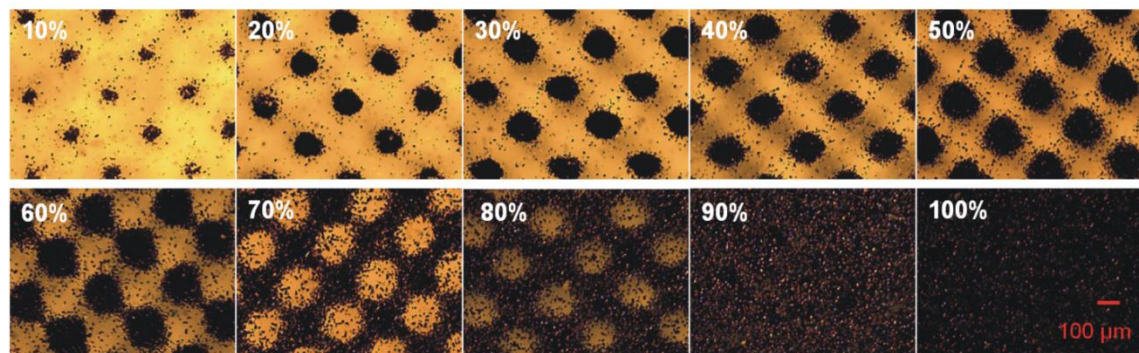


Figure 2-4: Photographs of the printed hydrophobic toner patches with different gray-levels.

provide a graded change in the fractional area of the toner-modified surface, which consequently changes the hydrophobicity. This was accomplished by capturing images of the toner surfaces under a light microscope (Figure 2-4) and using image analysis software to quantitate the fractional area covered by toner for correlation with the gray-scale level setting (Figure 2-5).

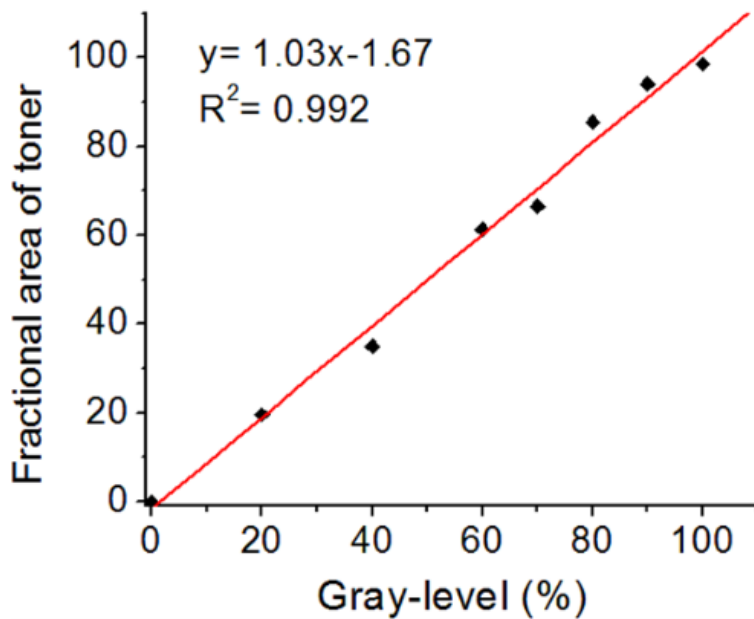


Figure 2-5: Correlation of the fractional area of toner relative to the value of gray-scale level.

As shown in Figure 2-5, there is a defined relationship between the fractional area of toner surface and the gray-scale level value. When the value of the gray-scale level increased from 50% to 70%, the micropattern of the toner surface changed from separated clusters to a honeycomb-like network. The contact angle of DI water on toner surfaces printed at different gray-scale levels were also measured and these results (Figure 2-6) show that the cosine value of the experimentally-determined contact angle decreased

linearly as the fractional area of toner surface increased, in agreement with Eq (2-2). Interestingly, only when the value of gray-scale level was >60% did the toner-modified surface possess adequate hydrophobicity (contact angle >90 °), and this correlated with the

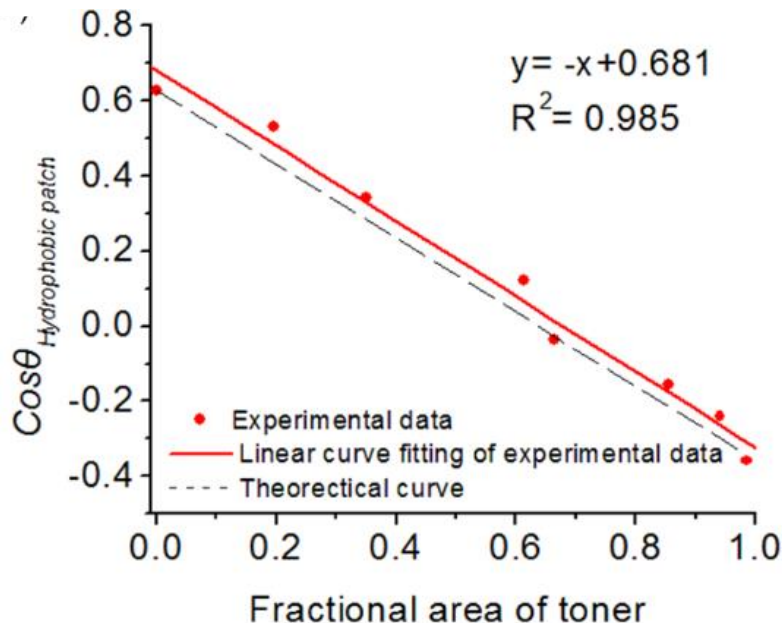


Figure 2-6: Correlation of the fractional area of toner relative to the value of gray-scale level.

appearance of the honeycomb network microfeature. Inter-day reproducibility of the contact angle was $\pm 3^\circ$ (n=3). This confirmed that control of the gray-scale level could provide a graded microscale change the surface, and that a gray-scale level value >60 % should be used to effectively create a hydrophobic surface that could provide valuing functionality.

2.4.3 Characterization of the laser-ablated sidewall on PeT microdevice

Along with the top and bottom surfaces of the toner valves, the quality of the

sidewall (Figure 2-7) is equally important because it also contributes to the reliability and

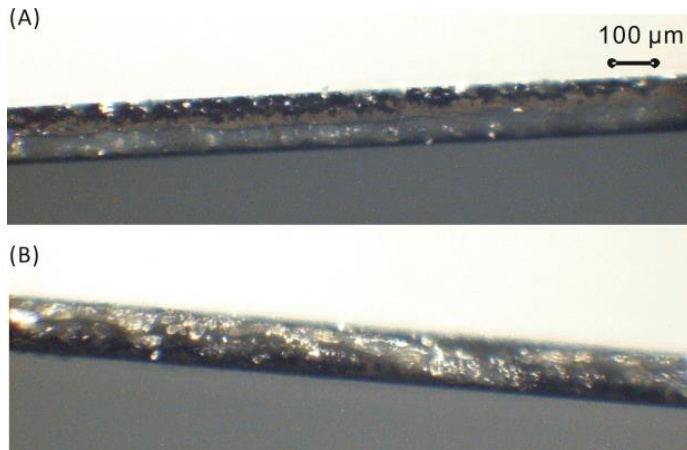


Figure 2-7: Images of the sidewall surface laser ablated with settings of: (A) 0.2% power and 0.7% speed and (B) 0.4% power and 0.4% speed.

robustness of the burst valves. An indirect but simple method was used to calculate the effective contact angle of DI water on the sidewall, as an assessment of the inter-day reproducibility of the heterogeneous surface (the basis for using this method was explained in the Theory section.)

The effectiveness of the laser ablation of the PeT is dependent on the laser power, the pulse frequency and the laser translation speed, all of which contribute to the change in the effective contact angle of the sidewall (Table 2-3). In addition, because of the zone affected by a single laser pulse on transparency film is between ~400 μm in diameter, as the laser ‘vects’ an edge of the square channel, it affects the mechanical and physical properties of the PeT that will comprise the adjacent wall (within ~200 μm). Thus, the laser ablation of a square channel narrower than 200 μm may lead to somewhat different PeT properties than that of a square channel with a width greater than 300 μm. As a result, the contact angle for a 200 μm wide channel was $103^\circ \pm 2^\circ$, while those channel widths

>300 μm was $126^\circ \pm 4^\circ$ for channels wider than on three-layer PeT microdevices. For one set of fabrication parameters for a channel with defined microfeatures (i.e., width and depth) the inter-day reproducibility of the contact angle is comparable to other hydrophobic valves.^{11, 12} The effective contact angle of the sidewall in a three- and four-layered PeT microdevices fabricated was found to be $126^\circ \pm 4^\circ$ and $98^\circ \pm 3^\circ$, respectively, for a channel width greater than 300 μm ($n=3$). Since these two multilayer devices have respective channel depths of 132 μm or 264 μm , certainly in the range of most common microfluidic devices, the PeT microdevices with more than four layers were not investigated in this study.

Table 2-3: Contact angle of DI water on the side wall that was laser ablated with different setting of parameters ($n=5$).

Power	Speed	Power to Speed ratio	Effective contact angle of deionized water
0.2%	0.7%	1:3.5	119 ± 2
0.4%	1.4%	1:3.5	120 ± 3
0.8%	2.4%	1:3.5	122 ± 2
1.6%	5.4%	1:3.5	121 ± 2
0.4%	1.2%	1:3	121 ± 2
0.4%	0.8%	1:2	123 ± 2
0.4%	0.4%	1:1	126 ± 3

2.4.4 Influence of the channel geometry on burst pressure

Previous studies anchored on Eq (2-2), have shown that with a given surface property, the burst pressure is dependent on the valve dimensions (width and depth) and has been observed and validated on microchips using many different substrates including PMMA¹⁴, PDMS¹⁰ and CHF₃ modified glass¹². Here, the influence of the channel geometry on burst pressure was investigated by varying the width of channels that had a depth of 132 μm with toner patterned on the surface printed at 100% gray-scale level. The channel widths investigated ranged from 250-800 μm ; widths narrower than this suffered from occlusion, while larger ones were prone to deformation during thermal lamination. The observed and theoretical burst pressures (from Eq (2-2)) were plotted against the channel width in Figure 2-8. Limited by the resolution of the laser ablation system (~100 μm) and thermal lamination constraints, the burst pressure change controlled by a simple change in channel width was determined to be 492 (± 18) Pa at 800 μm and 573 (± 16) Pa

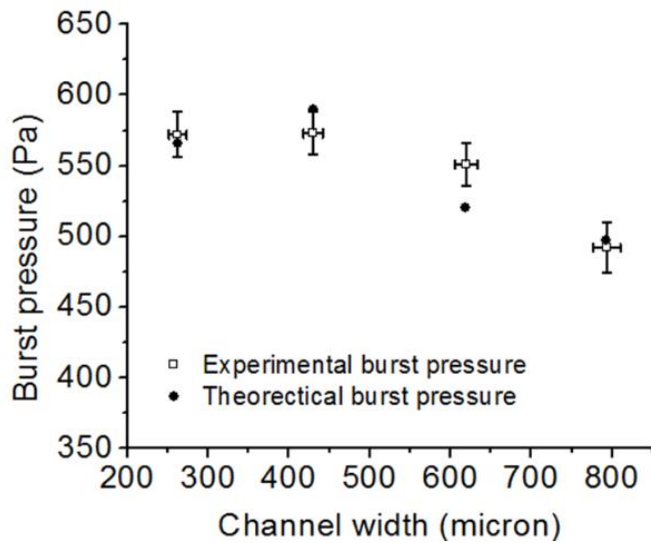


Figure 2-8: Experimental and theoretical results for valve burst pressure versus the fractional area of HP toner with deionized water (n=5). The error bars represent one standard deviation (n=5).

at 400 μm . There is a break in the trend below 400 μm , and this observation is likely explained by the fact that the contact angle along the sidewall of a 250 μm wide channel is smaller than the contact angle of channels wider than 300 μm , a direct consequence of potentially modifying adjacent PeT during the ablation process (discussed in the previous section). This deviation in trend could arise from: (1) the use of a static contact angle instead of the advancing contact angle, (2) the differences in contact angle on a freshly printed toner surface versus toner surface in a channel, where heating during lamination may alter the surface since the temperature is close to the glass transition temperature, and (3) the use of a mean value for the contact angles (e.g., θ_w).

2.4.5 Influence of gray-scale level on burst pressure

The effectiveness of varying the gray-scale level to change the surface hydrophobicity and, thus, control the valve burst pressure was studied by printing microareas of transparency film with toner at different gray-scale levels (>60 %) with constant channel geometry [400 μm (w) \times 132 μm (d)]. Plots of the experimental and calculated burst pressures [Eq (2-2)] versus the gray-scale level are given in Figure 2-9. There is only a small discrepancy between the two data sets, indicating the successful application of the Cassie model to the toner microarea patterning via laser printing lithography. More significantly, the operational band width of burst pressures, from $158 \pm 18 \text{ Pa}$ to $573 \pm 16 \text{ Pa}$, covers a 415 Pa range, a 5-fold improvement over the bandwidth obtainable with geometrical valves (80 Pa). Subsequently, this presents the possibility of tailoring laser-

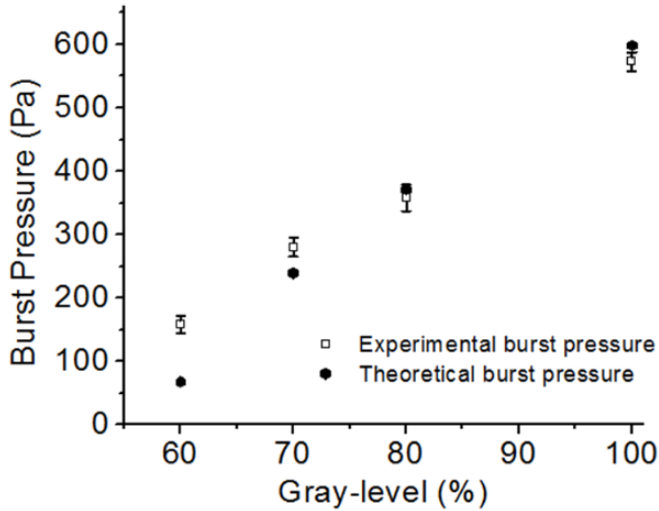


Figure 2-9: Experimental and theoretical results for valve burst pressure versus: the width of the channel with deionized water. The error bars represent one standard deviation ($n=5$).

printed toner valves with burst pressures that meet the specification of the pressure sources used for fluid mobilization. One can envision sources that range from the precision of an automated syringe-type pump to a manual ‘finger-driven’ pump, or centrifugally-driven force from a battery-powered motor (e.g., a motor from a CD drive).

2.4.6 Toner-valve performance in a centrifugal microfluidic device

For further validation of toner valve performance, PeT microdevices with 100% gray-scale toner valves and different channel dimensions were integrated into a rotating microfluidic system. The calculated and experimental burst frequencies, in rpm, with different valve dimensions on the centrifugal system are given in Table 2-4.

The experimental results are in reasonable agreement with theoretical predictions given by Eq (2-5). The difference between the experimental and calculated values, however, can be partially explained by that the pressure calculated by Eq(5) is an

equivalent pressure head and can deviate from the actual pressure experience at the toner valve on the centrifugal system and/or a limitation in accurately setting the rotation speed (limitation of the motor and control). Nevertheless, these results validate the functionality of toner valves for centrifugal-microfluidic applications.

Table 2-4: Burst frequency of the toner valves printed at 100% gray-scale level with different dimensional parameters. (n=7)

No.	Channel width (μm)	Channel depth (μm)	R1 (mm)	R2 (mm)	Calculated burst frequency (rpm)	Observed burst frequency (rpm)
1	400	132	20	40	405	353 ± 29
2	400	264	20	40	287	303 ± 22
3	600	132	20	30	628	575 ± 30
4	800	132	20	40	531	480 ± 19

2.4.7 Multivalve operation in a centrifugally-driven microfluidic system

Versatile movement and metering of fluids (i.e., sample, buffer reagents) on a centrifugal microfluidic system is essential for biological assays that involve the stepwise addition of reagents.^{13, 20, 21, 22} For valves with a given geometry, the burst frequency (in RPMs) decreases as the distance from the center of the microchip increases. Therefore, valves with identical geometry positioned in a line radially from the center to the perimeter will, at a particular rotational frequency, have the outer valves burst first. Since centrifugal force drives fluid from the center to the perimeter of the microchip, a valving system that allows for the metering, flow and mixing of reagents loaded at center reservoirs

necessitates that valves burst in the proper sequence at increasing rotational speeds. Knowing that, at a particular rotational speed, the innermost valves must burst first, the channel geometry must decrease from the center outwards. As indicated earlier, geometrical capillary valves provide a relatively narrow operational bandwidth of burst pressures, which will not only limit the number of possible sequential assay steps, but also

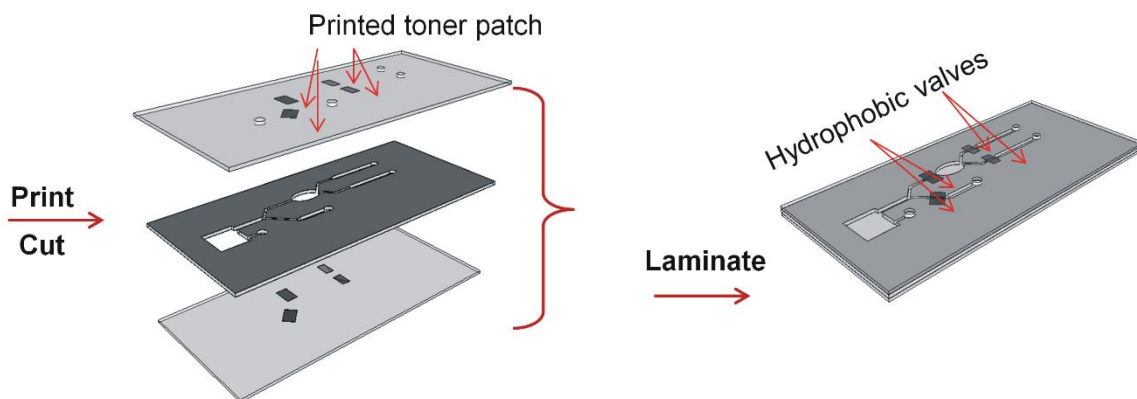


Figure 2-10: Schematic illustration of the fabrication of PeT microchip with multiple toner valves.

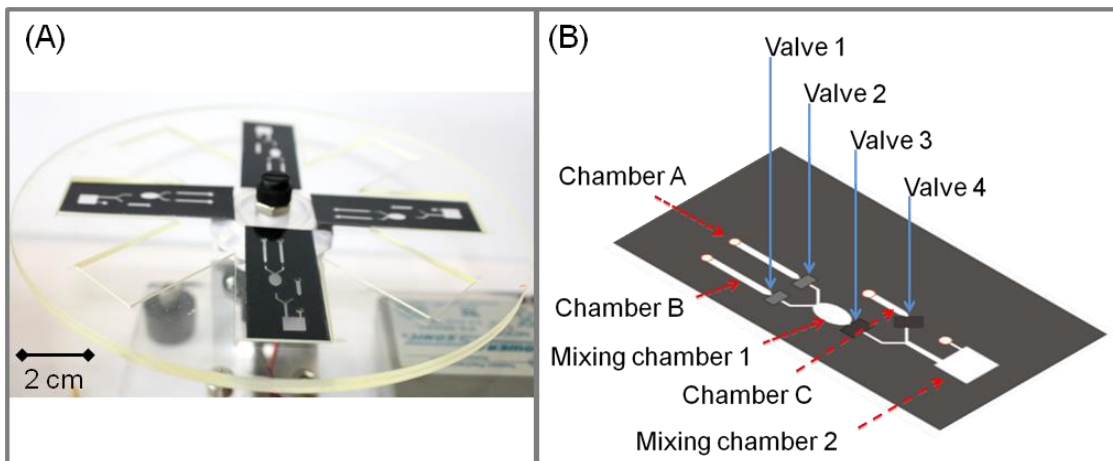


Figure 2-11: Appling the PeT microchip to centrifugal system. (A) Photograph showing PeT microchips containing toner valves on the home-built centrifugal system. (B) Fluidic architecture for sequential valving in the fluidic network.

will increase the risk of valving failure modes. To circumvent this issue, geometry was kept constant and toner valves printed at gray-scale levels of 65% (valve 1), 70% (valve 2) or 100% (valve 3&4) were employed in this microchip (Fig.2-10).

As shown in Figure 2-11, the microchannel architecture is detailed for three reagents (food dyes) with the toner valves represented by shaded rectangles. Figure 2-12 provides a series of images obtained after stepping through four rotational speeds: 480, 520, 690 and 800 rpm. This demonstrates the power of toner valves in geometrically-identical microchannels to have varied burst frequencies based on hydrophobicity.

The direct toner printed valve introduces a new development in fabrication for centrifugally-driven (and other) microfluidic platforms. Programming of sequential reagent delivery on one microdevice can be easily reconfigured by simply alternating the gray-scale level setting for the top and bottom layers while using the same modular design for the middle layer(s), thus relieving the dependency on sophisticated designs of

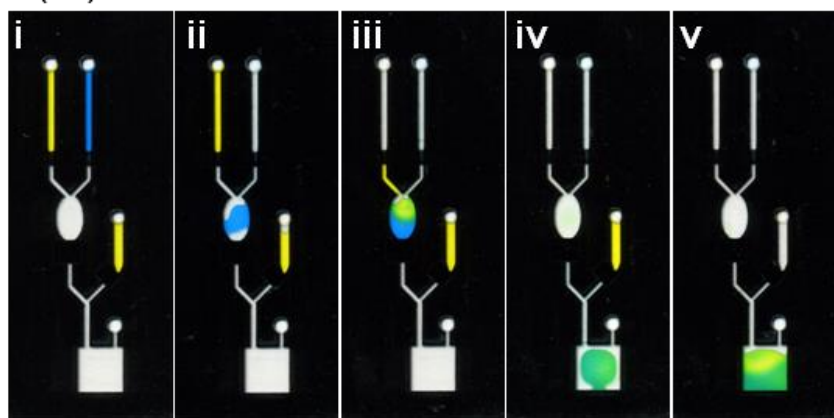


Figure 2-12: Demonstrating toner-based hydrophobic valving on centrifugal microchips. A series of images captured by an office scanner illustrating valving where the steps are: (i) reagent loading, (ii) addition of reagent A (blue dye), (iii) addition of reagent B (yellow dye) to reagent A, (iv) transfer of mixture A&B to downstream chamber, and (v) addition of reagent C (yellow dye).

for micro-fluidic network, as well as demands on the fabrication method(s). Since this reconfigurable feature provides a possible solution for rapid and cost-effective customization of microfluidic devices, it may open the door to more widespread use of PeT as a substrate for advancing LOC technology.

2.5 Conclusions

This chapter outlines the working principles and fabrication approach to integrate hydrophobic toner valves on PeT microdevices via laser printer lithography. Having characterized the relationship between hydrophobicity of a patterned toner surface in the microchannel and the burst pressure, gray-scale level control to vary the hydrophobicity was leveraged so that valves require different burst frequencies. The resolution of gray-scale level control in the current (and even older) laser printers is adequate for hydrophobic modification on PeT surface. By printing designs onto transparency film with toners of different compositions or gray-scale levels, the workable pressure range of burst valves was expanded, and these can be easily integrated to more complex systems to enable sequential delivery of multiple reagents either on pump- or centrifugally-driven microfluidic platforms.

As compared to other commonly used capillary valves, the incorporation of toner-based hydrophobic valves brings convenience to microchip fabrication with several advantages: (1) only one extra printing step is required, (2) highly-precise microstructures for burst pressure control can be eliminated, (3) there is zero additional fabrication time as the number of valves increases, and (4) there is potential for reprogramming an integrated microfluidic network via reconfiguration of the print setting for each valve. In addition,

this laboratory fabrication protocol may present new potential for industry-scale production used the currently-existing range of roll-based integration technologies for printing and lamination. Details on the manufacturing engineering details for such a device, as well as the putative cost to mass manufacturing are beyond the scope of this chapter.

2.6 Reference

1. A.-L. Liu, F. He, K. Wang, T. Zhou, Y. Lu, and X. Xia, *Lab on a chip*, 2005, **5**, 974–8.
2. A.-L. Liu, T. Zhou, F.-Y. He, J.-J. Xu, Y. Lu, H.-Y. Chen, and X.-H. Xia, *Lab on a chip*, 2006, **6**, 811–8.
3. H. Yu, Y. Lu, Y. Zhou, F. Wang, F. He, and X. Xia, *Lab on a chip*, 2008, **8**, 1496–501.
4. D. J. Beebe, J. S. Moore, J. M. Bauer, Q. Yu, R. H. Liu, C. Devadoss, and B. Jo, *Nature*, 2000, **404**, 588–590.
5. K. Abi-Samra, R. Hanson, M. Madou, and R. a Gorkin, *Lab on a chip*, 2011, **11**, 723–6.
6. R. Gorkin, C. E. Nwankire, J. Gaughran, X. Zhang, G. G. Donohoe, M. Rook, R. O’Kennedy, and J. Ducrée, *Lab on a chip*, 2012, **12**, 2894–902.

7. C. L. do Lago, H. D. T. da Silva, C. A. Neves, J. G. A. Brito-Neto, and J. A. F. da Silva, *Analytical chemistry*, 2003, **75**, 3853–8.
8. R. L. Hoffman, *Jounal of Colloid and interface Science*, 1975, **50**, 228–241.
9. L. Gao and T. J. McCarthy, *Langmuir : the ACS journal of surfaces and colloids*, 2006, **22**, 6234–7.
10. H. Cho, H.-Y. Kim, J. Y. Kang, and T. S. Kim, *Journal of colloid and interface science*, 2007, **306**, 379–85.
11. H. Andersson, W. Van Der Wijngaart, P. Griss, F. Niklaus, and G. Stemme, *Sensors & Actuators B*, 2001, **75**, 136–141.
12. Y. Feng, Z. Zhou, X. Ye, and J. Xiong, *Sensors and Actuators A: Physical*, 2003, **108**, 138–143.
13. J. Ducr  , S. Haeberle, S. Lutz, S. Pausch, F. Von Stetten, and R. Zengerle, *Journal of Micromechanics and Microengineering*, 2007, **17**, S103–S115.
14. C. Lu, Y. Xie, Y. Yang, M. M.-C. Cheng, C.-G. Koh, Y. Bai, L. J. Lee, and Y.-J. Juang, *Analytical chemistry*, 2007, **79**, 994–1001.
15. M. J. Madou, L. J. Lee, S. Daunert, S. Lai, and C. Shih, 2001, 245–254.
16. G. R. M. Duarte, C. W. Price, B. H. Augustine, E. Carrilho, and J. P. Landers, *Analytical chemistry*, 2011, 5182–5189.

17. C. J. Easley, J. M. Karlinsey, J. M. Bienvenue, L. A. Legendre, M. G. Roper, S. H. Feldman, M. A. Hughes, E. L. Hewlett, T. J. Merkel, J. P. Ferrance, and J. P. Landers, *Proceedings of the National Academy of Sciences of the United States of America*, 2006, **103**, 19272–7.
18. N. J. Cira, J. Y. Ho, M. E. Dueck, and D. B. Weibel, *Lab on a chip*, 2012, **12**, 1052–9.
19. J. a Lounsbury, B. L. Poe, M. Do, and J. P. Landers, *Journal of Micromechanics and Microengineering*, 2012, **22**, 085006.
20. M. Madou, J. Zoval, G. Jia, H. Kido, J. Kim, and N. Kim, *Annual review of biomedical engineering*, 2006, **8**, 601–28.
21. R. Gorkin, J. Park, J. Siegrist, M. Amasia, B. S. Lee, J.-M. Park, J. Kim, H. Kim, M. Madou, and Y.-K. Cho, *Lab on a chip*, 2010, 1758–1773.
22. N. Godino, R. Gorkin III, A. V Linares, R. Burger, and J. Ducr  , *Lab on a chip*, 2013, **13**, 685–694.
23. M. Focke, F. Stumpf, B. Faltin, P. Reith, D. Bamarni, S. Wadle, C. M  ller, H. Reinecke, J. Schrenzel, P. Francois, D. Mark, G. Roth, R. Zengerle, and F. von Stetten, *Lab on a chip*, 2010, **10**, 2519–26.
24. J. Park, V. Sunkara, T.-H. Kim, H. Hwang, and Y.-K. Cho, *Analytical chemistry*, 2012, **84**, 2133–40.

25. S. Haeberle, T. Brenner, R. Zengerle, and J. Ducr  , *Lab on a chip*, 2006, **6**, 776–81.
26. J. Steigert, T. Brenner, M. Grumann, L. Rieger, S. Lutz, R. Zengerle, and J. Ducr  , *Biomedical microdevices*, 2007, **9**, 675–9.

Chapter 3: Multilevel Fluidic Flow Control for Rapid Protein Quantitation in a Rotationally-driven Polyester-Toner Microdevice

3.1 Introduction

As mentioned in Chapter one, several clinically-relevant assays on paper-based microfluidic devices have been realized and commercialized, such as glucose, protein, cholesterolsterol and lactate detection/quantitation^{1,2,3}. The popularity of paperfluidic devices can be attributed to several obvious advantages including: 1) the low material cost, 2) the ease of fabrication by wax printing, and 3) the self-pumping of fluids via capillary action through hydrophilic cellulose fiber or like materials. Compared to the paper-based microfluidic device, polyester toner-based (PeT) microfluidic devices share several attractive characteristics with paper-based microfluidic devices: (1) poly(ethylene terephthalate) (Pe) film compose overhead transparencies, thus, inexpensive and readily-available; (2) multilayer devices can be fabricated with simple lamination⁴; (3) overhead transparencies have a silica coating enabling automatic reagent-priming; and (4) a thickness/density similar to that of paper. Moreover, they offer some unique advantages not inherent in paper devices, including a closed, non-porous channel that eliminates sample evaporation and loss of analytes due to a chromatographic effect. Additionally, sample delivery is more efficient on toner-based devices because there is no loss of reagents to saturating the substrate (typical loss with paper-based device is 50% or greater) prior to mobilizing it to the detection zone⁵. In addition, there are also flow impedance

issues in paper, where a wetted channel containing residue from the first reagent may have a flow rate that is significantly altered for the second reagent. Finally, the homogenous mixing on a PeT microchip should be substantially simpler than that on paper where inhomogenous spotting of the indicator and the ‘chromatographic effect’ can adversely affect mixing. To minimize those effects, paper-based microfluidic device require a longer reaction time for detection.

PeT microdevices for real-world applications have been restricted to one-step chemistries (e.g., single reagent delivery), at least in part, due to the difficulty incorporating active or passive valving features for the flow control needed for basic functions (e.g., metering and mixing). In chapter 2, hydrophobic valves were incorporated into PeT microdevices by simple laser-print patterning of toner that created surfaces of varied hydrophobicity governed by a gray-scale setting. The beauty of this approach was that the same method used to define the fluidic architecture^{4,6}, was also used to define the valving components. With these allowing for the sequential delivery of multiple reagents, an avenue was presented to the reagent metering needed for executing multi-step protocols in quantitative assays. The lacking functionality needed for PeT microdevice to conduct multi-step chemistry reaction is mixing. To author’s best knowledge, so far only one passive mixer has been demonstrated on the PeT microdevice. The passive mixer was created by printing the 7 μm -high periodic bas-relief printer toner patterns on the floor of the channel, which act as obstacles in the flow path for advection mixing. However, limited by the height of the toner pattern, this mixing scheme is only applicable to the channel has a very low aspect depth/width ratio⁷. As a result, this mixing scheme does not apply to

the channel depth larger than 100 μm scale that is required by most of applications demonstrated on PeT devices.

This chapter presents, for the first time, a CD-sized 5-layer PeT microfluidic device operated on an inexpensive and portable battery-powered centrifugal system, where several basic fluidic control functionalities required in multistep protocols (i.e., valving, metering, and mixing) have been achieved. Utilizing the passive valving technology that is reported in chapter 2, metering through two interconnected microfluidic networks (one where parallel metering of reagents ranges from nanoliter to microliter) was demonstrated. Critical to the effectiveness of this chip was the passive, rotation-activated reciprocating mixer that exploited a ‘surface-tension pump’; this chapter will discuss the fundamental principles behind this mixer and provide a preliminary characterization of the mixing process. Finally, the ability of the PeT microchip to execute a multiplexed colorimetric assay for quantitation of total protein in human blood plasma samples was carried out to test its serial dilution performance. The highlight of the five-layer PeT microchip is the ability to integrate a substantial number of fluidic control elements with rapid prototyping (~60 min) while maintaining a low-cost per device (<\$2), with only an office laser printer, a laser cutter and laminator required as equipment.

3.2 The Working Principle

3.2.1 Volume Splitting

The basic premise for aliquoting different volumes from a sample is based on a design that exploits two types of ‘hydrophobic’ valves created from toner on polyester surfaces⁸. Both toner valves were defined by selectively patterning a toner-based hydrophobic barrier on the top and bottom surface of the channel but, as defined in Chapter 2, the degree of hydrophobicity (which controls break-through pressure) is determined by gray-scale level. The first type printed at a 70% gray-scale and located at the channels leading to the waste chambers, while the second type is printed in 100% gray-scale and placed downstream of the aliquot chambers (Figure 3-1A). As a result of the cumulative effect of a lower toner density (thus, less hydrophobic) and an increased distance from the

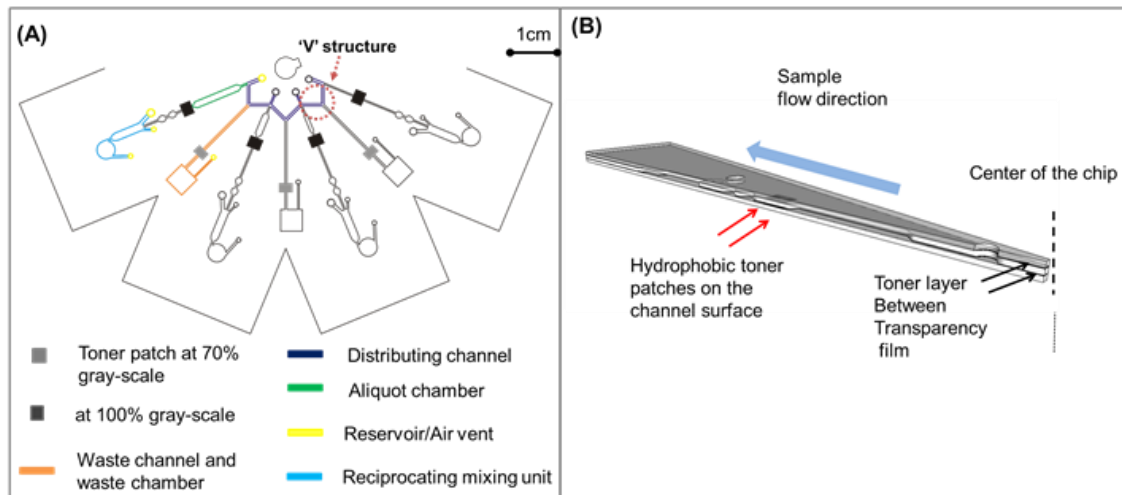


Figure 3-1: Design of a three layer aliquoting PeT microchip. (A) Schematic of the microfluidic network of one single sample aliquot domain on a CD-like dilution microchip for centrifugal system. The design of the buffer aliquot part is similar but with different size of aliquot chambers. (B) Section plane view of one metering branch.

center of rotation, the 70% gray-scale barrier has a rotational frequency for break-through

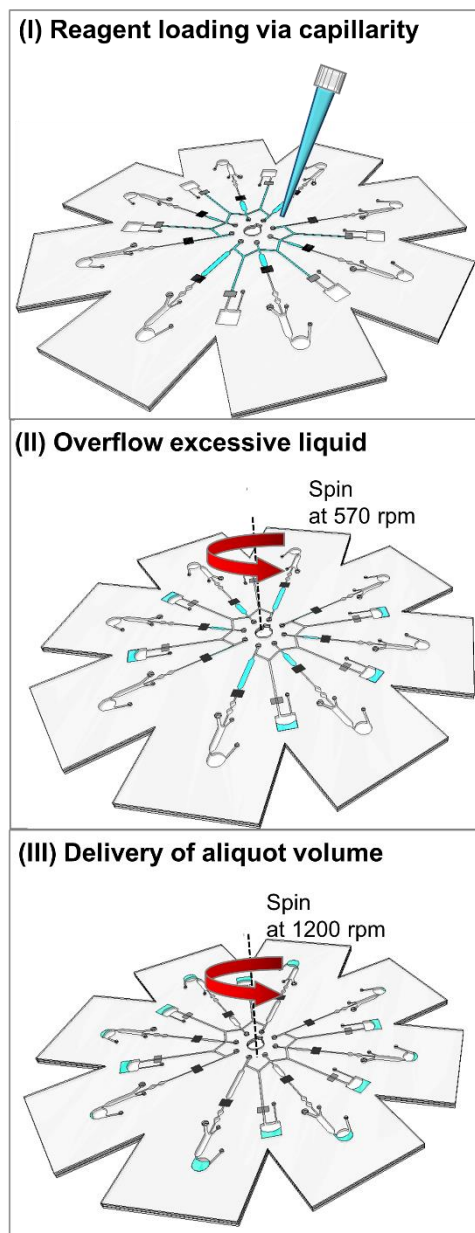


Figure 3-2: Schematic Sketch of the filling process of the aliquoting for sample on a three layer aliquoting PeT microchip.

that is much lower than the 100% gray level hydrophobic barrier which is directly connected to the metering chambers.

Aliquoting is achieved with the two-step process that is illustrated in Figure 3-2. Initially, a sample/reagent of undefined volume (12-14 μL) is loaded into any one of the reservoirs at the center of the microchip. Due to the hydrophilic nature of the silica-doped transparency film, capillarity drives the sample/reagent into the distribution channel; this automatically primes a series of branched aliquoting chambers and waste channels until the hydrophobic barrier is encountered. As a result, the sample volume loaded into the system is reliably and accurately defined. When the microdevice is spinning at 570 rpm, the solution breaks through the 70% gray-scale hydrophobic valves connected to the waste chambers, thus allowing the excess liquid to overflow into the waste chamber. As the result, the liquid remained in the aliquot chamber is separated by a plug of air in the distribution

channel. The microchip is then rotated at 1200 rpm, generating enough centrifugal force to breach the 100% gray-scale hydrophobic valves and enter the downstream mixing domain. By varying the width and length of aliquot chambers, the microfluidic aliquoting network, shown in the Figure 3-1, provides four accurate aliquots that range roughly from 250 nL to 2.25 µL.

3.2.2 Multi-level aliquoting on 3D PeT microdevice for sample diluting

The metering functionality on the PeT microchip shown in the Figure 3-1 for a single reagent can be further expanded to provide ‘dilution’ functionality. Figure 3-3 shows a five-layer PeT microdevice that has two microfluidic ‘levels’ for metering, one for *sample* and one for *buffer* (for dilution), with L1 providing ports for sample/reagent input to the device, and L3 containing ‘vias’ (through-holes) for fluidically-connecting the two levels. The microfluidic architecture for both levels is defined by laser-ablation of the architecture completely through layers L2 and L4, where the Pe film that has been uniformly coated with printer toner on both sides prior to ablation. The fluidic circuit in the *buffer metering* level is defined by L2 which is sealed by L1 (top) and L3 (bottom) – both L1 and L3 are Pe film onto which toner has been printed on specific microareas to provide a hydrophobic valve through toner on the channel ‘ceiling’ and ‘floor’ (see cut-away in Figure 3-1B). The microfluidic *sample metering* level is defined by L3, L4 and L5, which functions very much like that of L1, L2 and L3. However, the geometry of the aliquot chamber on L4 can be different from that on L2 based on the application of the microdevice. In addition, ‘venting’ holes in the metering architecture in L4 are also cut into L1, L2 and L3 for air exchange during reagent loading.

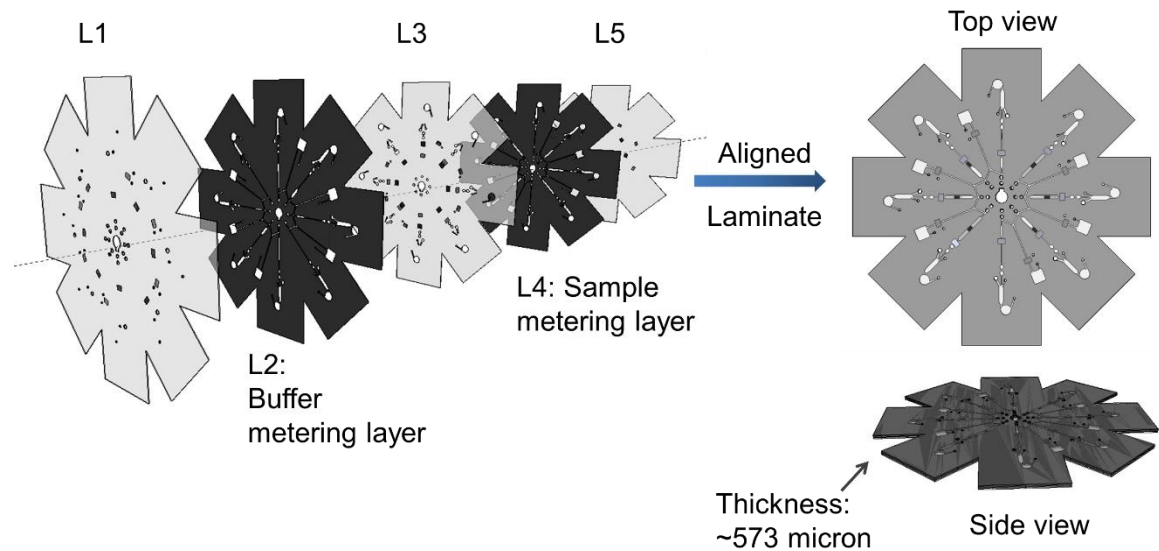


Figure 3-3: Schematic showing assembly of a five-layer CD-like dilution microchip, consisting of transparency film and printer toner.

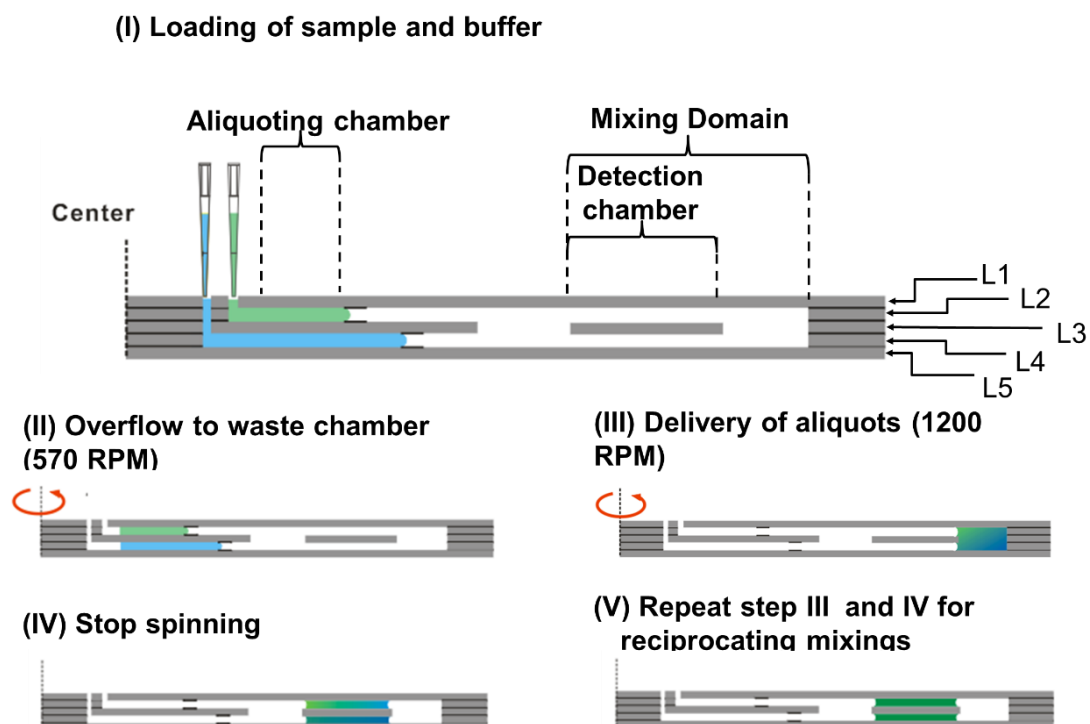


Figure 3-4: A schematic showing operation of five layer PeT microchip for multi-level fluidic handing for sample dilution and mixing processed from side-view.

For each aliquoting level in the five layer PeT microchip, there are two identical aliquot domains. Overlap of the sample and buffer aliquoting domain provides a parallel dilution functionality (Figure 3-4). In each dilution domain, sample or buffer is first processed to form four different aliquot volumes concurrently on each level. Following that, each sample and varied buffer volume aliquot is forwarded to the downstream mixing domain. The size of the aliquot chambers in sample and buffer aliquoting layer is optimized to provide a dilution of sample from 1.25- to 10-fold with a fixed final volume 2.5 μL .

3.2.3 Surface-tension pump to assist reciprocating passive mixing

If rotationally-driven microdevices are to enable portable and cost-effective devices, the integration of mixing functionality should add minimally to the time and cost of fabrication. In addition, invoking the mixing process should add little, if any, burden to the hardware (e.g., mechanical and power input). This is, indeed, the case for PeT microchips, where downstream of each aliquoting chamber, a surface-tension pump

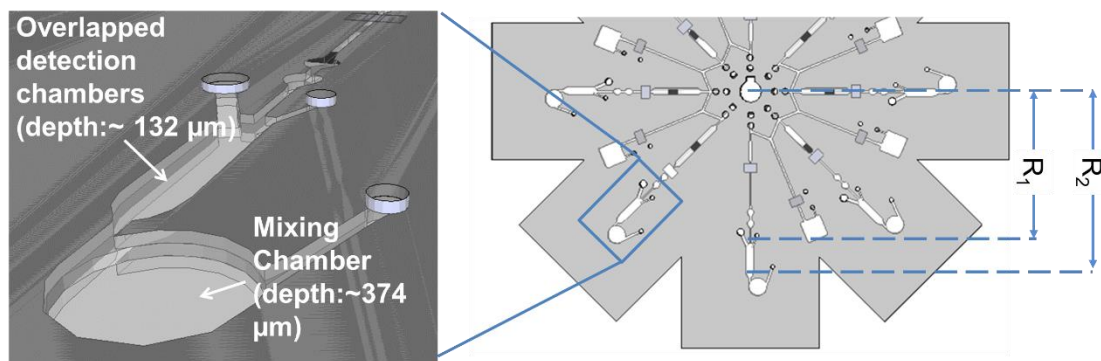


Figure 3-5: The 3D image shows the detailed view on a single reciprocating passive mixer.

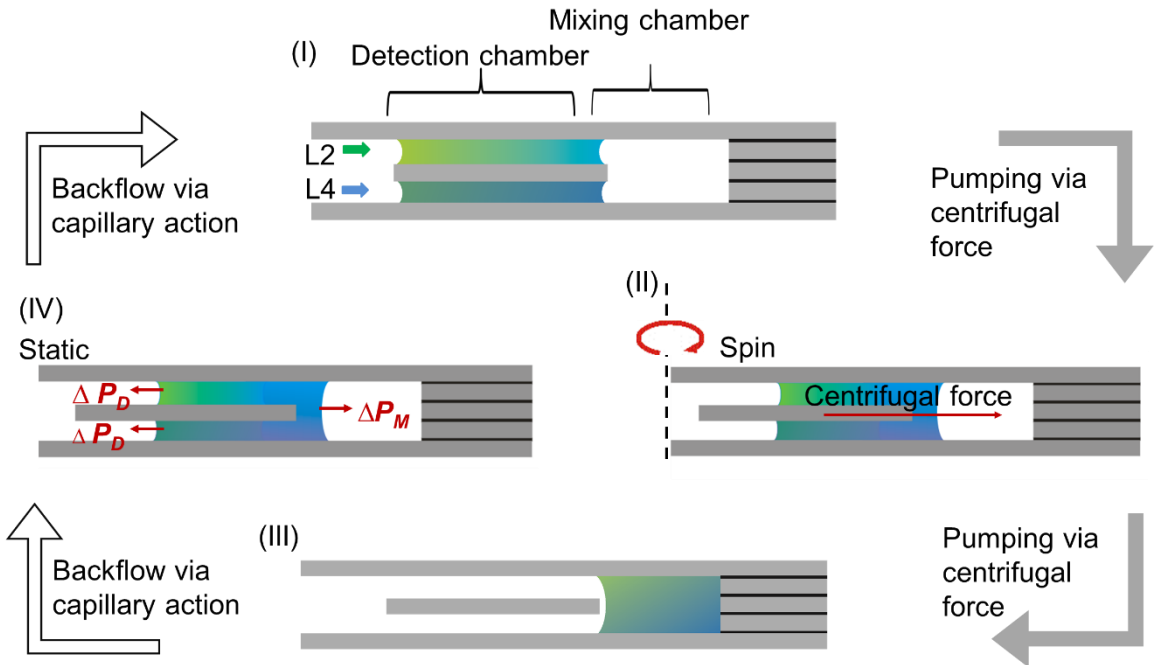


Figure 3-6: Illustration of the reciprocating mixing process showing by the side-view of one reciprocating mixing process.

(Figure 3-5) that drives a reciprocating passive mixer under varied rotation speed was integrated. As the buffer and sample aliquots are pumped over and through the hydrophobic barriers on different aliquoting levels (L2 and L4, respectively), they first pass through a pair of overlapped detection chambers of 132 μm depth (separated by the L3) and then fill a 374 μm deep round mixing chamber furthest from the center of rotation (Figure 3-6). Due to the hydrophilicity of the transparency film surface and geometry of the chambers, the capillary pressure generated by the meniscus in the detection chamber is calculated to be greater than that in the mixing chamber, both of which can be estimated by using Young-Laplace equation:

$$\Delta P = 2\gamma \left(\frac{\cos \theta_w}{w} + \frac{\cos \theta_p}{h} \right) \quad (3-1)$$

where γ is the surface tension of the liquid, h is the height of the channel, w is the channel width, $\cos \theta_w$ is the contact angle of the fluid on the side walls, and $\cos \theta_p$ is the contact angle at the top and bottom of the channel (Pe transparency). As for both the detection and mixing chambers, the width is greater by an order of magnitude compared to the height (1.8 mm width for the detection chambers; 5 mm diameter for the mixing chamber), therefore, Eq (3-1) can be simplified as:

$$\Delta P = 2\gamma \left(\frac{\cos \theta_p}{h} \right) \quad (3-2)$$

Assuming that the change of the contact angle of the mixture over the course of the mixing is negligible, in principle, the pumping pressure for the backflow can be calculated as follows:

$$\Delta P_F = \Delta P_D - \Delta P_M = 2\gamma \cos \theta_p \left(\frac{1}{h_D} - \frac{1}{h_M} \right) \quad (3-3)$$

where ΔP_D and ΔP_M are the capillary pressure from the meniscus at the detection chamber and mixing chamber respectively. h_D and h_M are the depth of the detection chamber and mixing chamber. Since $h_D < h_M$, one can infer from Eq (3-3) that it is more energetically-favorable for the mixture to remain in the detection chamber rather than the mixing chamber when the microchip is stationary.

Only when the rotation frequency exceeds a critical value, is rotationally-driven pumping sufficient to counteract the capillary action, driving the mixture to the mixing chamber. The critical rotation frequency needed to overcome the surface tension pumping can be estimated by:

$$f(\text{Hz}) = \frac{30}{\pi} \sqrt{\frac{2\Delta P_F}{\rho(R_2-R_1)(R_2+R_1)}} = \frac{30}{\pi} \sqrt{\frac{\Delta P_F}{\rho\Delta R\bar{R}}} \quad (3-4)$$

where ρ is the density of the mixture, R_1 and R_2 are the two distances of liquid from the disc center when stored in the detection chamber, and ΔR is equal to $R_2 - R_1$ while \bar{R} is equal to $(R_2 + R_1)/2$. However, once rotation speed decreases below the critical frequency, the capillary force overcomes the centrifugal force, driving the mixture flow back to the detection chambers since $\Delta P_F > 0$. In other words, the configuration of a pair of detection chambers and the mixing chamber comprise a micropump (driven by surface tension) that directs the liquid inward as the RPM decreases. As the microchip undergoes a series of “spin-stop” cycles, this surface tension-driven micropump serves as a reciprocating passive micromixer, allowing the liquid to spilt and recombine as many times as is needed. The concept underlying this mixer is similar to that reviewed by Nguyen et al., for the ‘serial lamination mixer’⁹. One additional aspect of the design that is noteworthy is the circular shape of the mixing chamber, which produces advective fluidic currents to further promote mixing while pumping the mixture to the mixing chamber¹⁰.

3.3 Material and Methods

3.3.1 Reagent

All the reagents were purchased from Sigma-Aldrich if not specified. The blue dye and yellow dye solutions were prepared by dissolving eriglaucing and tartrazine in a 10 mM tris (Fisher Scientific)/1 mM EDTA (TE) buffer at a pH of 7.51 (measured by a Mettler Toledo MP 220 pH meter) to a final concentration of 2.7 mM and 3.7 mM respectively. The green dye solution is a mixture of the blue dye and the yellow dye solution in a ratio of 3:1 (v/v).

The indicator for the colorimetric protein assay was prepared by modifying the recipe in a known procedure¹¹: 3.3 mM tetrabromphenol blue (TBPB) (Alfa Aesar) was first dissolved in the pure ethanol, and then mixed with 250 mM citrate buffer solution (pH=1.8) by 1:1 ratio (v/v). The preparation of the artificial blood plasma buffer was prepared followed a procedure described elsewhere¹². The protein concentration in the artificial blood plasma was adjusted by dissolving different mass of human serum albumin (HSA) in the artificial blood plasma buffer.

3.3.2 Fabrication of the PeT microchip

The protocol for assembly of a five-layer PeT microchip (see Figure 3-3) leveraged the bonding and assembly reported in previous chapter⁸. Most notable in design change is the fact that this is the five layers with two microfluidic levels. Briefly, the first (L1), third (L3), fifth layer (L5) of the Pe transparency film were first selectively patterned by a series of toner patches by a laser printer (HP laserjet 4000) with cyan toner cartridge (HP C-4127X) to defined the hydrophobic barriers, using by a design generated with CorelDraw. For L1 and L5, only the bottom surface and top surface were toner-patterned respectively. The patterned toner arrays on the top and bottom surface of L3 were printed in the mirror image of that on the L1 and L5 respectively. In such manner, the toner patterned on the L1 and top surface of L3 defines the ceiling and floor of the hydrophobic valves for buffer metering while the toner patterned patches on the bottom surface of the L3 and on the L5 define the hydrophobic valves for sample metering.

The L2 and L4 layers were printed with two uniform coating layers of toner on each side. Following the printing, five layers were ablated by a CO₂ laser system to cut access

holes on L1 and L3 to serve as reagent loading reservoirs. Aliquoting microfluidic network for buffer and sample were ablated into the L2 and L4 respectively. In the mixing region, all middle layers (L2-L4) were ablated according to the detailed design shown in Figure 3-5. The laser ablation parameters can be found in the previous chapter. After ablation, five layers were visually aligned with the assistance of alignment holes and inserted into an in-house modified heated roll laminator (UltraLam 250B) with a temperature of 150 °C and estimated speed of 8 mm/ second. During the lamination, the toner coatings on L2 and L4 were melted and bonded to the neighboring layers, while the hydrophobic toner barriers on the L1, L3 and L5 layers were spaced by L2 and L4 layers, thus remained their integrity. The three layer metering microchips, used in the calibration experiment, were fabricated using the same procedure without layers L4 and L5.

3.3.3 Spinner setup

The spinner step used to generate controlled centrifugal force consists of a computer-controlled motor (5:1 MicroMetal Gearmotor HP) which provide a rotational frequency from 200 rpm to 2500 rpm based on the voltage input (0-6V) with an increase interval of ~30 rpm. The motor stops at an input voltage of 2.5 V and spins at full speed in the reverse/ forward direction at 0 V/5 V respectively. The system can be either powered solely by the battery (PS-605W, Power-sonic battery) or be connected to a power adapter which will supply 6V in parallel with the battery, in turn charging the battery while it runs. The voltage control utilizes a LabVIEW application to define the analogue input to the motor via a data acquisition card (6024-E, National Instruments).

3.3.4 Image analysis to quantitate the metered volume

To quantitate the metered volume, the three-layer PeT microchip with the metered yellow dye in the serpentine channels were scanned by a desktop scanner (Epson Perfection V100 Photo Scanner) at 1200 dpi and 24 bit color resolution. The pixels which represent the black toner were first discarded by setting a Hue-based threshold and the rest of the pixels were processed into binary with the gray level threshold set by an isodata algorithm written in Wolfram Mathematica 8.0. The measureable variant is the total number of pixels that represent the yellow dyes.

Same scanner setting was used for the evaluation of mixing performance but with a different isodata algorithm. Artifacts from the black toner was first eliminated by using the same Hue-based algorithm. The rest of pixels representing the dyes were into a gray-level histogram, representing the full area of the mixing chamber and standard deviation was calculated. For the analysis of dilution performance and the colorimetric assay, same algorithm was employed to exclude the artifacts from the black toner and an average hue of the mixing region were calculated based on all the pixels representing the mixtures.

3.4 Result and Discussion

3.4.1 Influence of multiple layer alignment on aliquoting performance

Since the aliquot volume is geometrically defined by the region between the intersection of the aliquot chamber with the distribution channel and the hydrophobic toner barriers at the end of the chamber, minimizing misalignment of the hydrophobic barriers (both ceiling and the floor of the channel) is essential. This has been addressed by

designing an alignment port that is laser cut in each layer for simple assembly using an alignment pin; this assures alignment precision with a tolerance of up to $\sim 500 \mu\text{m}$. In addition, all of the hydrophobic valves connected to the aliquoting chamber have a width of $300 \mu\text{m}$, since this is suggested to be the minimum attainable channel width via laser ablation for constructing a reliable hydrophobic valve on PeT microchip⁸. Therefore, longitudinal misalignment of the toner patches on the top and bottom of the channel by as much as $500 \mu\text{m}$ is possible as a result of the mechanical roller mechanism in the laminator. This creates the possibility of an uncertainty in volume of 26 nL ($w \times l \times d = 300 \mu\text{m} \times 500 \mu\text{m} \times 132 \mu\text{m}$). As a result, the effect on precision/accuracy of the aliquoted volumes will range over roughly an order of magnitude depending on the volume aliquoted. With a $2.25 \mu\text{L}$ chamber, the error is negligible, however, with a 250 nL chamber volume, error from misalignment is expected to $\sim 10\%$, which mirrors that obtained with an piston-driven pipette¹³.

3.4.2 Influence of microfluidic network design on aliquotting process

In addition to layer alignment, reliable and precise aliquotting is decisively impacted by the break-off process (when the air plug displaces the liquid in the distribution channel during the overflow process) cut at the intersection of the distributing channel with the inlet of the aliquot chamber (Figure 3-2). Compared to the earlier prototype design of metering network shown in Figure 3-7, two issues had to be addressed in the final design of the aliquotting network for the PeT microchip (Figure 3-1). The first issue was the undesirable siphoning action (Figure 3-8A). When the excess liquid in the distributing

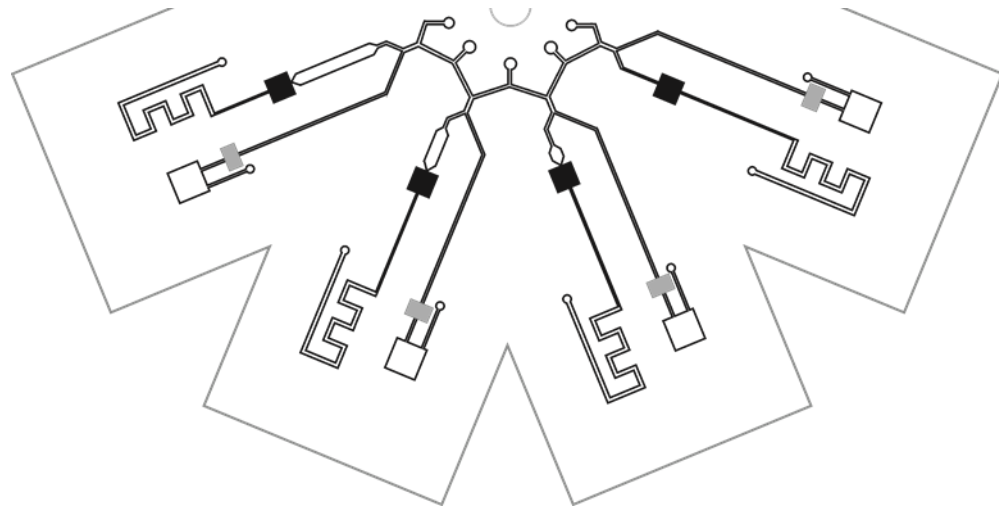


Figure 3-7: Schematic of a previous microfluidic design for parallel metering which does not properly meter.

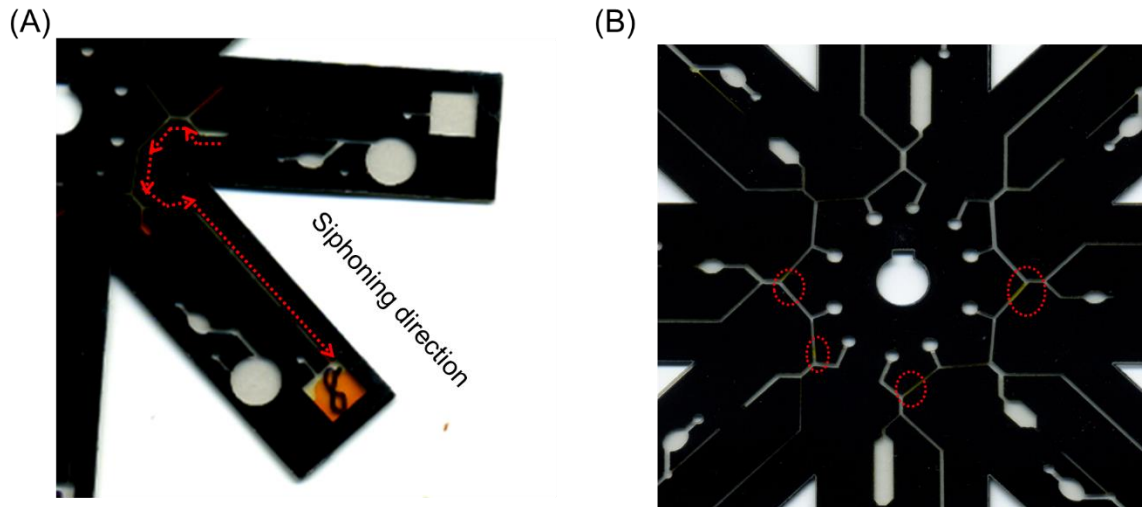


Figure 3-8: Design issues with the earlier prototype microchip for parallel metering. (A) A photograph showing a metering failure due to the undesirable siphoning effect during the overflow spinning step. Liquid in a metering chamber flows into a square-shape waste chamber. The siphoning direction is highlighted in red arrows. (B) A photograph showing a metering failure due to the non-synchronous break-off at the intersection of the distributing channel at the first aliquot stage. Residues of the yellow dyes are circled in the image. *Although the downstream design of the metering chamber is different from the sketch design, this PeT microchip has the same metering fluidic network shown in Figure 3-7.*

channel is draining to the waste chamber, the nearest aliquot chamber is still connected to the waste chamber, allowing for siphoning from the aliquot chamber to the waste chamber. As a result, the aliquot chamber could only be partially filled. A second issue, that is, the non-synchronous break-off at the intersection of the distributing channel with the inlet of the aliquot chamber at the first aliquot stage, which may result in small plugs of liquid in the distributing channel (Figure 3-8B). This effect might be more pronounced with viscous liquids (e.g., blood plasma). The residue liquid in the distributing channel can be problematic for accurate delivery of the desired aliquot volume if the residues flow to the adjacent aliquot chamber during the subsequent high RPM step.

To counteract the siphoning effect, each aliquot chamber was directly connected to an air vent (Figure 3-1). In this way, air plugs are readily supplied to the distributing chamber to displace the fluid flowing to the waste channel, thus, inhibiting the siphoning effect. To minimize the residue liquid flowing to the metering chamber, the upper point of the aliquot chambers is placed at the top part of ‘V’ structure in the distributing channel, being closer to the center of the chip (Figure 3-1). Conversely, the upper point of waste channel is placed on the bottom tip of the V structure so the waste channel is separated from the air vent by a small segment of distributing channel. With this design, if any small residue remains in the distributing channel after the first aliquot spinning, it can be favorably guided to the overflow channel during the second spinning.

3.4.3 Measurement of aliquotted volumes

Theoretically, each aliquot volume can be derived linearly from measuring the liquid area in the aliquot chamber if the chamber depth is constant. However, Do Lago et al., observed that the channel depth decreases as the distance from the channel wall increases due to the deformation of the transparency during the thermal lamination⁶. In addition, it is impossible to visualize the extruding liquid plug on the black toner patch, making it difficult to gauge the volume of the liquid based on visualized area. As a result, the aliquoting process was validated, not on a five layer chip but on two individual three-layered microchips, one for sample aliquoting and the other for buffer aliquoting. Each of these validation microchips shared the same aliquoting design (distribution channel, metering chambers and venting holes) as the five-layer Pet microchip, with the exception that a 400 μm wide serpentine channel (Figure 3-9) to replace the reciprocating mixing unit. Do Lago et al., determined that, for a 400 μm wide channel, the intra channel depth variation is only $\pm 2 \mu\text{m}$ ⁶.

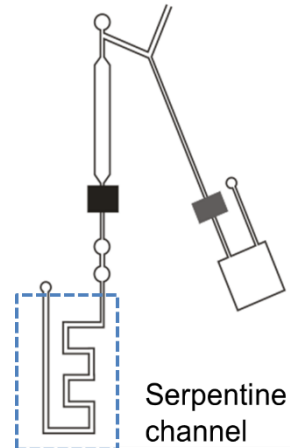


Figure 3-9: Design of the serpentine channel that used for measuring the aliquot volume.

In addition, with the fixed setting of parameters in the microchip fabrication described above (i.e., lamination pressure and speed), the serpentine channel had a depth of $132 \pm 7 \mu\text{m}$ that incorporated variation in both the thickness of Pe film and the toner layers. Although the geometry of the curved meniscus cannot be accurately measured, based on the dimensions of the channel and contact angle of the liquid, the uncertainty in the volume stemming from the meniscus is estimated to be small as 10 nL. Given all above

consideration, the actual delivered aliquot volume should be derived linearly from the measured area in the serpentine channel.

In order to derive a calibration curve from the liquid volumes and measured areas, different volumes of yellow dye were pipetted into the serpentine channels. Images of this structure were obtained with a desktop scanner and an isodata algorithm that was used to count the number of the pixels representing the yellow dye. A linear relationship between the pixel number and the pipetted volume is given in Figure 3-10A ($R^2 = 0.999$). The coefficient of variance (C.V.) associated with the pipetted volumes (e.g., 19.8% for 250 nL, 1.4% for 1.5 μ L, 5% for 2 μ L) were determined through image analysis and, generally, agreed with the pipetting coefficient of variance provided by the manufacturer (12% for 250 nL, 2.5% for 1.25 μ L and 1.4% for 2.5 μ L) although were slightly larger¹⁴. The slightly larger C.V. might be attributed to the inter-channel depth variation and uncertainty in determining the rough channel edge (estimated as 1-2 pixels, this corresponds to a

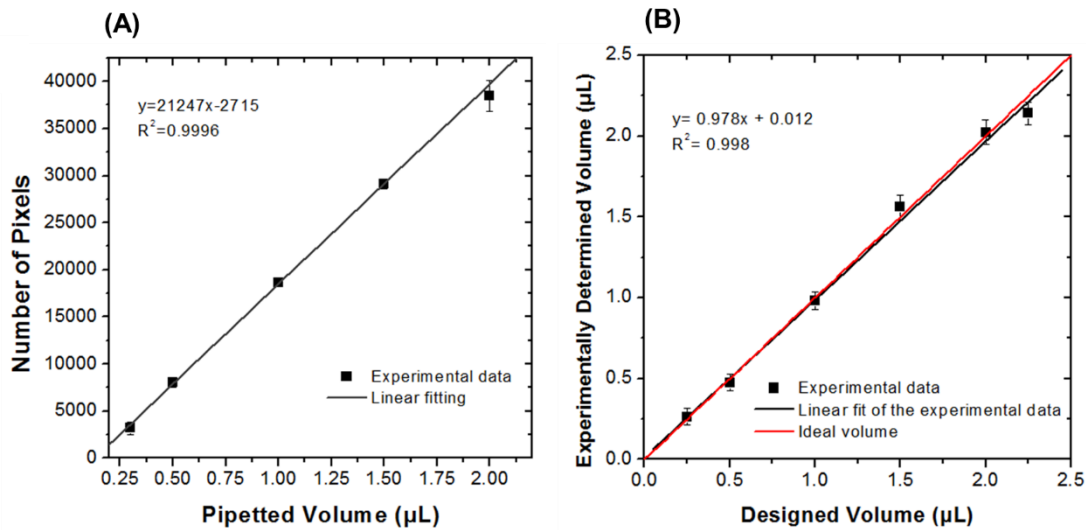


Figure 3-10: Validation of metering performance on chip. (A) Calibration curve correlating pixel number in yellow with aliquot volume of yellow dye (n=4) in serpentine channel. (B) Comparison of empirical volume with calculated aliquot volume on PeT microchip (n=4).

measurement error of ~ 10 micron). Nevertheless, the value for coefficient of determination (R^2) confirmed that the liquid volume in the serpentine channel can be proportionally derived from pixel number.

In the evaluation of the on-chip aliquoting performance, the same yellow dye was loaded and, after a two-step aliquot process which has been described earlier, the number of pixels in each serpentine channel was determined by the same image analysis used for the calibration experiments. The experimentally-determined metered volume was calculated by plugging the number of the pixels into the calibration linear fitting curve. Figure 3-10B shows the correlation between the experimentally-derived aliquot volume and the theoretically-calculated volume based on the area of the metering chamber and average total thickness of the Pe film/toner layers. Standard deviation for an aliquot volume $<1 \mu\text{L}$ is 48-56 nL, while aliquot volumes between $1.5 \mu\text{L}$ and $2.25 \mu\text{L}$ had a standard deviation of 58-78 nL. Since most analytical techniques use relative measurements, the aliquot microfluidic network on PeT microchip demonstrated a satisfactory precision for the proposed application.

Given that the depth of the buffer and sample aliquoting levels were the same, the dilution ratio can only be adjusted via the area of the metering chambers. Thus, the dilution range on the PeT microchip demonstrated here is limited to one order of magnitude. However, dilution by two orders of magnitude can be achieved with the same design if the depth of sample and buffer aliquoting chambers are varied by using Pe films of two different thickness (i.e., $15 \mu\text{m}$ and $110 \mu\text{m}$).

3.4.4 Characterization of reciprocating mixing

Efficient mixing is essential to rapid assays, especially for those involving large molecules (e.g., DNA and protein), which are associated with small diffusion coefficients. As a means of defining the applicability of this mixing design, the mixing efficiency with liquids of varied viscosity was tested on a PeT microchip design that only had a single reciprocating mixing domain (Figure 3-11). To visualize the mixing, two dye solutions were used, yellow dye (tartrazine in 0.1 M HCl) and red dye (phenolphthalein in 0.08 M NaOH). The viscosity of the solutions were adjusted by the addition of glycerol. As the two solutions were loaded to the L2 and L4, an orange color resulted from partial mixing; if they were completely mixed, the final mixed solution turns into yellow. One could quantitate the extent of mixing by evaluating ‘Hue profiles’ from images of the chip chamber prior to initiating spinning and following every reciprocating mixing cycle. Only

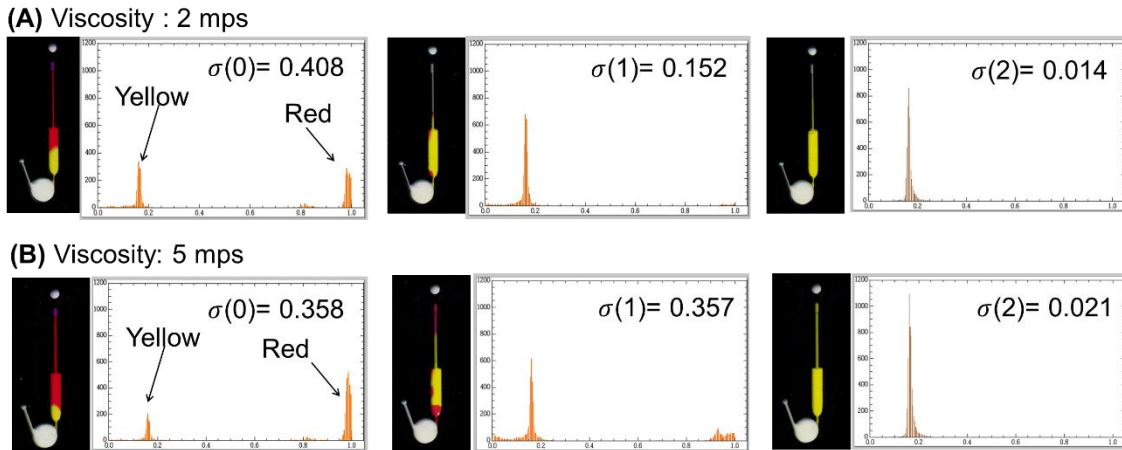


Figure 3-11: Representative snapshots of the dye distribution in the mixing unit as the number of the reciprocating cycle increases ($n=3$) when viscosity is (A) 2 mPa·s and (B) 5 mPa·s. Evaluation of the mixing process was done by analyzing the distribution of dye pixel intensities in the histogram as a function of reciprocating cycles number.

pixels representing the mixture were transferred into a normalized Hue histogram to calculate the standard deviation $\sigma(n)$ is evaluated.

The minimum RPM needed to overcome the capillary action and drive the mixture from the detection chambers to the mixing chamber was first estimated from Eq (3-4) (assuming the contact angle and surface tension is roughly the same DI water). Based on the design shown in Figure 3-1 ($\Delta R = 7.8$ mm *and* $\bar{R} = 39.5$ mm), the minimum rpm required is ~576 rpm. Although the minimum RPM may vary with different mixtures (that will have varied surface tension and the contact angles), the RPM required to pump the mixture back to the high surface energy state (in the mixing chamber) can be experimentally-determined. Since the final aliquot spinning step of is 1200 rpm, the rpm for the reciprocating mixing step was set at 1200 rpm for 15 sec with 5 sec at 0 rpm for backflow by surface tension; this provides sufficient centrifugal force to counteract the capillary action.

Figure 3-11 shows the evolution of $\sigma(n)$ along the reciprocating mixing cycles of two different solutions: 1) dyes in 25% (wt/wt) glycerol (a ~2 mPa·s viscosity, comparable to that of human blood serum) and, 2) dyes in 45% (wt/wt) glycerol (a ~5 mPa·s viscosity, comparable to that of whole blood)¹⁵. The decrease in $\sigma(n)$ is clearly observed as the number of reciprocating cycles increase. After one cycle, a more homogenous mixture was obtained with lower viscosity solutions than that observed with the higher viscosity solution, as is suggested by a greater extent of decreasing $\sigma(n)$ at lower viscosity. However, after two cycles, the histograms from both solutions begin to follow a Gaussian distribution and display a Hue histogram correlating with a homogeneous average of the

two dyes. This was comparable to a mixture prepared in an Eppendorf tube by pipetting and vortexing.

In terms of prior literature¹⁰, a reciprocating mixing unit in a centrifugal platform based on the pneumatic agitation has been reported by Madou et al., where a stream of compressed gas was used to reciprocate liquid between two domains, ultimately enhancing mixing. Although that work exploited the same “spin and stop” actuation, and did not require additional fabrication steps, it required a rotation speed of 7000 rpm. This contrasts the reciprocating mixing domain aforementioned, which requires only a rotation speed of 1200 rpm; a 6-fold decrease in rotation speed, suggesting that the flow can be driven by a CD player. This lower rpm will obviously consume less input energy, allowing for the potential use of inexpensive hardware associated with handheld CD-player, possibly reducing the cost of the hardware and enhancing portability.

3.4.5. Evaluating sample dilution performance

Critical to many assays is the ability to accurately dilute sample or reagents to desirable concentrations. To confirm that the aliquoted samples were diluted with buffer to the requisite ratios, a dye study was carried out using Hue as the readout. Blue and green dyes were loaded into the microchip (mimicking sample and buffer, respectively), and the microchip spun as described in Figure 3-4. The color of the mixture in the detection chamber was scanned and an image algorithm was utilized to calculate the average Hue of each chamber. The data points needed to create a calibration curve were obtained by preparing the standard mixtures in a tube, and then manually pipetting these into individual

mixing units for image capture and analysis. Figure 3-12A plots the ‘green dye volume’ of each mixture against hue, yielding a calibration curve with an exponential fit that provided an equation representing the relationship between dilution ratio and average hue. Figure 3-12B shows that the actual dilution ratio is in a good agreement with the calculated ratio based on the calibration results. This confirms the feasibility of parallel simultaneous aliquoting of sample and buffer into different fluidic levels of the microchannel architecture, and substantiates that effective mixing can be achieved on this five-layer PeT microchip.

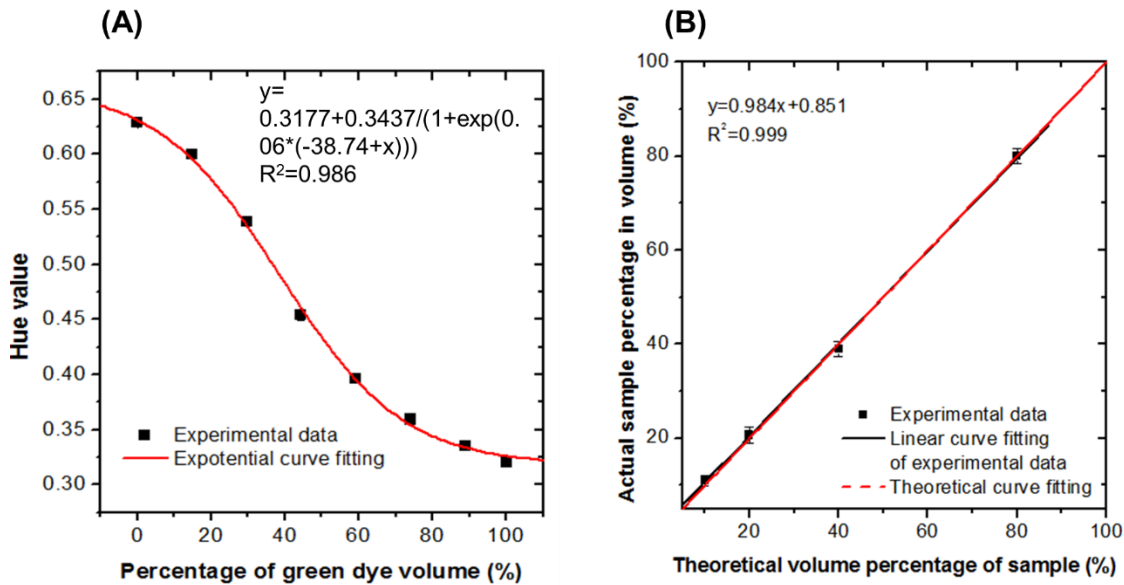


Figure 3-12: Validation of dilution performance by loading blue and green dyes to microchip to mimic the sample reagent and buffer reagent, respectively. (A) Calibration curve correlating the mean intensity of the Hue in the detection zone of the microchip with percentage of $V_{\text{Green Dye}} / [V_{\text{Green Dye}} + V_{\text{Blue Dye}}]$ ($n=4$). (B) Comparison of empirical dilution with calculated metering ($n=4$).

3.4.6 Colorimetric protein assay on the PeT microchip

For many assays used in biochemical or clinical laboratories, it is often necessary to serially-dilute an unknown sample to several different concentrations to obtain at least one concentration that lies within the dynamic range of the calibration curve. For the quantitative assays involving calibration curves that are semi-arbitrary or derived empirically, diluting a sample to multiple effective concentrations assures better accuracy. As a result, it is advantageous to apply the multi-level five-layer PeT microdevice to these types of quantitative assays where dilutions required can be done on-chip and reduce manual pipetting steps and associated human error. For a proof of concept, a colorimetric assay was carried out on the PeT microchip to determine the total protein concentration in human plasma. The protein level in the blood is an indicator of health status. For a healthy adult, the relevant total serum protein concentration is 60-83 mg/mL, which is equivalent to 6.0 to 8.3 gm/dL¹¹. Levels outside this normal concentration range can be indicative of numerous pathologies including kidney disease, liver disease, hyperthyroidism and blood diseases or immune system problems¹⁶.

The calibration curve for the protein assay was generated by pipetting ~2.5 µL of artificial human blood plasma (containing different human serum albumin (HSA) concentrations) and 2.5 µL of tetrabromophenol blue (TBPB) solution to the micromixer domain. Figure 3-13 shows a representative image of the PeT microchip after completing the colorimetric detection of total protein level in the artificial human blood plasma. The area of each detection chamber was ‘cropped’ in Image J to measure the average Hue by image analysis of Hue value described earlier. With the calibration shown in Figure 3-14, the limit of detection (LOD) was calculated using the three times the standard deviation of

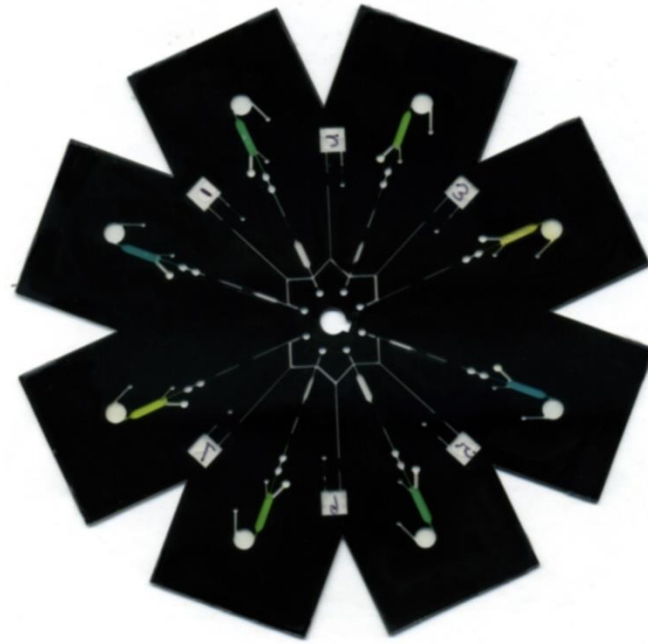


Figure 3-13: Scanned image of the five layer PeT microchip after completing the colorimeter assay.

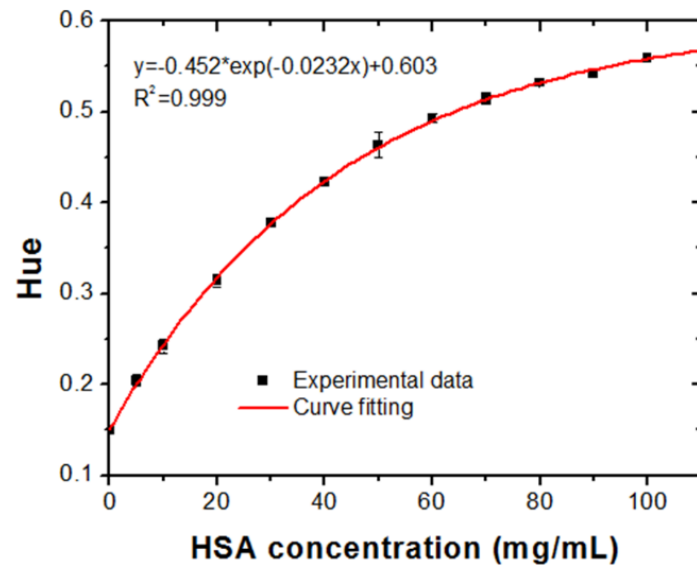


Figure 3-14: Calibration curve for quantitation of total protein concentration in the artificial human blood plasma ($n=3$).

the hue value of the zero concentration of HSA solution, and was determined to be ~5 mg/mL, clearly well below the lower end of the normal range. Increasing the protein concentration from 0 mg/mL to 80 mg/mL resulted in sufficient increases in the Hue value. It is clear that this colorimetric chemistry can differentiate a clinically-relevant low protein concentration (45 mg/mL) from the lower normal limit of the normal range (60 mg/mL). However, the plateauing between 80 and 100 mg/mL suggests that the assay is less sensitive to higher protein levels (Hue value at 70 mg/mL, 80 mg/mL and 90 mg/mL were 0.515, 0.532 and 0.542, respectively, with standard deviation no greater than ± 0.006). Therefore, samples with a protein concentration greater than 80 mg/mL required dilution for accurate quantitation.

The PeT microchip was challenged to quantitate the protein concentration both in the mock samples of human blood plasma (artificial human blood plasma buffer with a spiked HSA concentration) used for calibration, and unknown human lithium-heparin plasma samples obtained from a clinical lab. The sample of interest was loaded into the sample metering layer, while the buffer solution (artificial human blood plasma buffer without HSA) was pipetted into the buffer metering layer. After completion of the two-step metering process, 2.5 μ L of TBPB indicator was pipetted through the reservoir connected to the detection chamber of each micromixer domain, and reciprocating mixing cycles initiated. The entire process, from loading to the final Hue-based detection, required <10 min. When the averaged Hue values for each mixing chamber were plugged into the calibration curve, the post-dilution protein concentration (C_i) was generated. If the Hue value was outside the calibration curve dynamic range, that result was excluded in the final

calculation. The original protein concentration in the mock samples ($C_{protein}$) were calculated from Eq (3-5), expressed as follow:

$$C_{protein} = \frac{1}{n} \sum_1^n C_i \times k_i \quad (3-5)$$

where k_i stands for the particular dilution fold (e.g., 10, 5, 2.5 and 1.25 for the microchip design in Figure 3-1) in that specific micromixer domain.

Figure 3-15A shows the comparison of protein concentration determined on-chip to the spiked concentration of HSA. Note that there is only a small discrepancy between the experimentally-determined protein concentration and the known concentrations of the mock human plasma sample. For the clinical samples, the protein concentration determined on-chip (with an associated C.V. of 7%) agreed well with the values measured by the Biuret reaction on an automated analytical chemistry instrument (Abbott Architect c16000 analyzer) in the Clinical Chemistry Laboratory at University of Virginia (Figure 3-15B). This demonstrated that the PeT microchip was capable of

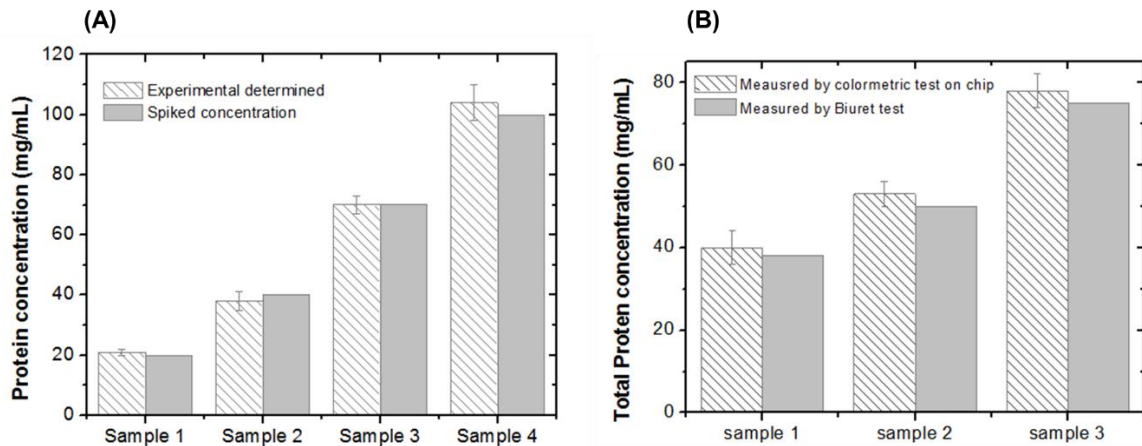


Figure 3-15: Result of protein quantitation on chip for (A) mock samples and (B) real samples of human blood plasma on PeT microchip (n=3).

handling samples with clinically-relevant viscosity, and carrying out an integrated colorimetric assay.

In terms of LOD and dynamic range, the performance of the PeT device was comparable (LOD: ~7 mg/mL and dynamic range: 7-80 mg/mL) to the paper-fluidic device. While the PeT microchips are slightly more expensive than paper-based microfluidic systems, the overall performance of PeT system is superior. This includes precision, dynamic range and speed of analysis, which can be attributed to the exquisite fluidic control and effective on-chip mixing for enhancing the protein-TBPB interaction. Both of these are more challenging on paper, as they are driven by capillary wicking rate, degree of wetting by the sample, and homogeneous distribution of the indicator on the reaction spot all impact performance. That said, it is difficult to argue with the merits of paper-based systems - simple to fabricate, inexpensive materials, and no-power/no hardware devices. Reports have suggested that paper devices could cost as little as a few to ten of cents¹⁷, providing obvious benefit to global health in resource-limited areas. The cost for mass-manufactured PeT microdevices could be as low as tens of cents/ sample. Furthermore, the PeT hardware that could be as simple as a handheld CD-like devices with embedded microprocessors that run algorithms to control spin speed, scan detection chambers colorimetrically and process the data against calibration curves.

3.5 Conclusion

The work in this chapter presents the feasibility of using a simple fabrication procedure that involves ‘laser print, ablate and laminate’, to construct intricate, 3-D

microfluidic structures on a five-layer polyester-toner microchip with two fluidic levels. The open fluidic architecture, passive valving/mixing functions, and ability to laser print valves during fabrication are all attractive features. In addition, the cost for low rate manufacture (in the lab setting) is <\$2 per device and, upon mass production, could potentially be decreased by order of magnitude. Driven by centrifugal force, valving actuation and mixing is rotation speed controlled and requires no more than a battery-powered CD-player with rotation speeds achievable by a handheld player.

Unique to the design is the multi-level microfluidic configuration enable aliquoting and simultaneous dilution from nL to μ L range with effective mixing manner for samples with biologically-relevant viscosities. Detection is colorimetric, utilizing a \$100 desktop scanner to determine hue which, against a calibration curve, allowed for demonstration of a protein quantitation assay. It compares favorably with paper-based microfluidics, both in simplicity and cost-effectiveness, but outperforms paper systems with better precision, faster analysis time (3-fold), better dynamic range and, unlike paper systems, was able to accurately quantitate samples above the normal protein concentration range. This is important because plasma protein concentration >83 mg/mL can be indicative of bone marrow condition, amyloidosis, multiple myeloma and HIV/AIDS¹⁸.

This system represents a step toward an integrated, portable device for point-of-care analysis. The versatility of the PeT microchip can be further enhanced by coupling it with other technologies, e.g., integrating a filter membrane (e.g., Vivid™ Plasma Separation Membrane) on the sample loading reservoir and incorporating dried, on-chip stored reagents. One can envision enhancing portability by supplanting the desk scanner with a smart phone with image processing functionality¹⁹ to create a fully-automated assay

protocol that eliminates error-prone handing steps and reduces the human exposure to reagents with rapid ‘sample-to-result’ capabilities.

3.6 Reference

1. M. Grumann, J. Steigert, L. Riegger, I. Moser, B. Enderle, K. Riebeseel, G. Urban, R. Zengerle, and J. Ducr  , *Biomed. Microdevices*, 2006, **8**, 209–14.
2. Z. Nie, F. Deiss, X. Liu, O. Akbulut, and G. M. Whitesides, *Lab Chip*, 2010, **10**, 3163–9.
3. A. V Govindarajan, S. Ramachandran, G. D. Vigil, and P. Yager, 2012, 174–181.
4. G. R. M. Duarte, C. W. Price, B. H. Augustine, E. Carrilho, and J. P. Landers, *Anal. Chem.*, 2011, 5182–5189.
5. J. Tian, D. Kannangara, X. Li, and W. Shen, *Lab Chip*, 2010, **10**, 2258–64.
6. C. L. do Lago, H. D. T. da Silva, C. A. Neves, J. G. A. Brito-Neto, and J. A. F. da Silva, *Anal. Chem.*, 2003, **75**, 3853–8.
7. A.-L. Liu, F. He, K. Wang, T. Zhou, Y. Lu, and X. Xia, *Lab Chip*, 2005, **5**, 974–8.
8. Y. Ouyang, S. Wang, J. Li, P. S. Riehl, M. Begley, and J. P. Landers, *Lab Chip*, 2013, 1762–1771.
9. N.-T. Nguyen and Z. Wu, *J. Micromechanics Microengineering*, 2005, **15**, R1–R16.

10. Z. Noroozi, H. Kido, R. Peytavi, R. Nakajima-sasaki, and A. Jasinskas, 2012, **064303**.
11. S. J. Vella, P. Beattie, R. Cademartiri, A. Laromaine, A. W. Martinez, S. T. Phillips, K. a Mirica, and G. M. Whitesides, *Anal. Chem.*, 2012, **84**, 2883–91.
12. L. Liu, C. L. Qiu, Q. Chen, and S. M. Zhang, *J. Alloys Compd.*, 2006, **425**, 268–273.
13. D. Mark, T. Metz, S. Haeberle, S. Lutz, J. Ducr  , R. Zengerle, and F. von Stetten, *Lab Chip*, 2009, **9**, 3599–603.
14. www.eppendorf.com
15. P. Garstecki, M. J Fuerstman, M. a Fischbach, S. K. Sia, and G. M. Whitesides, *Lab Chip*, 2006, **6**, 207–12.
16. [www.webmd.com/a-to-z-guides/total serum-pro](http://www.webmd.com/a-to-z-guides/total-serum-pro)
17. A. W. Martinez, S. T. Phillips, B. J. Wiley, M. Gupta, and G. M. Whitesides, *Lab Chip*, 2008, **8**, 2146–50.
18. www.mayoclinic.org/symptoms/high-blood-protein/basics/causes/SYM-20050599
19. L. Shen, J. a Hagen, and I. Papautsky, *Lab Chip*, 2012, **12**, 4240–3.

Chapter 4: A Laminated Microdevice for Multiplexing Cell Counting by Magnetic Bead Aggregation on a Rotating Platform

4.1 Introduction

Particle-based agglutination assays have been widely used in medical diagnoses, food analysis, and environmental monitoring^{1,2,3}. In a typical particle-based agglutination, when a sample containing analyte is mixed with the uniformly disperse particles that are chemically-modified, agglutination or clumping of the microspheres is observed due to the specific interaction between particles and analytes, indicating a positive result⁴. By using particles to amplify or visually indicate a specific interaction event, qualitative detection can be directly achieved via the naked eye⁵. When using spectrophotometers or digital CCD cameras in place of the human eye, quantitative analysis is also feasible and can usually result a better detection limit⁶⁻⁸. In the early development of the particle-based agglutination assays, polystyrene beads (also known as latex particles) were used. While the material is non-biofouling, the kinetics of the assay are limited by the passive diffusion of the analyte to the bead surface. Thus, a lengthy incubation time is often needed for detecting biomolecules with low diffusivities (i.e. DNA, protein). As an alternative to the latex beads, magnetic particles (MP) can be used to expedite the speed of assays. The magnetic properties of the MPs enable non-contact manipulation of the particles by a magnetic field to generate effective mixing⁹⁻¹³, which not only enhances fluid-phase kinetics for bimolecular binding, but also increases the colliding frequency between the particles¹⁴. Application of magnetic-beads to immunoassays has been successfully

demonstrated with a several-fold reduction in analysis time while offering a lower detection limit^{7,15,16}.

Recently, our group developed a magnetic, silica bead-based assay (also known as the ‘pinwheel’ assay) for quantitation of DNA⁶. The method was later evolved to enumerate DNA-containing cells as the DNA mass from the lysed cell is proportional to the cell number. In the presence of a static magnetic field, magnetic beads suspended in chaotropic salt buffers form pearl-chain like structures. When the magnetic field rotates at a certain frequency, MP chains attempt to align themselves with the field direction^{17–20}. While the induced magnetic dipole holds the chain integrated, breakup of chains can happen due to the arising shear force. Thus, MP chains remain visually disperse. On the contrary, chaotropic-driven adsorption of DNA to the silica-coated MP surface has been observed to stabilize the chain formation and lead to formation of readily observable aggregates, providing a positive result by direct visual detection. The quantification of DNA or DNA-containing cells can be obtained by simple image analysis of the amount of aggregation. This approach only requires inexpensive bench hardware: (1) a stir plate to generate a rotating magnetic field, (2) a 20 μL circular open-microwell on poly(methyl methacrylate) for an assay reactor, (3) a CCD camera for optical detection; it provides pg-sensitivity for DNA and detects down to 2 white blood cell in a 20 μL microwell within 5 min. Considering its simplicity and sensitivity, it is appealing to use the pinwheel assay as a cost-effective alternative to more expensive DNA or cell detection, especially in the low-resource conditions.

However, the reported pinwheel assay is not readily adaptable to automation and multiplexing due to several inherent limitations. Although the open-microwell reactor

facilitates the pipetting of reagents and samples, integration of the pinwheel assay to sample preparation up-stream can be difficult. Moreover, the pinwheel process is vulnerable to the contamination and evaporation. While the rotating magnetic field generated by a stir plate seems to be sufficiently robust and reliable, the pinwheel reaction has to be centered in the magnetic field for the optimum magnetic manipulation. Thus only one sample can be processed at a time. The limitation of the current pinwheel assay is manifested when applying it to quantitative detection. For example, to quantitate an unknown sample, serially diluting the samples to multiple concentrations so that the final concentration is within the dynamic range of the pinwheel assay is often necessary. Therefore, numerous steps for pipetting and repeated magnetic field actuators are involved in quantitative pinwheel assay, making it laborious and lengthy.

With advances in microfabrication and consumable electronic technologies, Lab-on-a-disc technologies have been boosted over the last decade. By spinning the disc-like microchip, centrifugal flow induced on fluid drives liquid radially outward from the spinning center to the perimeter, during which stepwise reaction initiates. Due to the rotational symmetry of the centrifugal flow, replication of identical microfluidic flow can be easily realized on a single microfluidic disc, which facilitates the multiplexing of assays and reduces the cost per run. The feasibility of using a disc platform for integration and multiplexing assays has been successfully demonstrated through a wide variety of applications including immunoassays, polymerase chain reaction, DNA analysis, cell analysis and others^{21,22,23}. Chapter 3 highlights the applicability of using a polyester toner (PeT) microchip as a disposable disc platform for multiplexing a protein quantitation assay. As demonstrated in Chapter 3, even though the fabrication process is simple and low-cost

compared to that of other thermoplastic disc platforms, the PeT disc provides all the essential fluidic controls such as pumping, valving, and mixing.

This chapter presents the first PeT disc platform for the pinwheel assay as a potential solution to improve sample throughput while reducing hands-on operation. To avoid numerous pipetting steps, a closed microfluidic network was designed and multiplexed on a PeT disc platform that integrates the parallel sample dilutions and the pinwheel assay. A simple bi-directional magnetic field was built and optimized for simultaneous actuation of the circular array of pinwheel assays on a PeT disc. The feasibility of conducting the pinwheel assay in a close-well format with a new magnetic field was verified through detection of pre-purified human genomic DNA. Finally, enumeration of white blood cells (WBC) in human blood samples was demonstrated on this new platform with sufficient sensitivity and accuracy for clinical purposes.

4.2 Material and Methods

4.2.1 Reagent

Tris base was bought from Fisher Scientific and EDTA was bought from Sigma-Aldrich. 8 M GdnHCl buffer was prepared by dissolving GdnHCl salt (MP Biomedicals, Solon, OH) in 1 ×TE buffer and the pH is adjusted to 6.1 by 100 mM MES (Acros Organics).

30 µL of Magnesil paramagnetic particles (Promega, Madison, WI) was washed once with deionized, distilled water (Nanopure, Barnstead/Thermolyne, Dubuque, IA)

followed by one wash with GdnHCl buffer and resuspended in 500 μL of GdnHCl solution to make the suspension. Whole blood samples were donated by consenting donors.

4.2.2 Device design

The PeT microchips are circularly shaped discs (diameter = 120 mm) and designed for centrifugal liquid handing on multiple levels. Each disc comprises four identical and independent domains. Each domain has a sample inlet reservoir and a buffer inlet reservoir, each of which is connected to a different metering microfluidic network on the top level (for sample metering) or bottom level (for buffer metering) of the disc (Figure 4-1). As sample is loaded from the sample reservoir on the top level of the disc, it automatically primes to a sloping feed channel and fills in five finger-like metering chambers. Two different types of hydrophobic toner valves were used in this design: one has a higher burst

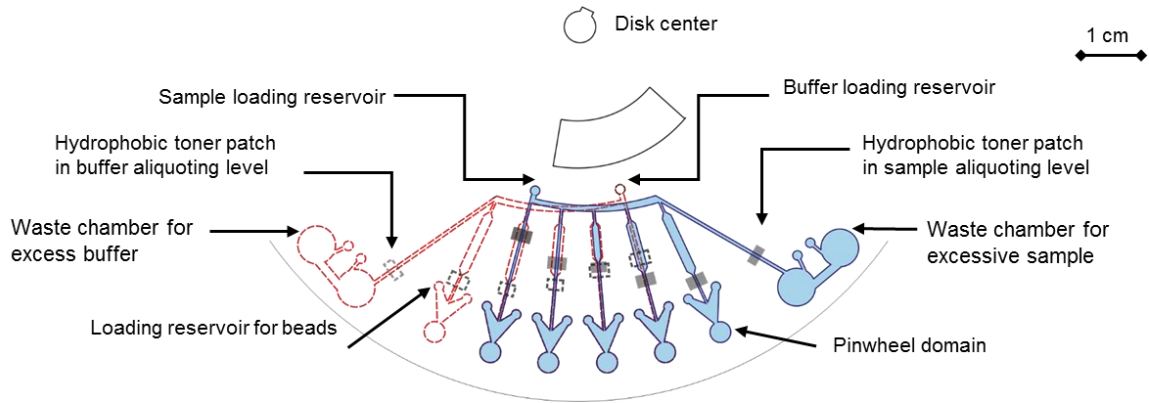


Figure 4-1: Schematic of the microfluidic multilevel design for sample metering (top level outlined in blue) and buffer metering (bottom level outlined in red) on a CD-like cell counting microchip for centrifugal system. The most left pinwheel domain only connects to buffer metering layer serving as negative control. Dilution folds of the second left pinwheel domain to the very right one are 10, 5, 2.5, 1.25 and 1 respectively.

pressure and is connected to the metering chambers. The other toner valve connected to the waste chamber has a lower burst pressure. The burst pressures of the hydrophobic toner valves were controlled by the printed toner density, detail of which can be found in previous work²⁴. By printing the downstream surface of the metering chambers with toner to make it hydrophobic, each metering volume can be defined. The buffer metering network on the bottom level of the disc was designed in a similar way. Distribution of the liquid can be improved by the slope of the feeding channel and rotation direction of the disc.

On the outer diameter of the disc, there are six mixing chambers, a buffer waste chamber, and a sample waste chamber. Four mixing chambers are connected with a pair of sample and buffer metering chambers that are overlapping each other. The volumes of the overlapped sample and buffer metering chambers are varied to provide four different dilution folds (i.e. 1.25, 2.5, 5 and 10 fold) with a consistent final volume of 2.5 μL . The first mixing chamber either from left or right shown in Figure 4-1 are only connected to the individual buffer or sample metering chambers respectively, to serve as a negative or positive control respectively. The total loading volume for sample or buffer for each domain is $\sim 13 \mu\text{L}$. Each mixing chamber is composed of a round-shape pinwheel detection well and a downward-pointing triangle shape chamber which connects to the beads loading reservoir and metering chambers. The downward-pointing triangle shape was designed to better guide the MPs solution (1.1 μL) from loading reservoir to the pinwheel detection well. The volume of the pinwheel detection well is designed to be 3.6 μL . In such manner, the dilute sample and MPs solution can fill the entire pinwheel detection well, leaving only a small liquid meniscus in contact with air and thus minimizing the evaporation.

4.2.3 Device fabrication

To fabricate disc with a multi-level design, each PeT disc is made of five distinctive Pe layers (3M, CG5000) that have been modified accordingly based on their roles in functionality. The detail of the disc fabrication and the implementation of hydrophobic valves has been reported elsewhere²⁴. Figure 4-2 shows the breakdown of the layers. The bottom side of the top Pe layer (L1) was patterned with black hydrophobic toner patches (HP laserjet 4000, HP C-4127X) with laser-ablated reservoirs and air vents according to the sample metering design shown in Figure 4-1. The microfluidic channels for sample metering were laser ablated through the second Pe layer (L2) that was uniformly coated by cyan toner (Brother) on both sides. The reason for using cyan toner instead of black toner will be explained in the “Image Detection” section. The top surface of the third Pe layer (L3) was patterned with the hydrophobic toner patches identical to L1. No metering

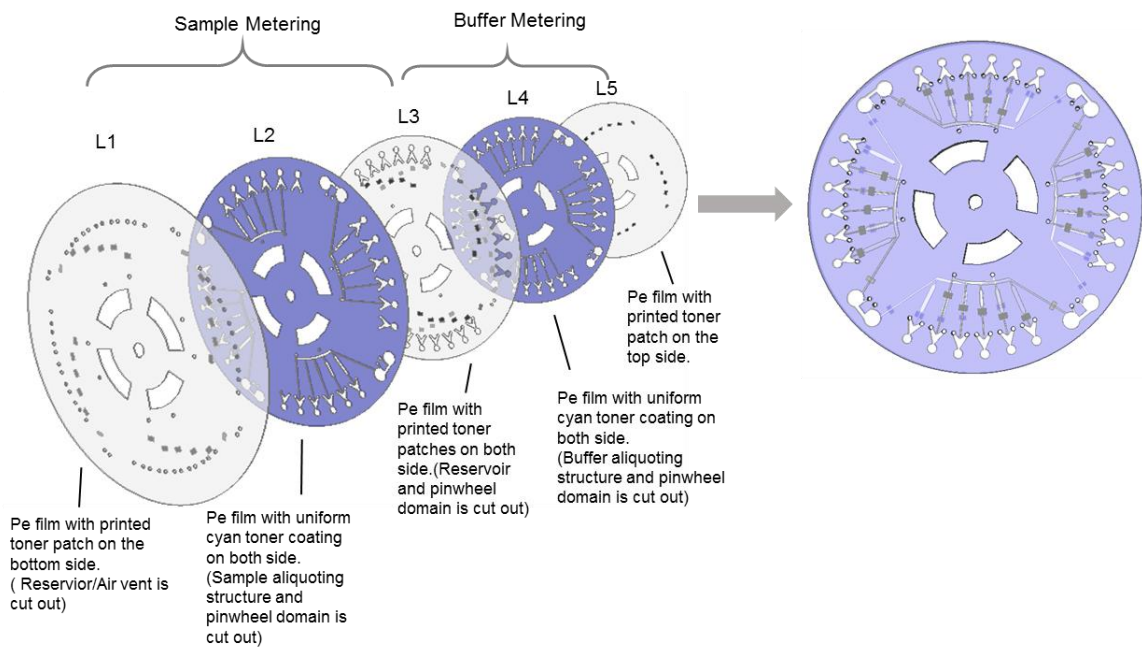


Figure 4-2: Assemble process for multi-level microfluidic PeT microchip.

channel was cut out on the L3 so that the metering level of sample and buffer would be separated from each other, and thus could be operated independently. However, the mixing chambers were cut on L3. In addition, the connecting holes for buffer loading and air venting were cut on both L1 and L3. The sample metering level was defined by L1 to the top surface of L3, while the buffer metering structure was defined by the bottom surface of L3-L5. The bottom surface of L3 and top surface of L5 were patterned with black hydrophobic toner patches to define the hydrophobic valves for the buffer metering level. The modification of the fourth Pe layer (L4) is similar to L2, which provides the microfluidic feature for buffer metering. Once all five layers were fabricated, the layers were aligned together and laminated by an in-house modified heated roll laminator (UltraLam 250B) with a temperature of 150 °C and estimated speed of 8 mm/second. During the lamination, only the cyan toner coatings on L2 and L4 that were in contact with the neighboring layers (L1, L3, and L5) were melted to function as adhesive for bonding.

4.2.4 Operational procedure of the PeT disc platform

The full process of the multiplexed pinwheel assay from reagent loading to detection on a PeT disc is schematically illustrates in Figure 4-3. The PeT disc was attached to a PMMA plate that was screwed on a spinner set-up that has been described in earlier work²⁴. After loading the sample to the top level of the PeT disc, the disc was spun clockwise at 300 rpm for 1 min. In this first step, only the hydrophobic valve connected to the waste chamber with lower burst pressure was opened to allow overflow of the excessive sample, while aliquots of sample in each metering chamber were still retained.

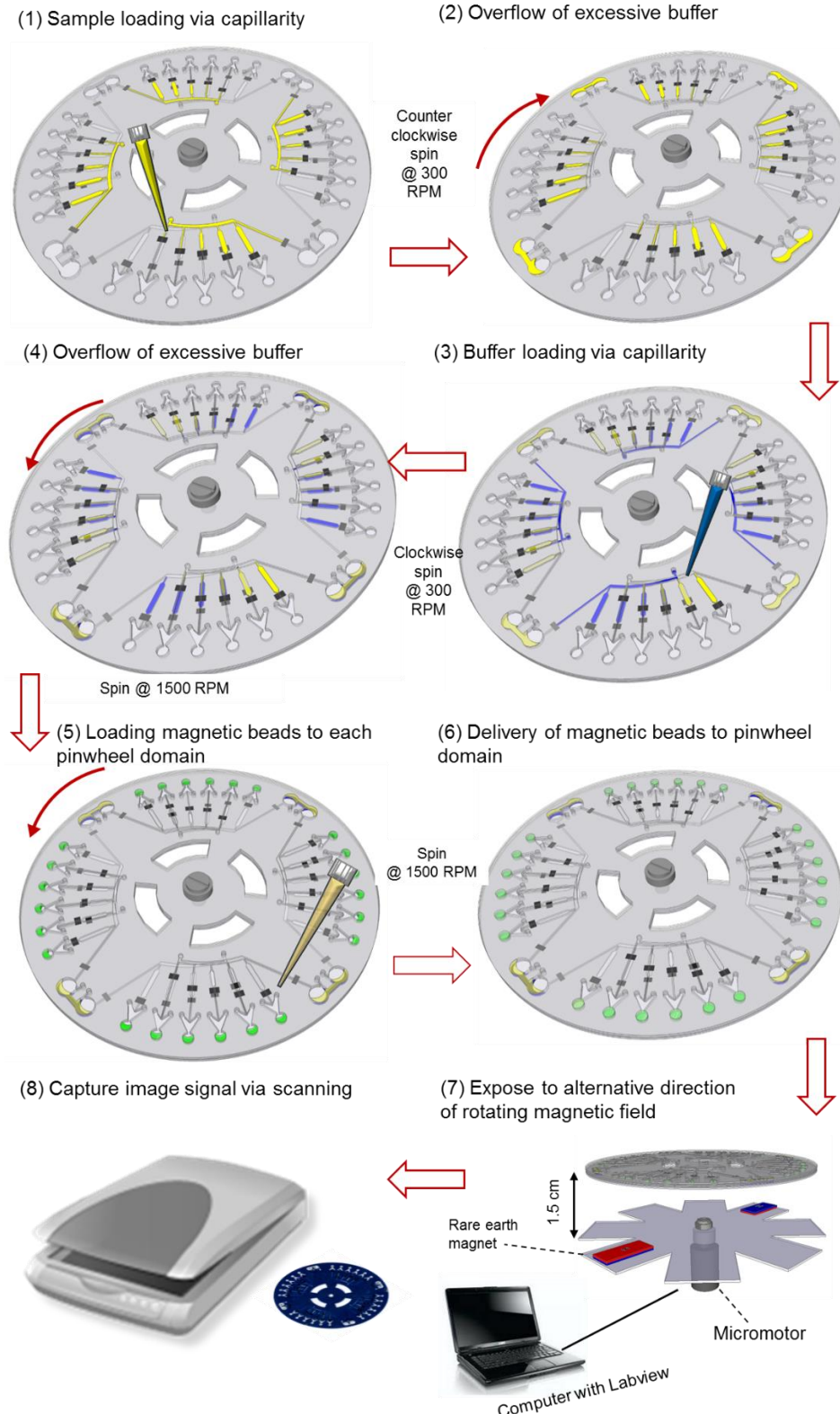


Figure 4- 3: Sketch of the operational procedure on the PeT microchip for cell counting.

Next, buffer was loaded to from the top reservoir to the bottom level of the PeT disc, followed by a counterclockwise spinning at 300 rpm for 1 min. As a consequence, metering of the buffer was achieved by the similar overflow method used in the first sample metering step. The PeT disc was then spun at 1500 rpm for 30 second, which generated enough centrifugal pumping pressure to burst the hydrophobic valves of all the metering chambers. As a result, metered sample and buffer were forced to the pinwheel chamber, where mixing occurred.

With diluted samples in the pinwheel domains, magnetic beads were pipetted to the reservoir adjacent to each pinwheel domain, followed by another spinning at 1500 rpm for 30 second which delivered the beads to the pinwheel domain. Then, the PeT microchip was transferred to a static stage. Another PMMA plate with two magnets was screwed on to the same spinner setup to function as a bi-directional rotating magnetic field (bi-RMF). The PeT disc was positioned above the bi-RMF by 1.5 cm. The bi-RMF rotated at a desirable rpm with a reversal frequency of 0.5 Hz for 5 min, during which DNA induced-magnetic bead aggregation can occur. Finally, the PeT microchip was transported to a flatbed scanner for optical detection.

4.2.5 Bi-directional rotating magnetic field

The reusable magnetic module comprises a pair of permanent magnets (BX082-N52, NdFeB, 1.2 mm wide, 25.4 mm long, and 2.5 mm thick; K&J Magnetics, Inc., Jamison, PA) with opposite magnetic polarities facing upwards (Figure 4-3). The two magnets were adhered to a 2 mm thick disc-shaped PMMA plate by double-sided adhesive

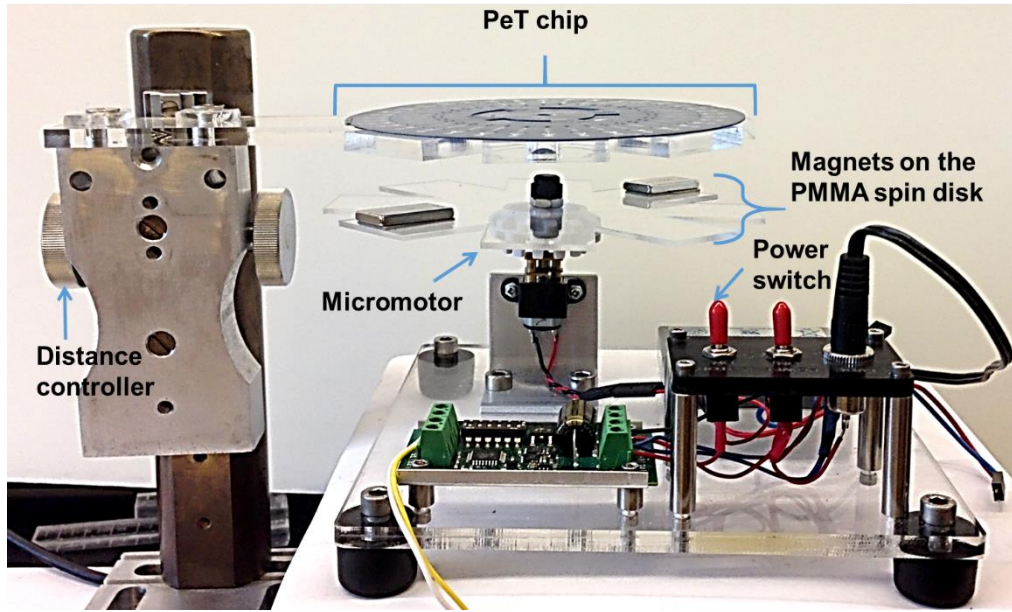


Figure 4-4: A photograph of the bidirectional magnetic setup. The spinning magnetic field are composed of two identical rare earth magnets glued to a PMMA disk with different pole facing to the bottom of the CD microchip.

tape so that they could be attached to the spinner setup (Figure 4-4). The distance between the centers of each magnet to the center of PMMA plate is 53.3 cm, which is the same as that between the center of pinwheel chamber and that of PeT disc. When the PMMA plate with the two magnets is spinning, pinwheel chambers on PeT microchip are exposed to the magnetic field from each magnet alternatively.

4.2.6 Image detection

After bi-RMF actuation, the PeT disc was scanned by a desktop scanner (Epson Perfection V100 Photo Scanner) at 2400 dpi and 24 bit color resolution. TIFF image files of each pinwheel chamber were cropped in Image J software and processed in the form of HSB (hue-saturation-brightness) color space with an isodata algorithm written in

Mathematica software. Pixels representing the cyan toner are first discarded by setting a hue-based threshold. The rest of the pixels are processed into binary with a saturation threshold to differentiate the beads from the white background. If the concentration of DNA increases, the beads start to aggregate, and thus, the number of pixels representing the beads decreases. The number of dark pixels (Dark Area) was normalized to the negative control (no DNA added).

4.2.7 Multiplexed pinwheel assays on PeT disc for cell counting

To establish the calibration curves, 5 μL raw human blood samples with known white cell counts were first incubated with 8M GdnHCl solution in either in 1:800 or 1:1600 volume ratio at room temperature for 30 min. After vortexing for 1 min, the samples were loaded onto the PeT disc as the procedure described above. Three scanned images of the beads and aggregates were acquired for image analysis. The calibration curves were generated by correlating the mean dark area (DA) value of the three images for each diluted sample, with the corresponding final dilution fold in the pinwheel chambers.

To determine the white cell counts in the unknown blood samples, 5 μL raw human blood samples were first incubated with 8 M GdnHCL in 1: 1600 volume ratio as room temperature for 30 min, followed by the same disc operation and image analysis used for generating the calibration curves. The concentration of the white blood cells in blood was acquired by comparing the Dilution threshold (Dt) value with the calibration curve, the detail of which will be explained and discussed in the “*Result and Discussion*” section.

4.3 Result and Discussion

4.3.1 Validation of metering performance

A crucial aspect in the liquid handling on PeT disc is reliable and precise metering. The successful metering process is dependent on the serial arrangement of metering chambers and the rotational direction. The optimized design to simultaneously meter different volumes of a sample is to arrange the metering chambers according to the size of metering chamber. In other words, chamber of larger volume should be placed further from the waste chamber while chamber of smaller volume should be placed closer to the waste chamber (Figure 4-1). During the overflow spinning step, the disc is spun in the opposite direction of the liquid flow. This combination prevents an undesirable siphoning

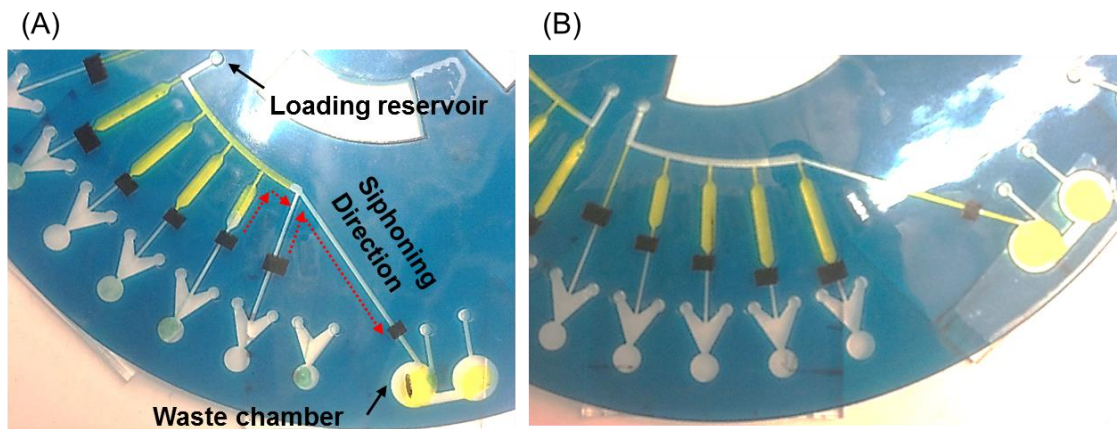


Figure 4-5: Photographs of two aliquoting design prototypes taken after completing the first spinning step. (A) In the earlier design, the volume of the metering chamber decreases from the sample loading reservoir to the waste chamber. This arrangement causes undesirable siphoning effect: liquid in the first and second smallest chambers flow to the waste chamber during the first spinning step. (B) When the sequence of metering chambers is reversed, there is no siphoning effect, ensuring a successful metering. *Although the downstream design of the metering chamber is different from the sketch design in Figure 4-5, this PeT microchip has the same metering fluidic network.*

effect (Figure 4-5) from the smaller metering chambers to the waste chamber during the overflow process.

The quantitation method used to evaluate volume metering has been established in Chapter 3. In brief, two types of individual three-layered microchips were fabricated for sample and buffer metering evaluation respectively. The microchips share the same metering design from either the sample or buffer layer but has a 400 μm wide serpentine channel to replace the mixing chamber. Yellow dye was used to mimic sample or buffer for better visualization. The resulting metered volumes can be determined by the observation of the filling level of each calibration channel in relation to its actual volume which was measured beforehand (Figure 4-6). Figure 4-7 and Figure 4-8

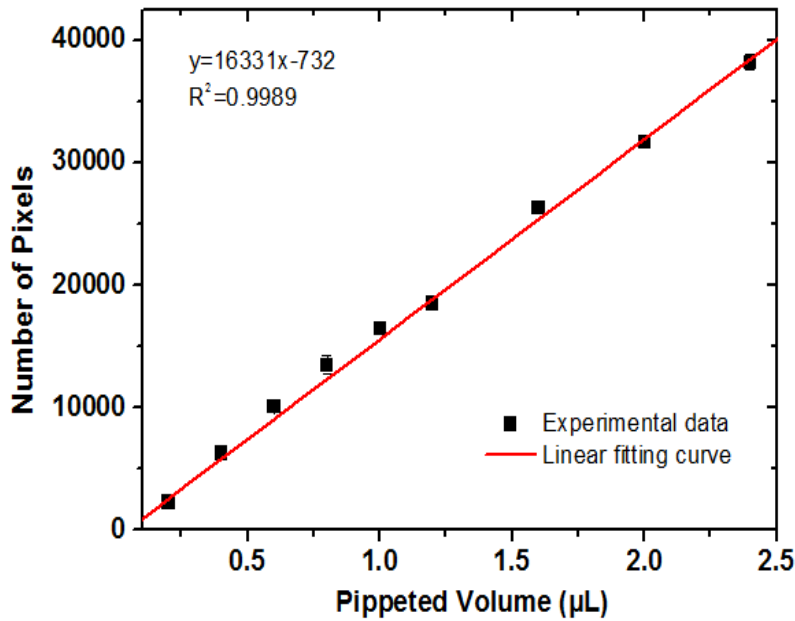


Figure 4-6: Calibration curve correlating pixel number in yellow with metering volume of yellow dye (n=4).

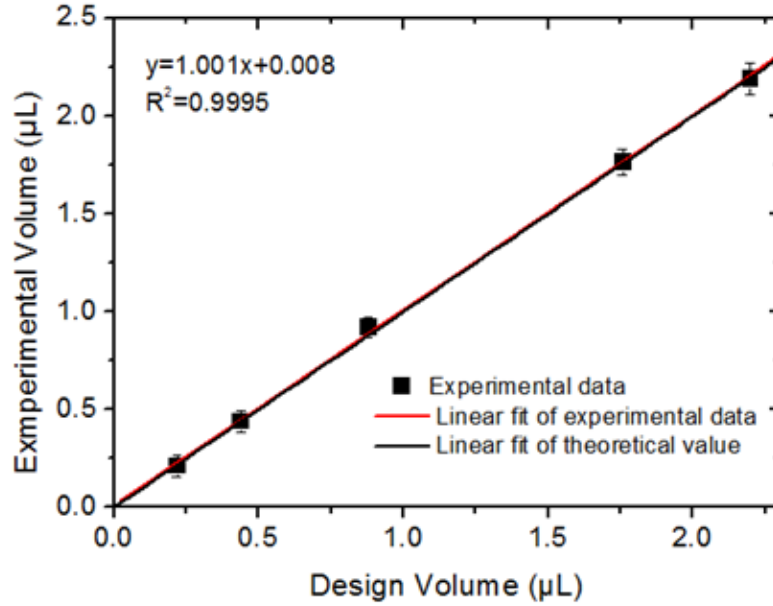


Figure 4-7: Comparison of empirical volume with calculated metered volume on sample metering layer (n=4).

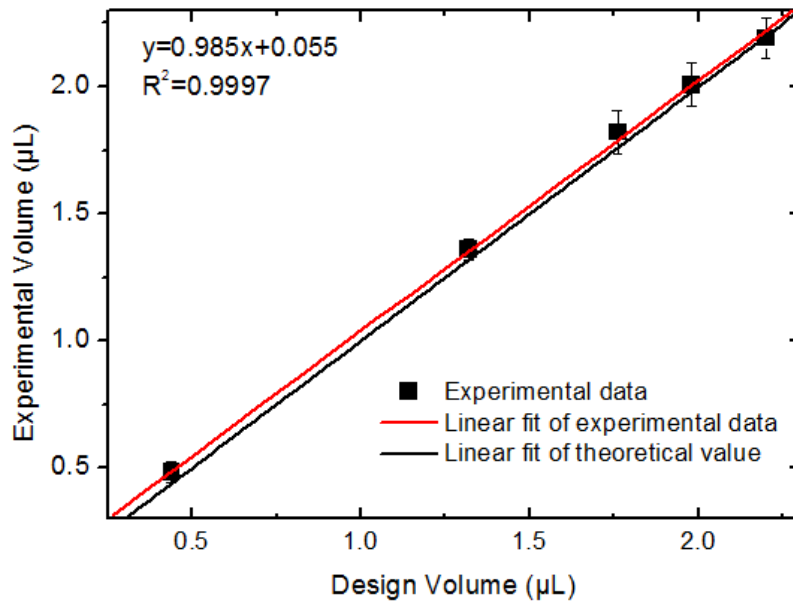


Figure 4-8: Comparison of empirical volume with calculated metered volume on buffer metering layer (n=4).

show the correlation between the average experimental-determined metered volume and the theoretically calculated volume based on the dimension of the metering chambers. The systematic deviations for metering above 0.5 μL are all less than 4% and a non-systematic variations were lower than 5%. As a reference, the standard EN ISO 8655 for multichannel piston pipettes demands a systematic deviation of less than 5% and a non-systematic variation lower than 5% for nominal volumes of 1 μL . A general greater systematic deviation and non-systematic variation were found for the metering volume below 0.5 μL . For example, the systematic deviation and non-systematic variation for metering of 0.44 μL were estimated to be 10% and 9% respectively. The larger error for smaller metering volumes can be possibly attributed to imperfect alignment of layers with toner patches and limitation of using image detection for volume determination that was discussed in Chapter 3. Nevertheless, the achieved precision is generally acceptable for the requirements of the presented pinwheel assay.

4.3.2 Movement of beads under bi-directional magnetic field

Rotating magnetic fields that are created by electromagnets can lead to undesirable heat generation for biological samples. Instead of using a rotating electromagnetic field, two rare-earth magnets were used to induce the magnetic field on the PeT disc, which is more cost-efficient and portable. The response of the beads to the rotating magnetic field was monitored by a CCD camera. Figure 4-9 shows the snapshots of magnetic beads acquired every 5 seconds in a bi-RMF rotating at 200 RPM. After spinning the beads into the pinwheel chamber, the beads accumulated at the bottom of the pinwheel chamber due

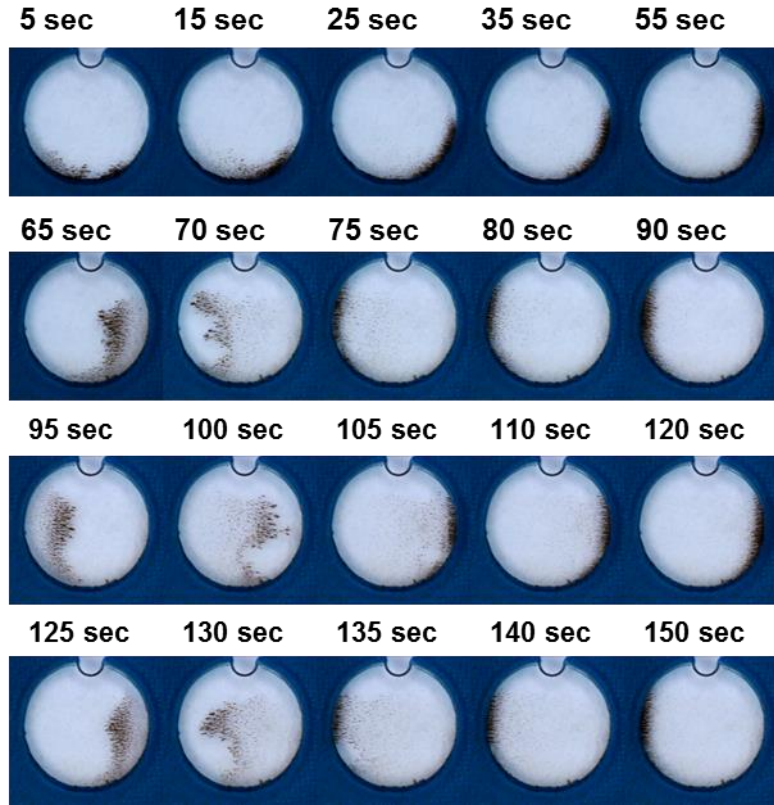


Figure 4-9: Snapshots of the beads movement under bRMF monitored with a digital camera. Beads remained dispersed due to the absence of DNA in the well. Images are taken every 5 seconds. The beads accumulated at the bottom of the well due to the centrifugal force from the spinning step. The RMF was spun clockwise for 1 min to move all the beads to one side of well, and then its rotation direction was reversed every 30 seconds.

to the centrifugal force. It was experimentally determined that the beads required 60 seconds to travel from the bottom of the pinwheel chamber to the one side of the pinwheel chamber with continuous spinning of the magnetic field in one direction. Without changing the rotation direction of the magnetic field, the beads were confined to the side of the pinwheel chamber, which increased both bead collision probability and contact time. Only by reversing the rotating direction of the magnetic field were the beads directed to the other side of the pinwheel chamber, during which the mixing of beads and DNA occurred. As

the rotating direction of the magnetic field reversed periodically, reciprocating movement of beads in the pinwheel chamber was observed.

To confirm whether the magnetic field can promote/activate DNA-induced bead aggregation, 500 pg of human genomic DNA was added to pinwheel chamber (Figure 4-10). Distinct formation of bead aggregates was observed and it remained in highly aggregated state through entire process. In contrast, without adding the DNA, redispersion of the beads was observed in the neighboring pinwheel chamber while the beads traveled within the pinwheel chamber (Figure 4-9). Due to the closed-well format on PeT disc and high salt concentration of the assay condition, even though the total volume of the pinwheel

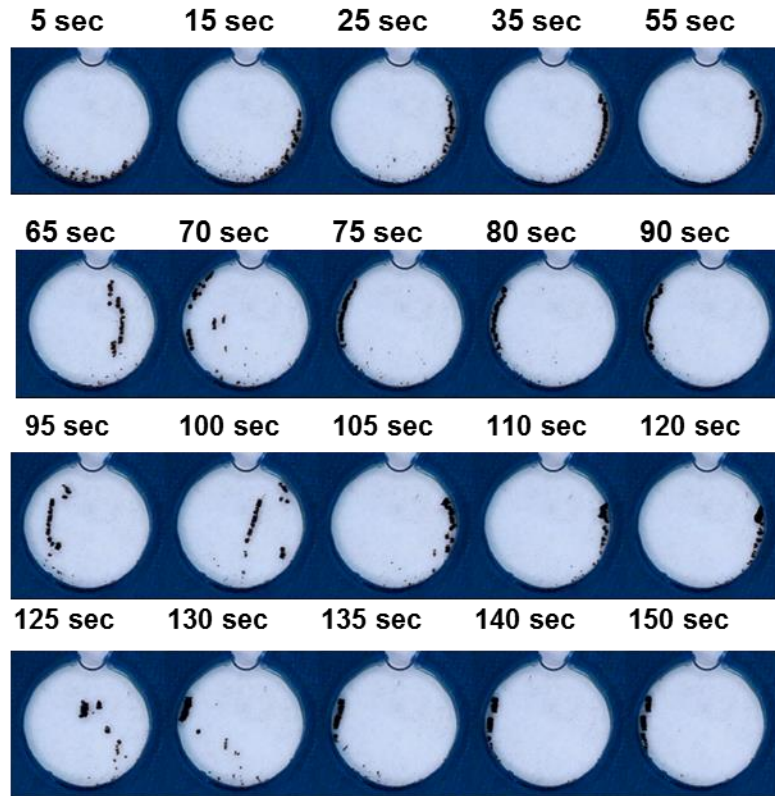


Figure 4-10: Snapshots of the beads movement under bRMF monitored with a digital camera. Beads aggregated in the presence of 500 pg hgDNA.

chamber is only 3.6 μL , significantly smaller compared to 20 μL in the open-well format, there was no observable evaporation of liquid during the assay.

4.3.3 Influence of rotation frequency of bi-RMF on beads assay

When optimizing the rotation frequency of bi-RMF, the total time for magnetic field exposure was set to be 6 min, which comprised of 1 min to move beads from the bottom of the pinwheel chamber to one side of pinwheel chamber, and 5 min (same incubation time used in the previous work) of reversing the rotational direction of the bi-RMF every 30 seconds. Various rpms (60 rpm, 200 rpm and 800 rpm) were investigated

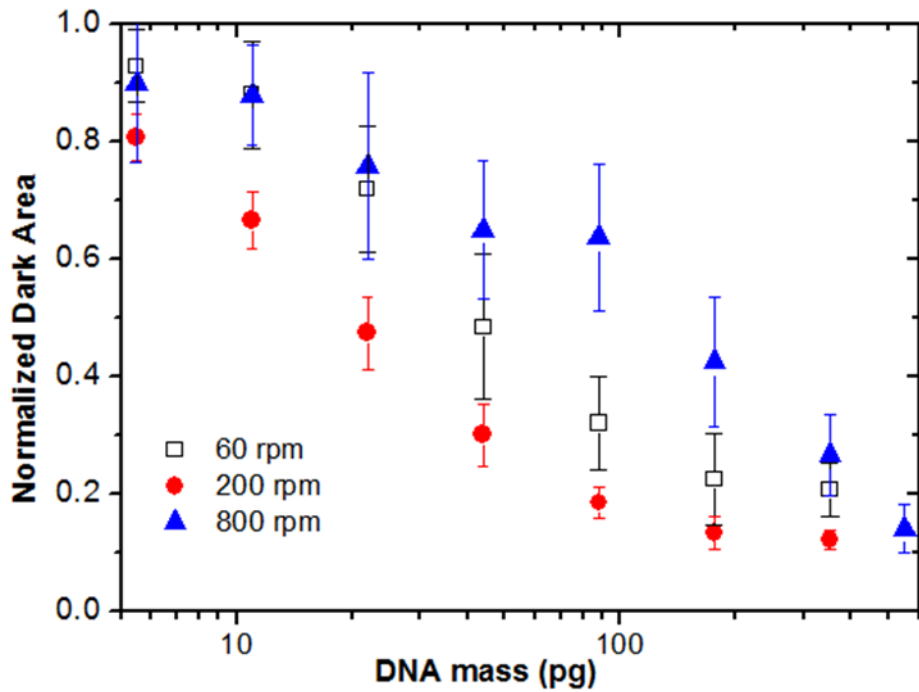


Figure 4-11: Comparison of the calibration curve for purified human genome DNA of multiplexed pinwheel assay on chip under different rotating frequency of the magnetic field. The data points are the average of triplicate image analysis of four replicates containing the same mass of added DNA. Error bar stands for one standard deviation ($n=4$).

by evaluating the formation of beads aggregation (Dark Area) as a function of human DNA mass in the pinwheel chamber. As shown in Figure 4-11, the best sensitivity and reproducibility (represented by the error bars) were achieved with 200 rpm as compared to 60 rpm and 800 rpm. It is important to note that a rpm dependence of the average bead velocity was observed: at 60 rpm, the time for beads to move from one side of chamber to the other side of the chamber is ~30 second, which is significantly longer than these for 200 rpm (~15 second) and 800 rpm (~5 second) conditions. A longer traveling time of the beads in the pinwheel chamber should enhance the binding of DNA to beads. However, for the 60 rpm condition, little time was left to confine the beads at one side of pinwheel chamber to increase the collision probability of the magnetic beads. In contrast, for 200 rpm and 800 rpm conditions, there were approximately 15 seconds and 25 seconds respectively to confine the beads at the side of the pinwheel chamber and promote collision and aggregation of the beads. The possible explanation for the 800 rpm condition being inferior to the 200 rpm is that mixing time of beads with DNA might be insufficient and the aggregation could be disrupted by the increase in drag force (due to the increase in bead velocity). Therefore, the optimum bi-RMF condition was chosen to spin at 200 rpm with a reverse frequency of 0.5 Hz for a 6 min assay time.

Under optimized magnetic field parameters, the detection limit of the assay for human genome DNA was found to be better than 5.5 pg/chamber which is comparable to the conventional pinwheel assay conducted in the open-well format. However, dynamic range of the assay here only cover 1.5 orders of magnitudes, one magnitude lower than the conventional format⁶. The decrease in the dynamic range is due to a reduction in magnetic beads amount used in order to be compatible with the smaller volume of pinwheel chamber.

Since each somatic cell contains 6.25 pg DNA, the dynamic range of the pinwheel assay for white cell counting is mathematically estimated to be 1- 28 cell per chamber.

4.3.4 White blood cell counting for crude blood samples

To generate calibration curve for WBC counting, a similar calibration method to that used for a quantitative PCR assay was adopted. WBC counts of five different freshly drawn blood samples were first determined by a flow cytometer at the Clinical Laboratory of University of Virginia. To effectively exploit the dynamic range of pinwheel assay for WBC enumeration, 5 μ L of each blood samples were first lysed with 8M GdnHCL with a dilution ratio of either 1: 800 or 1: 1600 by a 30 min incubation at room temperature. In such a manner, after further dilution on PeT disc, the WBC number in each pinwheel chamber ranges from ~0.5 cell to ~20 cell. The operation of the PeT and bi-RMF was kept the same as discussed previously. Figure 4-12A plots the dark area (DA) as a function of dilution fold for each blood sample. As the dilution fold increased, the total DNA mass in the pinwheel chamber decreased, which consequently resulted in less bead aggregation (DA). A dilution plot of each sample was generated by fitting the DA points at different dilution folds with an exponential curve. A dilution fold at which the dilution plots crossed a certain dark area level was defined as dilution threshold (Dt). The dark area level for determining Dt was chosen in the region where the plots were parallel to each other (Figure 5-12A). A linear correlation ($R^2=0.998$) between the initial white cell number in the sample and Dt was established in Figure 4-12B.

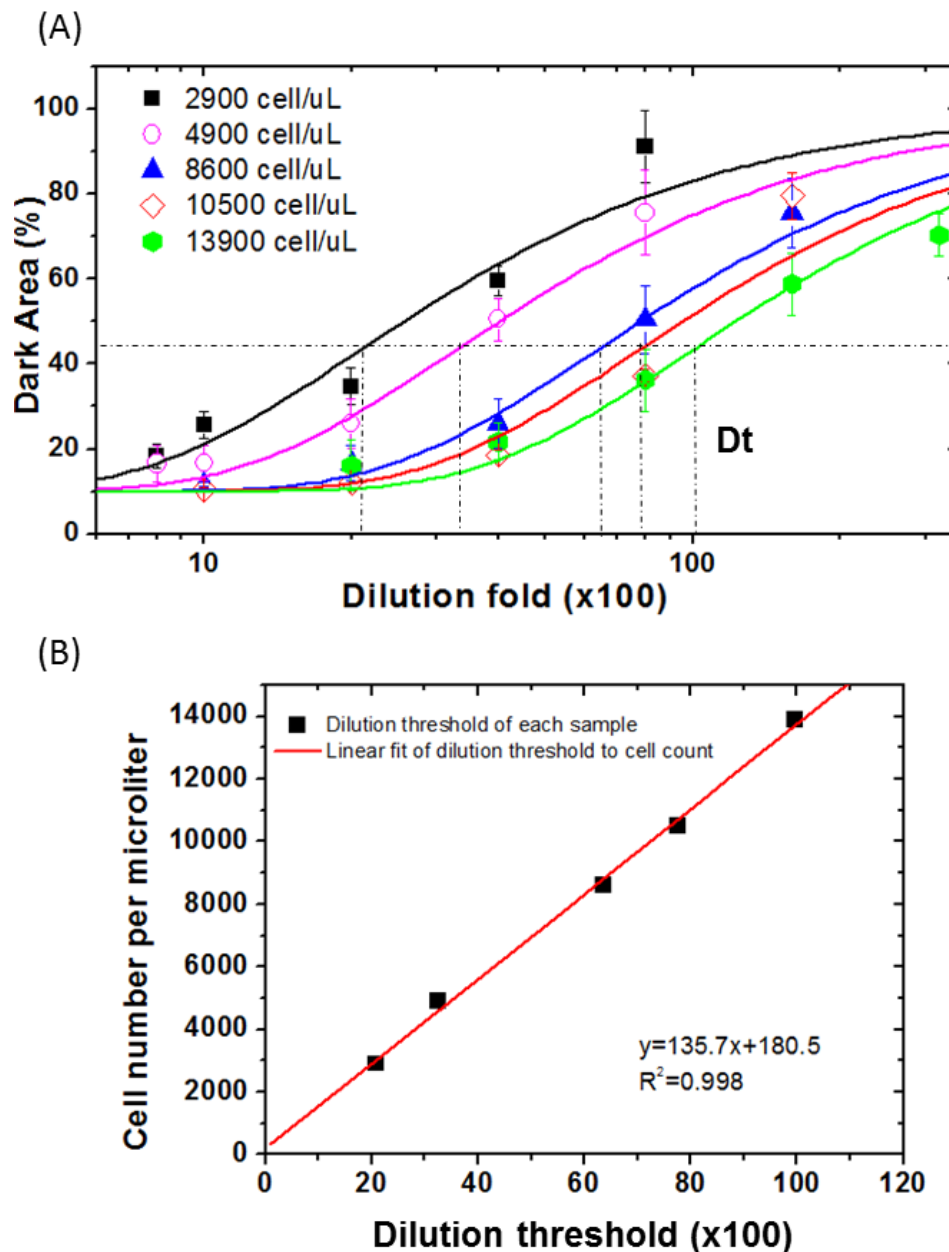


Figure 4-12: Pinwheel responses to the human blood samples with different final white cell numbers in each well. (A)The curves for each sample were generated by fitting the DA to an exponential curve with the general equation: $y=0.9*\exp(-\theta /x)+0.1$. Dilution threshold for each sample is defined as the dilution fold when the dark area is 43.1%, marked by the dotted lines. (B) Calibration curve to correlate the original white cell concentration to the dilution threshold.

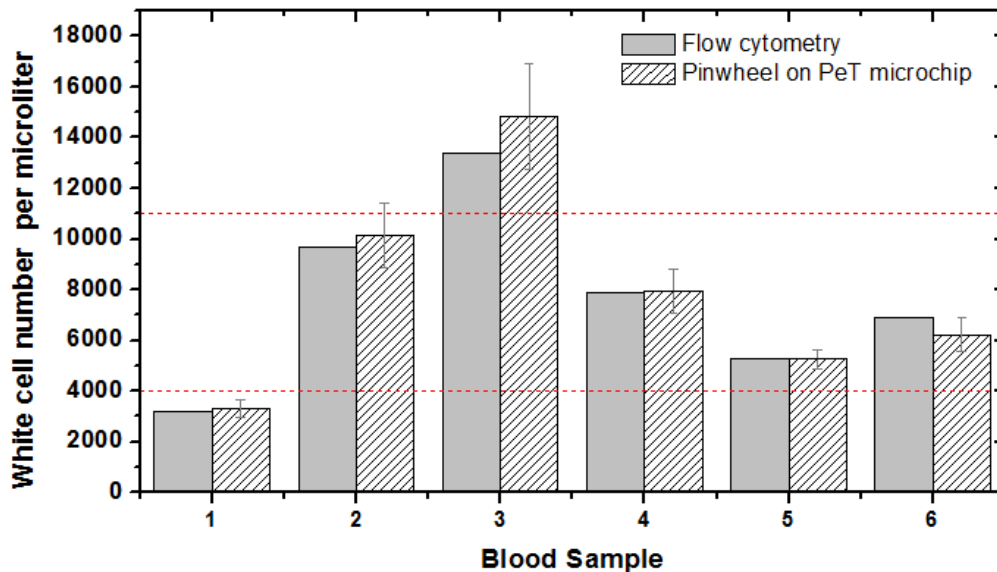


Figure 4-13: Comparison of white cell quantitating by multiplexed pinwheel assay on PeT microchip and a flow cytometer ($n=4$). WBC counts falls in between the red dash line is within the normal range.

To enumerate WBCs in unknown samples, all the samples were first lysed and incubated with GuHCl with a dilution volume ratio 1: 1600. After further dilution on PeT disc, the final dilution fold ranges from 1600 to 16000 (i.e. 1600, 2000, 4000, 8000, 16000). Since the normal range of WBC count of adult generally falls between 3500 and 10500 per μL , at least 3 diluted concentrations out of five are expected to provide a final white cell number that is within the dynamic range of the pinwheel assay. Four replicates were performed on each sample, and the same exponential curve fitting for the DA as a function of the dilution fold was carried out to determine D_t . The D_t was then plugged into the calibration curve to determine the initial WBC count in the blood sample. The determined WBC counts were compared to those independently obtained by the flow cyctometer. As shown in Figure 4-13, the counts from the PeT disc platform compares favorably to those from the flow cyctometer with a C.V. of 10%. In addition, the assay can effectively

identify the counts outside the normal range (bracketed by the two red dashed lines). While the WBC counting performance on the PeT disc platform is comparable to the conventional single open-well platform, the analysis speed and sample throughput were improved significantly (Table 4-1).

Table 4-1: Comparison of WBC counting by conventional pinwheel assay and assay on PeT disc. (Assume 3 different diluted concentrations for one sample and one negative control are required for accurate WBC counting.)

Assay format	Incubation time	Dilution time	Pinwheel assay time	Average detection time /sample
Conventional assay	30 min	4 min/sample	20 min/sample (5 min / concentration)	54 min/sample
Assay on PeT disc	30 min	0.5 min /sample (2 min/4 sample)	1.5 min/sample (6 min /4 sample)	9.8 min/ sample (39 min/4 sample)

4.4 Conclusion

The work in this chapter has demonstrated the feasibility of a low-cost and high-throughput agglutination assay platform for cell counting by combining the advantage of the pinwheel assay, centrifugal PeT platform and bi-RMF. A centrifugal PeT disc was designed to provide automatic sample dilution to five concentrations for optimum pinwheel assay detection with multiple sample throughput. For the first time, the pinwheel assay was conducted in a closed-chamber format for a 5 fold reduction in reaction volume with a comparable limit of detection to the conventional assay. This integrated microfluidic format prevents potential sample contamination and evaporation, while reducing the human exposure to the biohazard. By introducing a simple bi-RMF instrument, pinwheel assays that were circularly arranged on a PeT disc were simultaneously activated and

showed detectable aggregation in 6 min with a significant increase sample throughput. Scanning a PeT disc in an inexpensive flatbed scanner proved to be an effective optical detection for massive data acquisition. Although only WBC quantitation in human blood was successfully demonstrated on this new platform as an exemplary application, the principle of this platform applies across the same applications demonstrated by the conventional pinwheel assay or even other MP-based agglutination assays that have been used for DNA quantification, bacterial drug susceptibility, and virus/bacteria detection.

In order to make the device a truly user-friendly platform for clinical purposes, reagent storage on disc needs to be resolved in the near future. The hydrophobic valves on the PeT disc do not provide a physical barrier, thus the bead solution needs to be manually pipetted to the disc. Accurate metering of bead solution remains challenging on the centrifugal platform due to the density difference between beads and liquid. To make the platform more robust and automated, it is of great interest to investigate methods to dry store the beads on disc, as well as effective techniques to re-disperse the beads once they are rehydrated by buffer. Nevertheless, this work presents significant initial work towards improving the throughput pinwheel assay on a cost-effective, disposable, PeT disc with simple, reusable instrumentation.

4.5 Reference

1. R. V Ramanujan, 2009, 477–491.
2. Y. Weizmann, F. Patolsky, E. Katz, and I. Willner, *Chembiochem*, 2004, **5**, 943–8.

3. I.-M. Hsing, Y. Xu, and W. Zhao, *Electroanalysis*, 2007, **19**, 755–768.
4. L. B. Bangs, *Pure Appl. Chem.*, 1996, **68**, 1873–1879.
5. J. Li, Q. Liu, H. Alsamarri, J. a Lounsbury, D. M. Haversitick, and J. P. Landers, *Lab Chip*, 2013, **13**, 955–61.
6. D. C. Leslie, J. Li, B. C. Strachan, M. R. Begley, D. Finkler, L. a L. Bazydlo, N. S. Barker, D. M. Haverstick, M. Utz, and J. P. Landers, *J. Am. Chem. Soc.*, 2012, **134**, 5689–96.
7. R. Zhang, S. Liu, W. Zhao, W. Zhang, X. Yu, Y. Li, A. Li, D. Pang, and Z. Zhang, 2013.
8. X. Liu, Q. Dai, L. Austin, J. Coutts, G. Knowles, J. Zou, H. Chen, and Q. Huo, *J. Am. Chem. Soc.*, 2008, **130**, 2780–2.
9. T. Kang, M. Hulsen, P. Anderson, J. den Toonder, and H. Meijer, *Phys. Rev. E*, 2007, **76**, 066303.
10. I. Petousis, E. Homburg, R. Derkx, and A. Dietzel, *Lab Chip*, 2007, **7**, 1746–51.
11. M. C. Sorter, 2004, **13**, 779–790.
12. a Rida and M. a M. Gijs, *Anal. Chem.*, 2004, **76**, 6239–46.
13. T. Roy, A. Sinha, S. Chakraborty, R. Ganguly, and I. K. Puri, *Phys. Fluids*, 2009, **21**, 027101.

14. J. Baudry, C. Rouzeau, C. Goubault, C. Robic, L. Cohen-Tannoudji, a Koenig, E. Bertrand, and J. Bibette, *Proc. Natl. Acad. Sci. U. S. A.*, 2006, **103**, 16076–8.
15. R. S. Sista, A. E. Eckhardt, V. Srinivasan, M. G. Pollack, S. Palanki, and V. K. Pamula, *Lab Chip*, 2008, **8**, 2188–96.
16. J.-T. Lee, L. Sudheendra, and I. M. Kennedy, *Anal. Chem.*, 2012, **84**, 8317–22.
17. S. Melle and J. E. Martin, *J. Chem. Phys.*, 2003, **118**, 9875.
18. A. K. Vuppu, A. A. Garcia, and M. A. Hayes, 2003, **87**, 8646–8653.
19. S. Biswal and A. Gast, *Phys. Rev. E*, 2004, **69**, 041406.
20. D. Liu, M. R. Maxey, and G. E. Karniadakis, *J. Micromechanics Microengineering*, 2005, **15**, 2298–2308.
21. M. Madou, J. Zoval, G. Jia, H. Kido, J. Kim, and N. Kim, *Annu. Rev. Biomed. Eng.*, 2006, **8**, 601–28.
22. D. D. Nolte, *Rev. Sci. Instrum.*, 2009, **80**, 101101.
23. J. Ducr  e, S. Haeberle, S. Lutz, S. Pausch, F. Von Stetten, and R. Zengerle, *J. Micromechanics Microengineering*, 2007, **17**, S103–S115.
24. Y. Ouyang, S. Wang, J. Li, P. S. Riehl, M. Begley, and J. P. Landers, *Lab Chip*, 2013, 1762–1771.

Chapter 5: A Disposable Polyester-Toner Microchip for PCR via Infra-Red Mediated Thermal Control

5.1 Introduction

The polymerase chain reaction (PCR) is an indispensable technique in clinical diagnostics, molecular biological and forensic science^{1,2,3}. Conventional tube PCR uses polypropylene tubes as reaction vessels with relatively large sample volumes (15-100 µL), thus, contributing to the cost of analysis. In contrast, the implementation of PCR on microfluidic devices has allowed for scaling down to sub-µL volumes, presenting the possibility for reducing expenditures on costly PCR reagents. In addition, the use of microfluidic devices for PCR application offers several other advantages, including the integration with upstream or downstream analysis step as part of miniaturized micro total analysis system^{4,5,6,7,8}. As a result, implementation of PCR on different microfluidic devices has been extensively explored since 1993 and is being continuously developed^{9,10}.

The early work on microfluidic PCR devices originated in silicon and then was dominated by glass, primarily because of the existing knowledge fabrication process and chemical inertness. However, they are not disposable due to the lengthy fabrication time and high fabrication cost (i.e. use of expensive clean room and hazardous chemicals). Thus, to prevent run-to-run cross contamination (to which PCR is especially susceptible), meticulous cleaning and re-passivation procedures were often necessary before reusing the microchip. The last decade has witnessed a significant transition from using glass/silicon PCR microchips to using polymeric PCR microchips. Benefiting from the

diversity of well-established methods (e.g., CNC machining, CO₂ laser ablation, soft lithography, etc.), prototype polymeric PCR microchips can be fabricated in a few hours at much lower cost (\$2-\$10 compared to \$40+ per glass chip)¹¹. Future manufacturing of those prototype polymeric PCR microchip in large volumes with low cost is possible with well-developed industrial techniques¹², such as multilayer lamination, embossing, and injection molding. Additionally, a number of commercial entities (MiniFab, Chipshop, Aline) have been established to provide service as a foundry. There have been a number of demonstrations of PCR microfluidic system in polymeric microdevices such as PDMS, PMMA, PC, COC, which has been reviewed by Zhang et al recently¹³.

In addition to the common polymeric microdevices mentioned above, Poly(ethylene terephthalate)-Toner (PeT) microchips, fabricated from polyester transparency sheets and laser printer toner, are possibly the simplest and least expensive PCR microfluidic devices. Duarte et al. has explored the potential of utilizing multilayer PeT microchips for solid phase extraction of DNA and PCR¹¹. In their work, it was found that: i) more than 65% of the DNA could be recovered, which is comparable to ~64% efficiency achieved in glass microchips, ii) the resultant DNA was recovered in a small volume yielding a concentrated DNA solution and, iii) the recovered DNA is suitable for the downstream PCR amplification. In addition, large volume (10 µL) PCR amplification of λ-phage DNA was also demonstrated on PeT microchip by placing the microchip direct on the block of a conventional thermocycler, suggesting good thermal stability of PeT microchip for PCR applications.

Considering the great potential of PeT for generating cost-effective, mass-producible yet highly functional microfluidic devices, it is conceivable that PeT

microchips could serve as disposable microdevices for a number of bioanalytical methods that required integrated microfluidic systems. While the individual processes for DNA extraction, amplification and detection have been separately demonstrated on PeT microchips, the mass of DNA (hence, the volume of input sample) required for detectable amplification in 10 μL volume exceeds the capability of the upstream DNA extraction process. Moreover, the large thermal mass of PCR sample and use of a conventional heating-block-based thermal cycling equipment limits the speed for temperature transitioning between 50 and 95 $^{\circ}\text{C}$ (for denaturing, annealing and extension) for 20-40 cycles. Therefore, the improvement of the PCR scheme is critical to an effective integrated PeT microfluidic genetic analysis system.

This chapter presents the first PeT microchip for PCR with more than one order of magnitude reduction in reaction volume relative to conventional vessels (i.e. 25 μL), which are compatible with the IR-PCR system for rapid thermocycling. The first investigation is the dynamic passivation to mitigate the reduction of PCR efficiency on PeT microchip, which rose from the increase in the surface area to volume ratio as reducing the chamber dimension. Using a tungsten lamp as heating source and a miniaturized fan as cooling force, a single-chamber amplification of 520 bp of λ -phage fragment on PeT microchip was demonstrated with a reduced reaction time. The same PeT microchip and IR-PCR setup was then challenged by amplifying a 1500 bp fragment of bacteria genome. The PeT microchip and IR-PCR setup were further advanced to enable multichamber PCR for the first time. Design aspects such as symmetry of chambers configuration were taken into consideration along with selection criteria of IR lamp type to obtain a homogenous temperature distribution within the multichambered

PeT microchip. Characterization of the temperature behavior of the multichamber IR-PCR system was provided. As a proof of the applicability of this technology, simultaneously amplify a region of the human β -globin gene fragment in five sample chambers was carried on a single PeT microchip.

5.2 Material and Method

5.2.1 Reagents

PCR reagents were obtained from Fisher Scientific (Fairlawn, NJ). Primers for amplification of 520 bp fragment of λ -phage and amplification of 390 bp fragment of β -globin gene were synthesized by MWG Biotech (High Point, NC). Primers Y1 and Y3 for amplification of 1500 bp fragment of *Azospirillum Brasiliense*s were synthesized by Invitrogen (Brazil). HinD III digested λ -phage DNA was obtained from Sigma-Aldrich (St. Louis, MO). PEG-200 and bovine serum albumin (BSA) were analytical grade purchased from Sigma. Transparency films (CG 3300 and CG5000) were obtained from 3M (USA).

5.2.2 Microdevice fabrication

PeT microchips were fabricated using a previously described method¹¹. Briefly, polyester sheets are first covered uniformly by toner on both sides using a laser printer (HP LaserJet 4000). The design for the device chambers was drawn using CorelDraw

12.0 software and the chambers were created by cutting with a laser cutter with a 50 watt CO₂ laser (VersaLaser 350, Universal Laser Systems). Four-layer devices were created by sandwiching two polyester layers with precut chambers and coated with toner between uncoated sheets of polyester with precut access holes in the top sheet. The four layers were aligned and laminated using an inexpensive office laminator (Akiles, UltraLam 250B) at 130 °C with a lamination speed of 1 cm/second. Microchips for single PCR amplification experiments were designed to have two chambers (272 µm deep) and 2 µL volume. Figure 5-1 shows the design of microchip and the close-up view of PCR chamber with thermocouple insertion. Microchips for multichambered PCR amplification experiments were fabricated in the same way but with different chamber design (refer to the Figure 5-8 in *Result and Discussion* section).

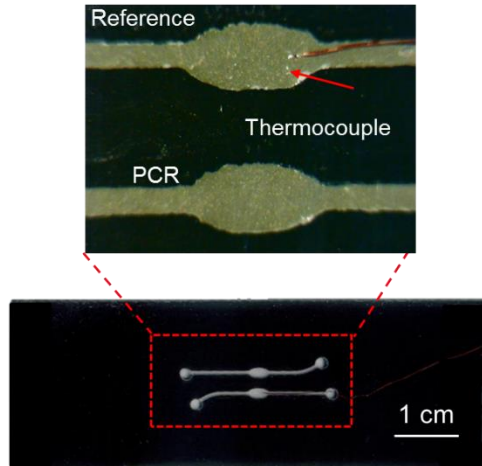


Figure 5-1: Design of PeT microchip for single PCR reaction and close-up view of PCR domain with thermocouple insertion.

5.2.3 IR- mediated temperature control system

The IR-mediated heating system for single PCR amplification on microchip was constructed in-house and it has been described elsewhere^{14,15,16}. Briefly, this IR-PCR setup employs a LabVIEW application to collect the signal output from a miniature type-T thermocouple (Physitemp Instruments) inserted in the reference chamber (Figure 5-2).

The signal was transmitted to a model TAC-386-T thermocouple-to-analog converter (Omega Engineering, Stamford, CT) and further amplified by a simple amplification circuit before being acquired by a data acquisition card (USB6008, National Instruments). In response to the change in temperature, the tungsten lamp and a convective cooling fan were controlled through a proportional-integral-derivative (PID) feedback control algorithm to achieve the set temperature via modulation of duty cycle. The lamp was focused on the PCR chamber. The microchip was covered by aluminum foil mask before start the heating, so that only PCR chamber and reference chamber were exposed to the IR radiation. The IR-PCR set-up used for multichambered PeT microchip was slightly modified by replacing the tungsten lamp with a halogen lamp (MR16, International light, L6409-G), the latter of which has better homogenous heating radiation.

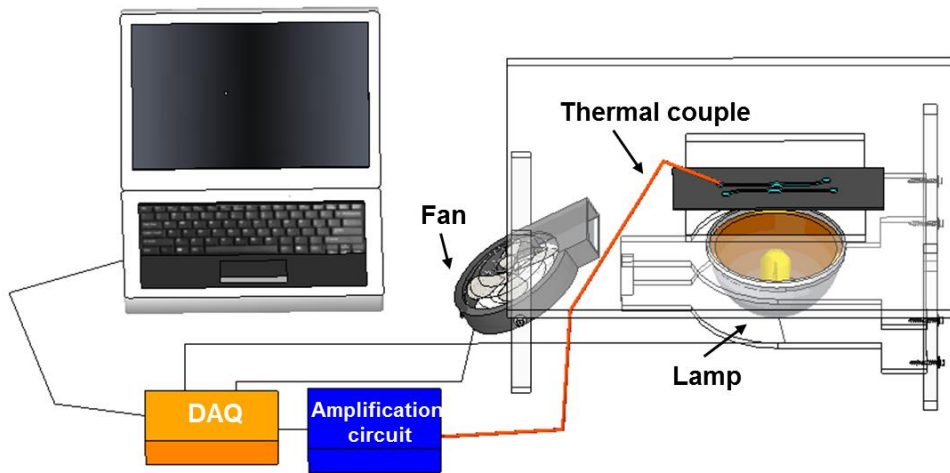


Figure 5-2: Schematic of non-contact thermal cycler using a halogen lamp and blower fan controlled by a LabVIEW program written in-house. Temperature was recorded via a thermocouple in the reference chamber. Note that the chambers and thermal couple are not to scale, and have been enlarged to show structure. The size of IR-PCR step-up is 13 cm wide, 13 cm long and 15 cm high.

5.2.4 Investigation on surface passivation

Pe transparent pieces (1 mm wide and 5 mm long) was obtained by using laser ablation and then added to the PCR tubes. A 520 bp of λ -phage gene fragment was chosen as the target. The master mix consisted of 1 \times Qiagen *Taq*PCR buffer, a total of 2.4 mM MgCl₂, forward and reverse primer each at 0.4 μ M, four dNTPs each at 0.2 mM, 0.2 units/ μ L *Taq* polymerase and 1 ng of λ -phage DNA template. After adding different amount of BSA or PEG to the master mix, the 25 μ L aliquot of master mix was loaded to each tube, followed by 1 min vortexing to ensure a full interaction between the master mix and Pe pieces. The thermal cycling conditions were as follow: an initial hold at 95 °C for 2 min, 30 cycles of 95 °C for 30 second, 68 °C for 30 second, followed by a final hold at 72 °C for 2 min. Tube-based PCR without addition of Pe film was included in every experiment as control. All PCR amplifications were run in parallel in a thermocycler (GeneAmp 2400 Perkin Elmer). After completion of the PCR, the tubes were vortexed and 1 μ L of sample was removed from the tube. Agilent 2100 Bioanalyzer (Agilent Technologies, Inc., Santa Clara, CA, USA) was used to separate and detect the product according to the manufacture's instruction.

5.2.5 Amplification of λ -phage DNA in PeT microchip for single PCR

The PCR master mixture was prepared with the following concentrations for both microchip and conventional tube-control PCR: 10 mM Tris-HCl buffer, pH 8.3, 50 mM KCl, 2.4 mM MgCl₂, 0.4 mM of the each primer, 0.2 mM of each dNTP 0.24 mg/mL of BSA, 1.5% (v/v) of polyethylene glycol-200 (PEG), and 0.2 units/ μ L *Taq* polymerase.

For the positive control in tube-based PCR and on-chip PCR, λ - phage DNA was added to a final concentration of 1 ng/ μ L. The PCR chamber of the PeT microchip was filled with approximately 2 μ L of PCR stock solution by capillary force, while 1 \times PCR buffer was loaded into the reference chamber. Mineral oil was overlaid on the reservoirs to prevent evaporation of solution. The positive control and negative control (lacking λ -phage DNA) carried out in tubes were placed in a conventional thermocycler while microchip PCR was performed using an IR-mediated PCR system. Thermal cycling conditions for tube experiments was as follows, 120 s at 95 °C for initial denaturation of DNA, 30 cycles of 30 s each at 95 °C (denaturation) and 68 °C (annealing/extension), followed by 120 s at 72 °C for a final extension. There were three different thermocycling conditions for on-chip PCR experiments. The first one was the same as the tube-based control listed above. In the second PCR condition, the initial denaturation and final extension were kept the same as the first PCR condition; however, it consisted only 20 cycles of 30 s each at 95 °C (denaturation) and 68 °C (annealing/extension). The third PCR thermocycling is the shortest, and conditions was as follow: 30 s at 95 °C for initial denaturation of DNA, 20 cycles of 10 s each at 95 °C (denaturation) and 68 °C (annealing/extension), followed by 30 s at 72 °C for a final extension. PCR products were removed from the microchip via manual pipetting. Microchip PCR and tube PCR control samples and were analyzed on the Bioanalyzer 2100 using the DNA 1000 kit and microchips (Agilent Technologies).

5.2.6 Amplification of *Azospirillun brasilienses* DNA in PeT microchip for single PCR

The PCR master mixture for *Azospirillun brasiliense* DNA amplification was prepared with the following concentrations for both microchip and conventional tube-control PCR: 10 mM Tris-HCl buffer, pH 8.3, 50 mM KCl, 2.4 mM MgCl₂, 0.3 μM of the each primer, 0.2 mM of each dNTP, 0.24 mg/mL of BSA, 2.5% (v/v) of polyethylene glycol (PEG) 200, 0.15 units/μL *Taq* polymerase. For the positive control in tube-based PCR and on-chip PCR, *Azospirillun brasilienses* DNA was added to a final concentration of 4.6 ng/μL. Thermal cycling condition for tube experiment was as follow, 240 s at 95 °C for initial denaturation of DNA, 30 cycles of 95 °C for 40 second, 62 °C for 40 second and 72°C for 80 second, followed by a final hold at 72 °C for 10 min. PCR products were removed from the microchip via manual pipetting. Microchip PCR and tube PCR control samples and were analyzed on the Bioanalyzer 2100 using the DNA 7500 kit and microchips (Agilent Technologies).

5.2.7 Characterizing the temperature behavior of multichamber PeT microchips on IR-control system

Temperature was measured in 6 chambers simultaneously to assess inter-chamber variation. All miniature thermocouples and temperature sensing systems were first calibrated in a conventional PCR thermal cycler by a standard calibration method described elsewhere¹⁷. After calibration, each chamber was filled with 1× Qiagen *Taq*PCR buffer (Applied Biosystems) and a thermocouple was inserted. The reservoirs were covered with mineral oil to prevent solution evaporation. The prepared PeT

microchip with aluminum foil mask, was centered over the halogen lamp at a distance of 10 mm measured from the rim of the lamp. The temperature behaviors of each chamber were recorded in real-time. The mock thermal cycling PCR condition for measuring the temperature discrepancies between PCR chambers on a single PeT microchip is composed of 5 cycles of 30 s at 90 °C followed by 30 s at 68 °C and 30 s at 72 °C. Mock thermal cycling PCR condition for ramp rate measurement were the following: 120 s at 90 °C, followed by 5 cycles of 30 s at 68 °C and 30 s at 90 °C. Heating rate was defined as $\text{heating rate} = (88 \text{ } ^\circ\text{C} - 70 \text{ } ^\circ\text{C}) / (t_{88\text{C}} - t_{70\text{C}})$ while cooling rate was defined as $\text{cooling rate} = (88 \text{ } ^\circ\text{C} - 70 \text{ } ^\circ\text{C}) / (t_{70\text{C}} - t_{88\text{C}})$. The final ramp rate data shown in the Figure 5-5 was the average results of three repeated experiments.

5.2.8 Multichambered PCR amplification on PeT microchip

For the amplification of a 520 bp fragment of purified λ-phage DNA, the PCR mixture was kept the same as previously described. The thermal cycling was initiated at 91 °C for 120 s, followed by 30 cycles of 30 s each at 91 °C (denaturation) and 68 °C (annealing/extension) ended with 120 s at 72 °C for a final extension.

For the amplification of a 390 bp region of the human β-globin gene, the PCR mixture were contained 1× Qiagen *Taq*PCR buffer, a total of 3 mM MgCl₂, forward and reverse primer each at 0.8 μM, four dNTPs each at 0.2 mM, 0.2 units/μL *Taq* polymerase, 0.24 mg/mL bovine serum albumin (BSA), 1.5 % (v/v) Polyethylene glycol (PEG-200). Human genomic DNA with a final concentration of 4 ng/μL was added to the master mix for on chip PCR amplification and tube-based positive control. The thermal cycling was

initiated at 93 °C at for 2 min, 30 cycles of 93 °C for 30 second, 60 °C for 30 second and 72 °C for 30 second, followed by a final hold at 72 °C for 2 min. Positive control and negative control were conducted by conventional amplification method. The operation of microchip-based PCR on IR mediated PCR setup was the same as previously described except the PCR mixture were loaded to each sample chamber rather than 1× Qiagen *Taq*PCR buffer. Amplified products were removed from the microchip and were analyzed by Bioanalyzer 2100.

5.3 Result and Discussion

5.3.1 Thermocycling on PeT microchip for single PCR amplification

Non-contact heating of the solution was performed on PeT microchip (Figure 5-2) using infrared radiation to excite vibrations of water molecules. Since the Pe film used here does not have significant IR absorption, the vast majority of the radiation is transmitted through the substrate for selectively heating the PCR solution. However, with a temperature measured by the thermocouple positioned at center of the chamber lower than 70 °C, the boiling of aqueous solution at the chamber periphery was observed within a few seconds of powering up the tungsten lamp, made it clear that this was problematic. This was the result of the IR heating the black toner much more rapidly than it heated the bulk sample, creating a large temperature gradient from the periphery to the center of the chamber. Aluminum foil was used to mask the black toner embedded parts of the chip surface so that only the elliptical PCR chamber and

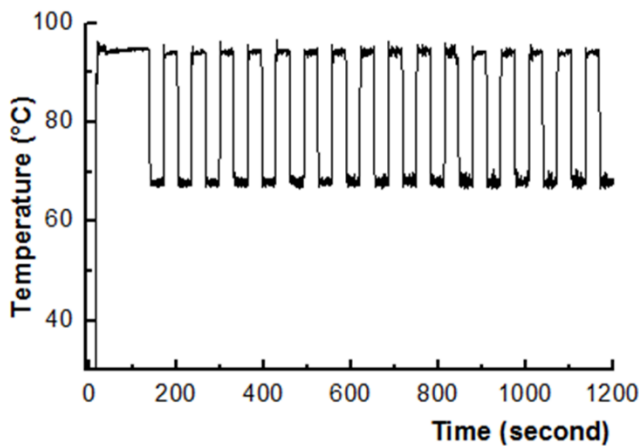


Figure 5-3: Thermocycle profile from infrared heating in a black PeT microchip covered with aluminum foil mask. Only PCR chambers are exposed to the IR radiation from tungsten lamp.

reference chamber were exposed to the IR radiation. The use of the foil mask allowed for a more precise exposure to IR radiation, resulted in a better temperature control (Figure 5-3). The ramp rate for heating solution in the PeT microchip was found to be comparable with glass¹⁷ and polyimide microchips¹⁶ with a heating rate of 10.1 ± 0.7 °C/second and cooling rate of 12.1 ± 0.9 °C/second, suggesting that fast thermocycling could be achieved with this substrate and heating method. The temperature variation when thermostatting at a given temperature was calculated to be ± 0.4 °C for 95 °C and ± 0.6 °C for 68 °C, which is acceptable stability for PCR amplification.

5.3.2 Dynamic surface passivation to enhance the PCR efficiency

The surface area to volume ratio of the PCR chamber containing 2 μL is $9 \text{ mm}^2 \mu\text{L}^{-1}$ ¹ with 95% of the surface contributed from Pe transparency film. In contrast, the surface to volume ratio of a 25 μL aliquot of master mix in a PCR tube is roughly $1.6 \text{ mm}^2 \mu\text{L}^{-1}$.

This high surface area to volume ratio of the PCR on microchip can be problematic with respect to the undesirable absorption of *Taq* polymerase and other reaction components to surface, causing the reaction fouling. Therefore, as is the case for the majority of PCR microchips made from a variety of substrate, surface passivation is essential for successful PCR in PeT microchip as it is the case for the majority of PCR microchips made from different substrates¹⁸. To minimize the reaction inhibition and improve the PCR performance, the feasibility of using dynamic passivation for PeT microchips was explored as it does not require additional steps for surface treatment. It has been suggested that BSA and polyethylene glycol (PEG) can preferentially bind to the wall of the microreactor, preventing the majority of *Taq* polymerase from adhering to the wall, thus improving the PCR-biocompatibility of many types of polymeric microchips^{19,20,21}.

The first investigation was the PCR enhancement protocol via a tube-based PCR in conventional thermocycler. BSA and PEG-200 were added to 25 μL PCR mixture in the microtubes containing 0, 10 or 40 laser-ablated Pe transparent flakes. Because a single Pe transparent flake (1 mm (*w*) \times 5 mm (*l*) \times 0.11 mm (*d*)) with a surface area of 6.3 mm^2 , 40 pieces of Pe transparent pieces in 25 μL of PCR master mix provides a surface to volume ratio equivalent to that on the microchip. Figure 5-4 illustrates that addition of BSA (0.24 mg/ μL) alone to PCR reaction cannot alleviate inhibition effect when the Pe surface to volume ratio increased as indicated by no detectable product by using Bionalyzer when there were 10 or 40 Pe flakes added. Formulating the PCR master mix with the PEG-200 (1.5 % v/v) and BSA (0.24 mg/mL), the loss of amplified product still existed due to the increase of Pe surface to volume ratio. However a reasonable PCR product concentration was regained for the largest surface to volume ratio experimental

condition. Thus, for all the PCR reactions on the microchips in the rest of the paper, PEG-200 and BSA were added to the PCR mixtures.

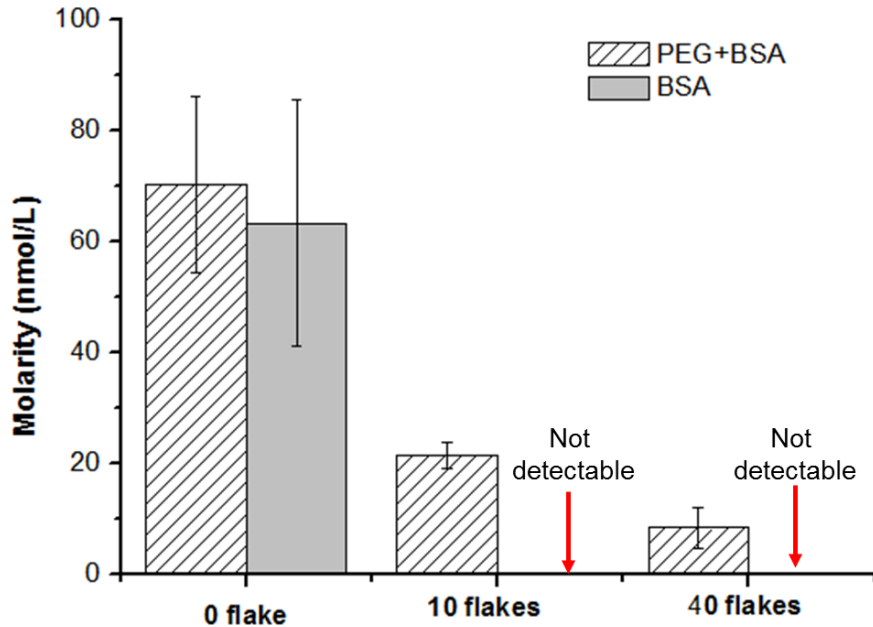


Figure 5-4: Study of dynamic coating of PeT chip to improve amplification result. PCR product concentration is affected by the number of Pe pieces in the PCR tube.

5.3.3 Amplification of λ -phage DNA and *Azospirillun Brasilienses* DNA

In earlier work by Duarte et al., amplification of 520 bp fragment of λ -phage DNA in a 10 μ L volume on PeT microchip by using conventional heating¹¹. Here, the volume of the PCR chamber has been reduced to 2 μ L for amplifying the same fragment in λ -phage genome. Figure 5-5 shows that successful PCR amplification could be accomplished on the microchip only if PEG-200 was added as dynamic passivation additive. The observation here, again, confirms that dynamic passivation for the PeT

microchip fluidic architecture is essential for successful PCR. Not surprisingly , similar PCR enhancement with PEG was observed within polyimide¹⁷ and glass²² microchips using IR-thermocycling.

Representative electropherograms of the amplification products resulting from thermocycling times that have been shortened by decreasing the number of the cycles are given Figure 5-5. Acknowledging that Bioanalyzer 2100 only provides semi-quantitative analysis of the product concentration, it is still useful for estimating the average PCR efficiency per cycle of each PCR reaction carried under different themocycling settings. A PCR efficiency of ~25% was obtained for the 35 min amplification containing 30 thermal cycles. As the cycler number reducing from 30 to 20 cycles, the reaction time decreased to 25 min with a PCR efficiency of ~31%. Maintaining the same number of cycles, the time was further reduced by decreasing the hold times for both annealing and

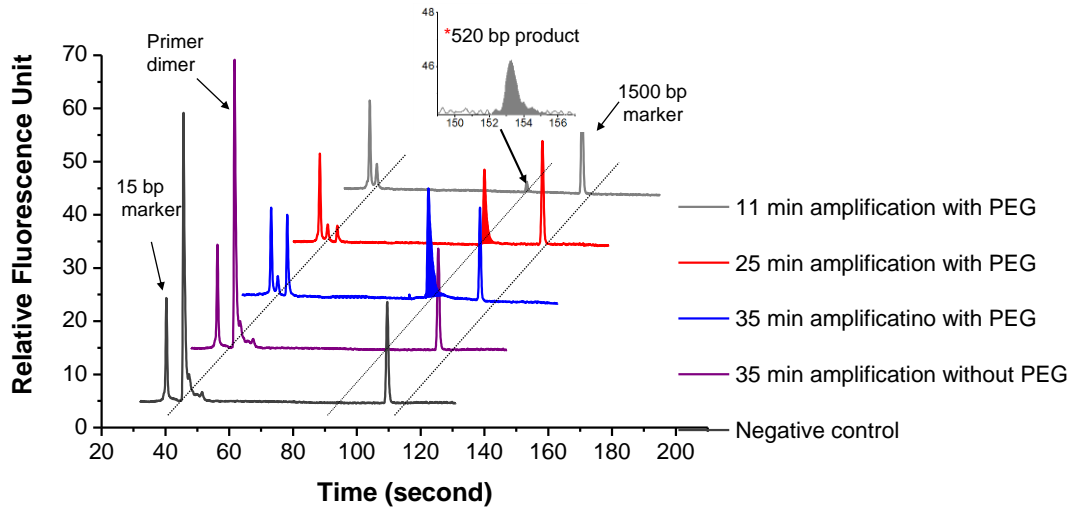


Figure 5-5: Electropherogram showing (1) successful amplifications of a 520 bp fragment of λ DNA in a PeT microchip can be achieved by adding PEG in master mix; (2) the detectable 520 bp amplicons can be obtained when reduce the thermal cycling time by 3 fold.

denaturing steps from 30 second to 10 seconds, yielding a total PCR time of 11 min and a concurrent PCR efficiency $\sim 20\%$. While the product peak from the 11-minute PCR reactions was small, it was clearly present as the signal to noise ratio was 20:1.

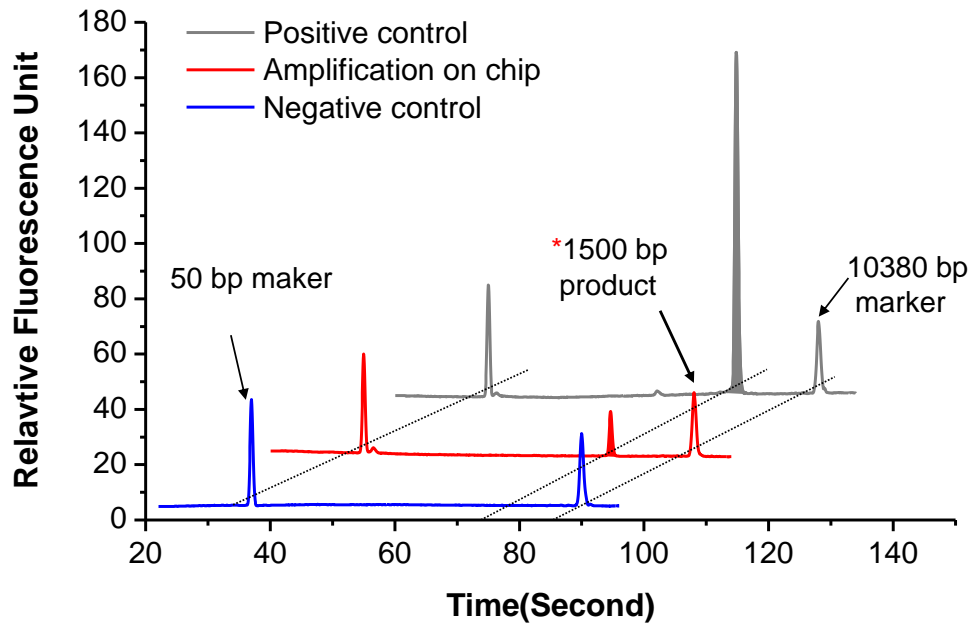


Figure 5-6: Electropherogram showing successful amplifications of a 1500 bp fragment of *Azospirillum brasiliense* DNA in a PeT microchip.

The PeT microchip was challenged to amplifying a long fragment (1500 bp) from the genome of *Azospirillun Brasillienses* (Figure 5-6). Using the same dynamic surface passivation, the on-chip PCR efficiency was estimated to be $\sim 28\%$, a value that was 75% relative to the tube-based PCR efficiency ($\sim 37\%$). The extension time used in this PCR is significantly longer (80 second *vs* 30 second, See the *Experiment* section), a necessary modification given the length of the amplicon and inherent limitations of the speed for base incorporation of standard *Taq* polymerase. As a result, the on-chip thermal cycling

time is 95 min, representing a reduction of 30% in time relative to conventional PCR method. The extension time can be potentially shortened if an engineered *Taq* with faster synthesis speed (i.e. 10 sec/kb of *SpeedSTARTM* relative to the 60 sec/kb with standard *Taq* polymerase) is utilized in the future. Nevertheless, the success of using PeT microchip for long duration of PCR suggests the good durability for IR radiated thermalcycling.

5.3.4 Multi-chamber thermal control for PCR on a PeT microchip

In order to transition from single-chamber PCR to multichamber PCR on PeT microchip while using the same IR-mediated thermal control, a centrosymmetrical chambers configuration on microchip was introduced as shown in Figure 5-7 but replaced the tungsten heating source with a halogen lamp to acquire a

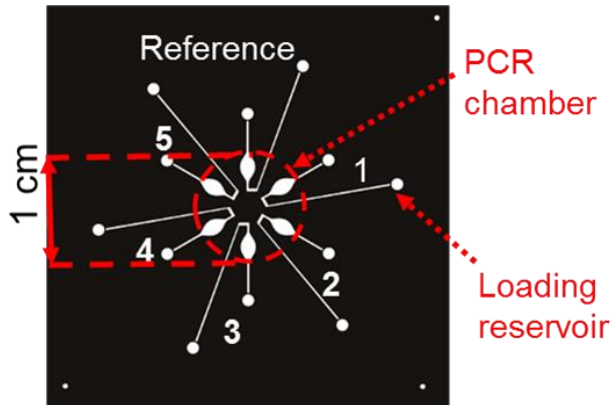


Figure 5-7: A centrosymmetric design of PeT microchip (4.5 cm × 4.5 cm) used with a halogen lamp as IR radiation source. The PeT microchip has one reference chamber and five PCR sample chambers.

larger focus spot. The design of the multichambered PeT microchip has six centrosymmetryical PCR chambers, connected to channels for sample loading and collection, has a volume of ~500 nL. With a halogen lamp providing a larger and more

centrosymmetrical heating spot, all the sample chambers should be exposed to an equivalent intensity of IR radiation. Homogenous heating of all chamber (low inter-chamber variation) is essential if a single chamber is to serve as the PID-controlled reference chamber for servo-based control of temperature cycling.

The temperature behavior of PeT microchips on the IR-PCR system was characterized through real-time temperature monitoring during the mock PCR thermal cycling experiments. Since black toner has been well characterized in the previous work, the black PeT microchips filled with 1× Qiagen *Taq*PCR buffer, thermocycled and similar to what was observed with tungsten lamp system, metal foil masking was required for well-controlled IR-mediated heating without overshooting the desired temperatures. For set temperatures of 68 °C and 90 °C, the reference chamber maintained a temperature of 67.9 ± 0.3 °C and 90.5 ± 0.5 °C respectively. As shown in Figure 5-8, measurement of the temperatures sensed in both the reference chamber (used to control lamp power and fan) and sample chamber track almost perfectly. Similar results were obtained with other reference sample chamber comparison, indicating that all chambers could reach the desirable temperatures and maintained them without significant

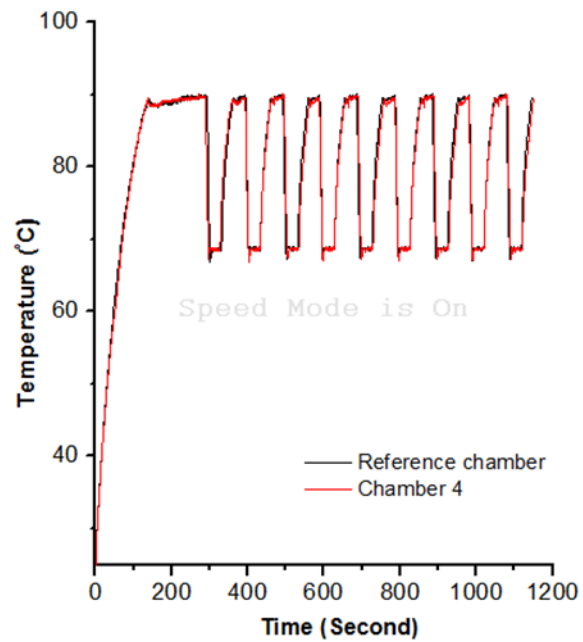


Figure 5-8: Temperatures of the reference chamber and a representative sample chamber as a function of time on the same multichambered PeT microchip.

temperature oscillation or deviation from the set point. As shown in Figure 5-9, the inter-chamber temperature standard deviation from annealing (68 °C), extension (72 °C) and denaturing steps (91 °C) were ± 1.0 °C, ± 0.6 °C and ± 1.5 °C respectively. Since the multichambered PeT microchip for PCR was highly symmetrical, the measured temperature discrepancy is likely due to the variation in the emitted radiation from the halogen lamp, and should scale with the intensity of the radiation applied (voltage applied); this is corroborated by the fact that the inter-chamber temperature standard deviation was

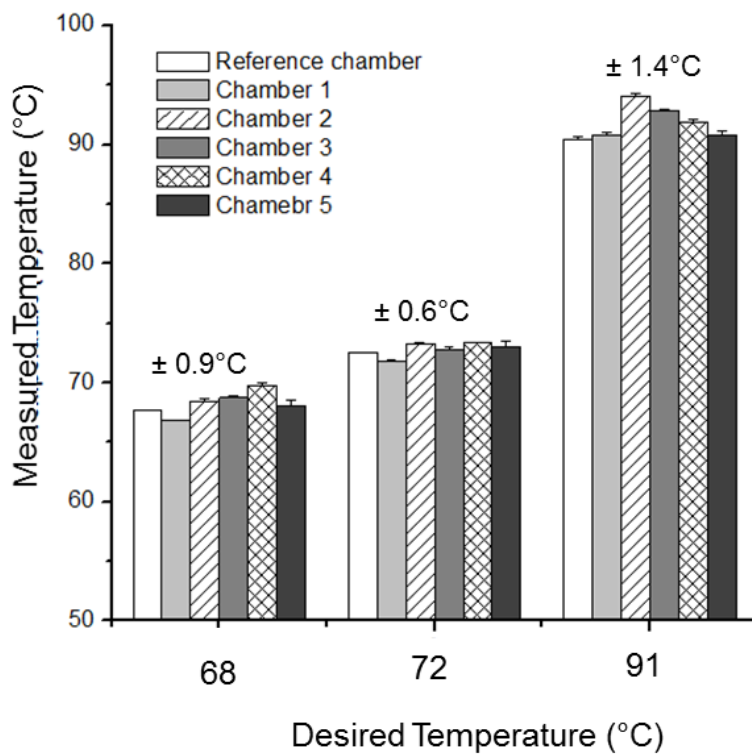


Figure 5-9: Temperature discrepancy in six-chambered PeT microchip with foil mask on IR-PCR setup using halogen lamp. All values are expressed as average \pm one standard deviation ($n=3$). Standard deviation of inter-chamber temperature is provided at the top of bars.

greatest at highest temperature (91 °C). The less than ± 1 °C temperature deviation at the annealing and extension temperatures is comparable to most of 96-well Peltier-based thermocyclers on the market²³, suggesting the potential of using a centrosymmetric chamber configuration and heating source for multichambered PCR thermal control.

5.3.5 Optimization of the ramp rate for multi-chambered PCR thermal cycling

Temperature ramp rates are another important performance metric with microchip-based PCR systems, since faster ramp rate means shorter cycling time. The heating rate of black PeT microchips with foil mask was determined to be 1.0 ± 0.1 °C/s while the cooling rate was 4.1 ± 0.1 °C/s ($n=3$). The heating rates were comparable to a conventional thermocycler and uncharacteristically low for an IR-PCR system. The unsatisfactory heating rate was likely attributed to the use of the chambers-only aluminum foil (“Chamber-only mask” in Figure 5-10) that reflects majority of the IR radiation. Direct heating of the microchip substrate itself contributes significantly to heating in polymeric IR-PCR microchips. In order to maximize the power impinging on the chip surface, the aluminum foil coverage needed to be minimized, and other others (magenta, yellow and cyan toners) were considered as substitutions to the black toner for bonding PeT microchips. Ramp rate of non-black PeT microchips with different foil masks were again studied through mock PCR thermal cycling experiments. Besides utilizing the chamber-only foil mask, a new foil mask (“Centro-spot Mask” in Figure 5-10) was designed, which allows the center of the non-black PeT microchip (diameter = 1cm) to be fully exposed to the IR radiation. Contrast to the black PeT microchip, overheating in the PCR chambers was not observed on the color PeT microchips with the centro-spot mask and their heating rates were increased by 3~4 fold compared to the black or magenta PeT microchips covered by the chamber-only mask (Figure 5-10). In addition, the reduced coverage of foil mask on the PeT also reduced the insulation effect during the cooling process as evidenced by the enhancement in the cooling rate.

Since magenta PeT microchip provided the fastest ramp rate (heating rate= $3.9 \pm 0.3 \text{ }^{\circ}\text{C second}^{-1}$, cooling rate = $5.0 \pm 0.3 \text{ }^{\circ}\text{C second}^{-1}$) compared to the others, it was chosen for further experiments. It was clear that the ramp rate on the multichamber magenta PeT microchip-halogen system was 2-3 fold lower compared to the two-chamber black PeT microchip-tungsten system. Using the optimum voltages recommend by the manufacturers and actual voltages supplied to the lamps in the experiments, the calculated power output of the tungsten and halogen lamps were 19.5 watts and 8.5 watts respectively, and may

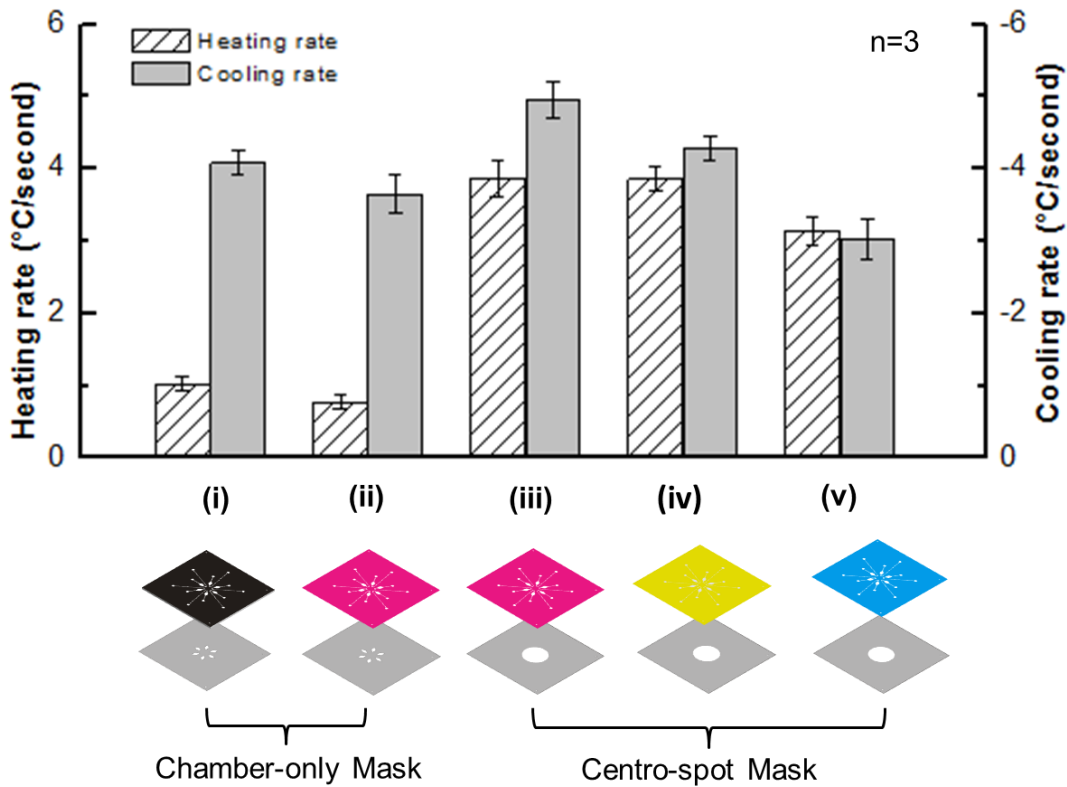


Figure 5-10: Comparison of the ramp rate between different colored chips with foil mask in the mock thermal cycling experiments. (i) Black and (ii) Magenta PeT microchips with chamber-only aluminum foil mask, in which setting only PCR chambers are chamber exposed to the IR radiation. (iii) Magenta PeT microchip, (iv) yellow PeT microchip and (v) cyan PeT microchip with centro-spot aluminum mask, which allows the center of the microchip (D.I.= 1 cm) to be exposed to IR radiation. Error bars denote one standard deviation of three replicates.

provide a possible explanation for the lower ramp rate with the magenta PeT microchip-halogen system. The observed decrease in the cooling rate is likely due to the larger thermal mass in the multi-chamber PeT microchip compared to the two-chamber PeT microchip when using the same convective cooling power from the fan. With the necessity to use the halogen lamp for multichamber IR-PCR microchip to obtain a low inter-chamber temperature variability, and the trade-off between ramp speed and multiplex chamber capability was acceptable. Nonetheless, the heating rate of the multichamber microchip could potentially be improved in the future by increasing the electrical power to the lamp to increase the IR output of the halogen lamp.

5.3.6 Amplification of DNA fragment on multichamber PeT microchip

In order to evaluate effectiveness of multichamber PeT microchip for PCR, amplification of a 520 bp region of λ -phages DNA genome in 5-sample chambers of the PeT microchip was carried out to provide evidence of temperature control and biochemical compatibility. Using the same dynamic passivation method discussed earlier, specific product peaks from each chamber on the magenta PeT microchip covered by the centro-spot mask further confirms the effectiveness of IR-mediated temperature control in multichamber PeT microchips for PCR application (Figure 5-11). Noticing the differences in the peak height between chambers, this multichambered PeT microchip has a noticeable range in PCR efficiency. The variation in the peak height may be due to a variety of factors such as small temperature deviations from the set temperature, reproducibility of dynamic passivation, insufficient collection of samples, and

eletcrokinetic bias in electrophoretic analysis, etc.²⁴ Obviously, the multichamber PCR here can be used for qualitative analysis. Ultimately, peak height is a secondary concern because internal control reactions could be multiplexed into the PCR recipe to normalize the peak heights.

To show applicability to the amplification of human genomice DNA, the system was challenged with amplification of a 380 bp fragment of β -globin gene from human genomic samples. The complexity and size (3.3×10^9 bp) of the human genome presents

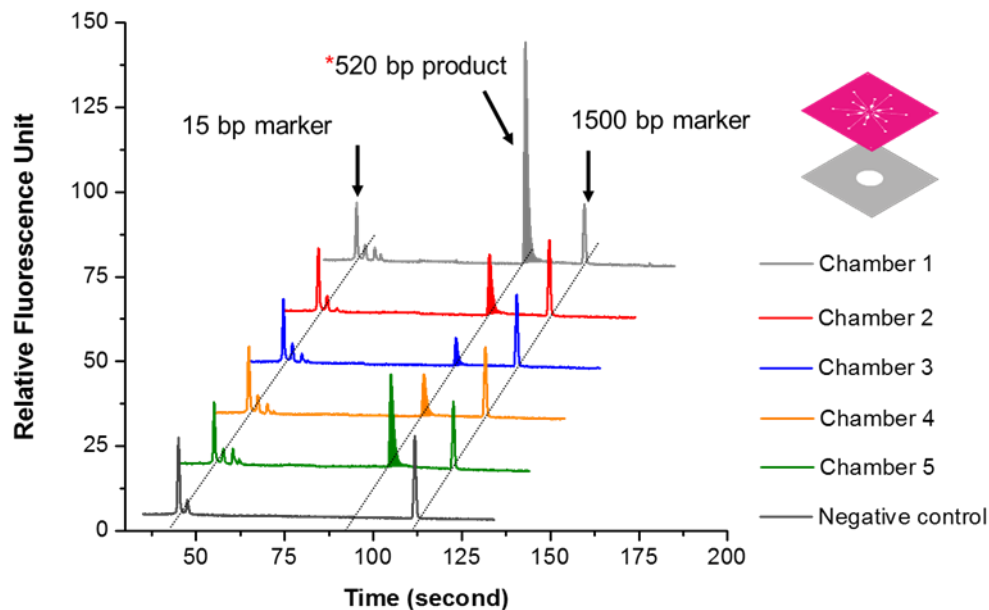


Figure 5-11: Electropherograms in the representative of three replicates resulting from analysis of amplified products of λ -phage DNA on multichambered magenta PeT microchip cover by foil mask II. The 520 bp highlighted by black dash line represents λ -phage DNA amplicon. Negative control was carried out in conventional PCR thermal cycler. Note that the 15 bp and 1500 bp markers were added to PCR product only before the electrophoresis.

a challenge for reaction specificity and amplification efficiency. Successful amplification of β -globin gene fragment from 2 ng human genome (~540 genome copies) were obtained from all the sample chambers as proven by the electropherograms in Figure 5-12. Based

on the semi-quantitative result from Agilent Bioanalyzer, the average PCR efficiency per cycle for conventional tube-based PCR as positive control was estimated to be $73 \pm 5\%$, while the efficiency of on-chip PCR amplifications ($n=3$) was estimated ranging from $51 \pm 3\%$ (chamber 3) to $68 \pm 3\%$ (chamber 1) with the inter-chamber standard deviation of 10%. The on-chip PCR efficiency is 70-90% relative to efficiency to the conventional instrument and is comparable to the relative efficiencies described with different template DNA and heating methods on glass microchips for single PCR reaction^{18,25}.

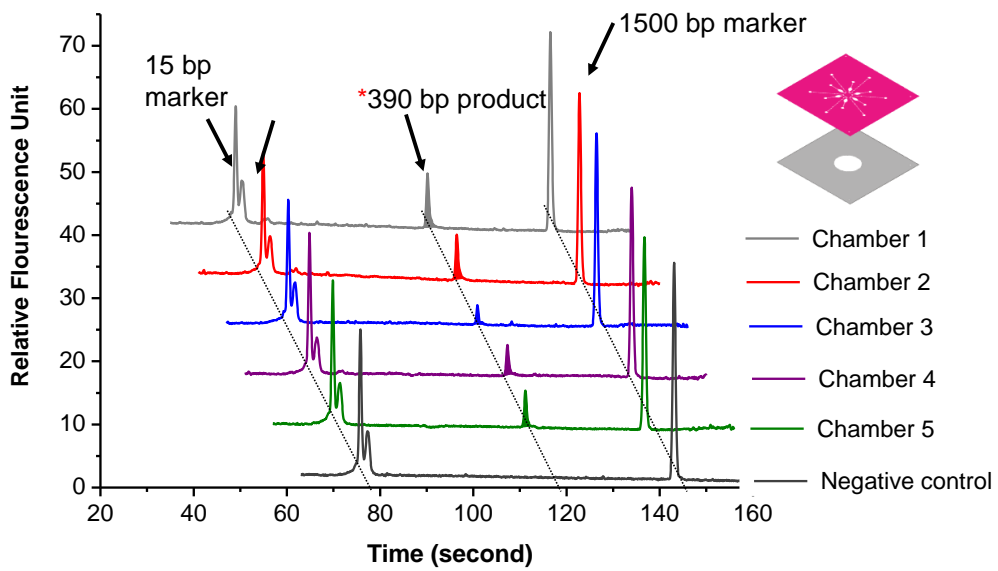


Figure 5-12: Electropherograms in the representative of three replicates resulting from analysis of amplified β -globin gene of human genome DNA on multichambered magenta PeT microchip cover by foil mask II. The 390 bp highlighted by black dash line represents beta-globin amplicon. Negative control was carried out in conventional PCR thermal cycler.

5.4 Conclusion

This chapter reports development of PeT microchip for PCR via IR-mediated control system. The PCR compatibility of PeT surface can be improved simply by addition of dynamic passivation agents. PeT microchips with one- or five-sample throughput were designed and fabricated. Fast amplification of λ -phage DNA was demonstrated on the PeT microchip of one sample throughput with a 5 fold reduction time relative to conventional PCR methods. In addition, the PeT microchip can also withstand long duration of PCR for amplification of long fragment from bacteria genome. Although the ramp rate of the multichambered PeT microchip was inferior to that of a two-chamber PeT microchip, it is the first example of parallelizing PCR on PeT microchip on IR-PCR setup, broadening the scope of possible IR-PCR applications. The effectiveness of multichamber PeT microchips for PCR was demonstrated by amplifying human genome DNA with an average 80% PCR efficiency relative to the conventional thermal cycler. When combined with the dynamic solid-phase extraction and electrophoretic separation of DNA that have been previously developed on PeT microchips, this work improves one of the bioanalytical processes vital to using PeT microchips as a microfluidic total genetic analysis platform.

5.5 Reference

1. N. Ramalingam, Z. Rui, H. Liu, C. Dai, R. Kaushik, B. Ratnahraka, and H. Gong, *Sensors Actuators B. Chem.*, 2010, **145**, 543–552.

2. C. Zhang and D. Xing, *Nucleic Acids Res.*, 2007, **35**, 4223–37.
3. J. a Lounsbury, A. Karlsson, D. C. Miranian, S. M. Cronk, D. a Nelson, J. Li, D. M. Haverstick, P. Kinnon, D. J. Saul, and J. P. Landers, *Lab Chip*, 2013, **13**, 1384–93.
4. C. J. Easley, J. M. Karlinsey, J. M. Bienvenue, L. A. Legendre, M. G. Roper, S. H. Feldman, M. A. Hughes, E. L. Hewlett, T. J. Merkel, J. P. Ferrance, and J. P. Landers, *Proc. Natl. Acad. Sci. U. S. A.*, 2006, **103**, 19272–7.
5. G. V Kaigala, V. N. Hoang, A. Stickel, J. Lauzon, D. Manage, L. M. Pilarski, and C. J. Backhouse, *Analyst*, 2008, **133**, 331–8.
6. D. Chen, M. Mauk, X. Qiu, C. Liu, J. Kim, S. Ramprasad, S. Ongagna, W. R. Abrams, D. Malamud, P. L. a M. Corstjens, and H. H. Bau, *Biomed. Microdevices*, 2010, 705–719.
7. X. Pan, L. Jiang, K. Liu, B. Lin, and J. Qin, *Anal. Chim. Acta*, 2010, **674**, 110–5.
8. Y. Zhang, S. Park, S. Yang, and T.-H. Wang, *Biomed. Microdevices*, 2010, 1043–1049.
9. Y. Zhang and P. Ozdemir, *Anal. Chim. Acta*, 2009, **638**, 115–25.
10. C. Zhang, J. Xu, W. Ma, and W. Zheng, *Biotechnol. Adv.*, 2006, **24**, 243–84.
11. G. R. M. Duarte, C. W. Price, B. H. Augustine, E. Carrilho, and J. P. Landers, *Anal. Chem.*, 2011, 5182–5189.

12. H. Becker and L. E. Locascio, *Talanta*, 2002, **56**, 267–87.
13. C. Zhang and D. Xing, *Nucleic Acids Res.*, 2007, **35**, 4223–37.
14. R. P. Oda, M. a Strausbauch, a F. Huhmer, N. Borson, S. R. Jurrens, J. Craighead, P. J. Wettstein, B. Eckloff, B. Kline, and J. P. Landers, *Anal. Chem.*, 1998, **70**, 4361–8.
15. a F. Hühmer and J. P. Landers, *Anal. Chem.*, 2000, **72**, 5507–12.
16. B. C. Giordano, J. Ferrance, S. Swedberg, a F. Hühmer, and J. P. Landers, *Anal. Biochem.*, 2001, **291**, 124–32.
17. M. G. Roper, C. J. Easley, L. A. Legendre, J. A. C. Humphrey, and J. P. Landers, *Omega*, 2007, **79**, 1294–1300.
18. L. Chen, J. West, P.-A. Auroux, A. Manz, and P. J. R. Day, *Anal. Chem.*, 2007, **79**, 9185–90.
19. Y. Xia, Z. Hua, O. Srivannavit, A. B. Ozel, and E. Gulari, *Chem. Technol.*, 2007, **38**, 33–38.
20. L. J. Kricka and P. Wilding, *Anal. Bioanal. Chem.*, 2003, **377**, 820–5.
21. Y. Xia, Z. Hua, O. Srivannavit, A. B. Ozel, and E. Gulari, 2007, **38**, 33–38.
22. B. C. Giordano, E. R. Copeland, and J. P. Landers, *Electrophoresis*, 2001, **22**, 334–40.

23. D. Schoder, A. Schmalwieser, G. Schauberger, J. Hoorfar, M. Kuhn, and M. Wagner, 2005.
24. D. C. Leslie, E. Seker, L. a L. Bazydlo, B. C. Strachan, and J. P. Landers, *Lab Chip*, 2012, **12**, 127–32.
25. Y. Yu, B. Li, C. a Baker, X. Zhang, and M. G. Roper, *Anal. Chem.*, 2012, **84**, 2825–9.

Chapter 6: Future Direction

6.1 Overview

The work in this dissertation focused on exploiting the potential of using PeT microchip as a disposable, cost-effective microdevice for point-of-care diagnostics. Flow control, detection as well as surface modification have been implemented on the PeT microchip for a variety of bioanalytic purposes. With all the development of PeT microdevices and existing technologies that can be integrated onto PeT microdevices, it seems more functions can be developed on PeT microdevice. In addition, it is now feasible to envision that specialized micro total analysis system (μ -TAS)¹ will be devised in the near future.

6.2 Flow Control

The work in Chapter 2 demonstrated an inexpensive and rapid approach to fabricate microfluidic systems with passive valves allowing for a four-step reagent delivery. One has to acknowledge that, for some assays that may require a high centrifugal speed as the first step (e.g., ~3600 rpm to separate plasma from the red blood cells²), toner valves will be insufficient. However, due to the hydrophilic property of the commercial Pe film, a siphoning structure similar to those shown by Ducrée's group^{3, 4} could be adopted. Additionally, the burst pressure bandwidth of the toner valves is not as broad as phase-change valves^{5, 6, 7}, and hence it is challenging to achieve eight or nine sequential reagent

addition steps at this point. Therefore, approaches to enhance the burst pressure bandwidth will be a future research focus.

6.3 Reagent Storage on PeT Microchip

Before using PeT microchip as a cost-effective, disposable cartridge for the point-of-care analysis in the resource-limited situations, sample storage on microdevice is another important issue to address. Since the hydrophobic toner patches presented in Chapter 2 do not provide a vapor barrier, on-chip storage of the liquid reagents could therefore be problematic. This could be addressed by using lyophilized reagents which can be reconstituted when buffer or sample is loaded; such feasibility has been demonstrated by Fockes et al.^{2,3} on polymeric-based microchips (despite using a non-PeT substrate).

Modification of fabrication procedure might be necessary when implementing the reagents storage on PeT microdevices. The lamination temperature used in the current work is 130 °C, with a lamination roller speed of 2.5 mm/second. It is estimated that the heated roller contact time for one spot on the film surface is 4-6 second. For a dried reagent with a melting/decomposition temperature higher than 130 °C, it is possible that the chemicals maintain their integrity after lamination. However, if heat sensitive reagents (e.g., enzymes) need to be pre-stored, one could circumvent this problem by substituting one of the adhesive toner layers with a pressure-sensitive adhesive such that a cold lamination process could be utilized to seal the chamber for the reagent storage.

6.4 Portable PeT Microdevices Platform for Integrated Assays

Chapter 3 and Chapter 4 have demonstrated that the developed rotation-driven PeT microdevices provide all the essential needed for total protein quantitation in blood plasma, DNA quantitation in blood, white blood cell counting in blood. Further progress based on these works is to develop a microfluidic device that will provide direct readout of white blood cell count, total protein concentration and albumin concentration simultaneously. The reason for incorporating the albumin quantitation is that the level of albumin can serve as a surrogate marker for nutritional status. Thus, the integrated PeT microdevices can provide more comprehensive monitoring for patients' health status.

The design from Chapter 3 could be leveraged for albumin test for flow control and the indicator will be switched from tetrabromophenol blue to an indicator that is albumin specific (i.e., bromocresol green)⁹. The same design can be used to optimize the assay conditions (e.g., pH, dye concentration, volume of plasma, etc.) for obtaining a color change that is detected with maximum sensitivity via scanning using the same hardware described in Chapter 3 and 4, requiring only a modification of image algorithm.

Once the chemistry for all the quantitation assays are defined (sample/aliquot volumes for each assay), optimization in the microfluidic architecture to enable an accurate metering, dilution and mixing performance will be the following step. Since both the protein measurements and cell counting on PeT microdevices use the same rudimentary flow control, fusing the architecture into one that provides sample-in-answer-out for protein and albumin quantitation, as well as white cell count, is achievable. Although the

design in Chapter 3 only allows two samples per device, footprint of each domain can be further compressed to increase the structure density by 2-3 folds in the new design.

Another improvement in the current system will be the miniaturization of the external hardware, which integrates the centrifugal platform, optical detection and readouts. Taking advantage of the existing technologies in the compact CD players, it is feasible to control the rotational speed of the spindle by directly hacking into and controlling the CD player's DC brushless spindle motor. This will allow spinning the sample at various rotation speeds to generate different magnitudes of centrifugal pumping pressures which ultimately controls fluidic flow. Utilizing the CD player's pre-existing laser tracking mechanism, detection chambers at different locations on the sample disk can be aligned into the optical sensor. By simply adding an inexpensive (<\$20) color sensor system, the modified CD player should be able to automatically read the WBC count, total protein and albumin concentration from the patients' blood samples. Any additional digital signal processing can be performed on the device using the same embedded microcontroller chip that controls the motors and automated testing process. This microcontroller could also be

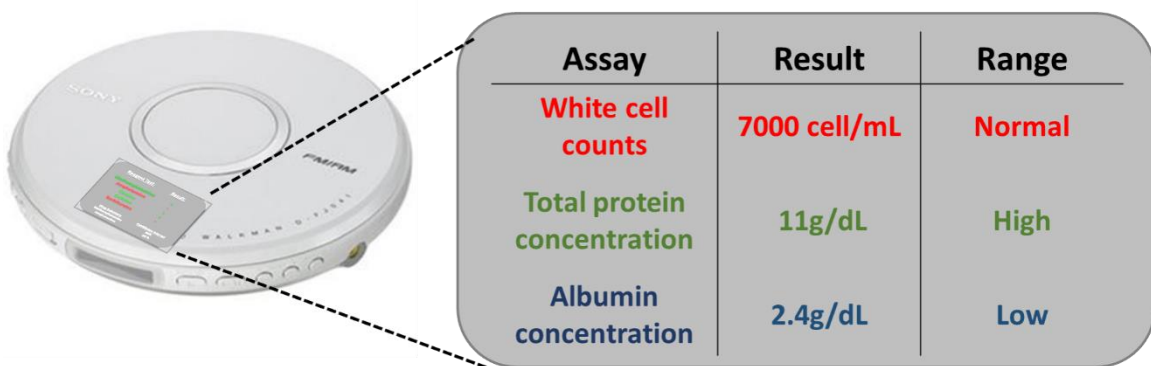


Figure 6-1: Concept device to be built as external support hardware for portable PeT microdevices.

programmed to clearly display the results of the analyses on an LCD screen that is built into the unit (Figure 6-1).

6.5 Reference

1. a. Manz, N. Gruber, and H. M. Widmer, *Sensors Actuators B Chem.*, 1990, **1**, 244–248.
2. J. Park, V. Sunkara, T.-H. Kim, H. Hwang, and Y.-K. Cho, *Anal. Chem.*, 2012, **84**, 2133–40.
3. S. Haeberle, T. Brenner, R. Zengerle, and J. Ducr  , *Lab Chip*, 2006, **6**, 776–81.
4. J. Steigert, T. Brenner, M. Grumann, L. Rieger, S. Lutz, R. Zengerle, and J. Ducr  , *Biomed. Microdevices*, 2007, **9**, 675–9.
5. D. J. Beebe, J. S. Moore, J. M. Bauer, Q. Yu, R. H. Liu, C. Devadoss, and B. Jo, *Nature*, 2000, **404**, 588–590.
6. K. Abi-Samra, R. Hanson, M. Madou, and R. a Gorkin, *Lab Chip*, 2011, **11**, 723–6.
7. R. Gorkin, C. E. Nwankire, J. Gaughran, X. Zhang, G. G. Donohoe, M. Rook, R. O’Kennedy, and J. Ducr  , *Lab Chip*, 2012, **12**, 2894–902.
8. M. Focke, F. Stumpf, B. Faltin, P. Reith, D. Bamarni, S. Wadle, C. M  ller, H. Reinecke, J. Schrenzel, P. Francois, D. Mark, G. Roth, R. Zengerle, and F. von Stetten, *Lab Chip*, 2010, **10**, 2519–26.

9. H. G. B. Basil T. Doumas, W. Ard Watson, *Clin. Chim. Acta*, 1970, **31**, 87–96.